Opening the Black Box of III-V Nanowire Growth

Marnauza, Mikelis

2025

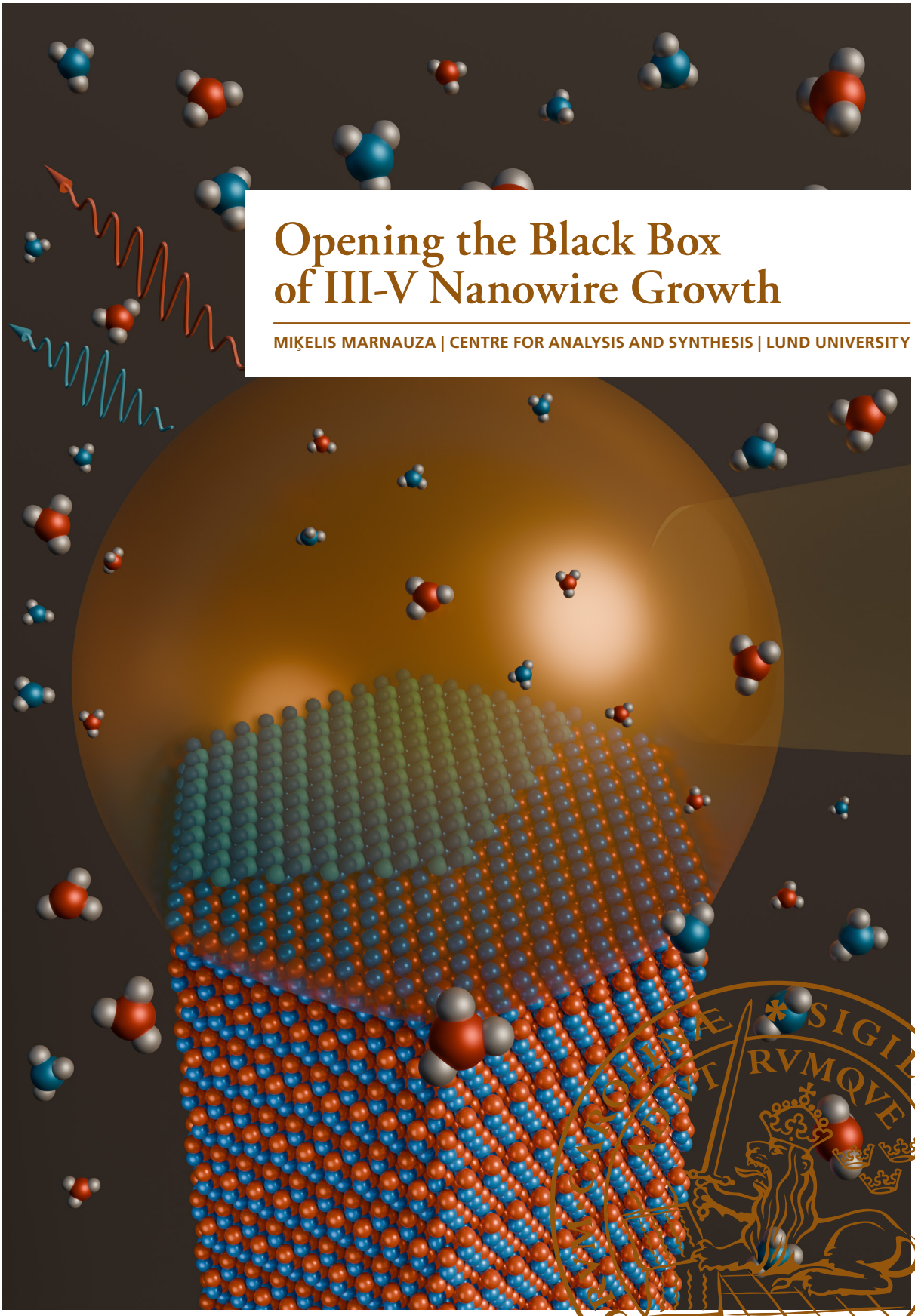

Opening the Black Box of III-V Nanowire Growth

MIĶELIS MARNAUZA | CENTRE FOR ANALYSIS AND SYNTHESIS | LUND UNIVERSITY

Opening the Black Box of III-V Nanowire Growth

Opening the Black Box of III-V Nanowire Growth

Miķelis Marnauza

LUND
UNIVERSITY

DOCTORAL DISSERTATION

Doctoral dissertation for the degree of Doctor of Philosophy (PhD) at the Faculty of Engineering at Lund University to be publicly defended on 28th of February at 9.00 in Lecture Hall KC:A at the Department of Chemistry, Naturvetarvägen 22, Lund

Faculty opponent
Philippe Caroff

Thesis advisors:

Kimberly Dick-Thelander, Martin Ek Rosén, Daniel Madsen

Organization: LUND UNIVERSITY

Document name: Doctoral Dissertation **Date of issue:** 2025-02-28

Author(s): Miķelis Marnauza **Sponsoring organization:**

Title and subtitle: Opening the Black Box of III-V Nanowire Growth

Abstract:

Group III-V semiconductor nanowires are a material platform with potential applications in electronics, photovoltaics and optoelectronic devices. One of the central challenges in the growth of III-V semiconductor nanowires is to understand the dynamic processes that occur during crystallization. However, the growth of these materials is commonly performed in closed systems. There the details of the growth dynamics are hidden from us, resulting in these systems being described as black boxes. Therefore, nanowire growth studies in the past generally have relied on a combination of theoretical modelling coupled with post growth analysis of the as-grown nanowires.

This thesis presents a different approach. Here the black box of nanowire growth is opened by performing the growth of Au-seeded III-V semiconductor nanowires in an environmental transmission electron microscope. This enables us to study nanowire growth ***in situ***, effectively coupling the growth with real-time observations at atomic resolution. This gives information about the fundamental interplay between vapour phase precursors, liquid seed nanoparticle and solid nanowire during growth.

The ability to study growth in real time is used in this thesis to describe how the lateral dimensions of GaAs nanowires affect the growth dynamics. This is achieved by acquiring high frame rate videos of the layer-by-layer growth process and correlating the changes in dynamics to nanowire diameter. This is followed by a detailed characterization of GaSb nanowires focused the aspects of morphology and growth dynamics, where I first discuss the impact of growth conditions on the seed nanoparticle composition and morphology. Thereafter, I present how these conditions affect the growing nanowire morphology and growth dynamics. Lastly, I showcase the formation of GaSb/GaAs axial nanowire heterostructures. In addition to examining the growth parameters required for successful heterostructure formation a detailed description of the growth dynamics during heterojunction formation is provided.

The findings presented in this thesis could be used to improve the modelling and growth of III-V nanowires using conventional growth systems, to further our goal of controlling and more importantly understanding the growth of these materials at the atomic scale.

Key words: Nanowires, semiconductors, III-V, TEM, ***in situ***, Environmental TEM, Crystal growth, MOCVD, heterostructures

Language: English **Number of pages:** 192

ISBN (print): 978-91-8096-086-1

ISBN (electronic): 978-91-8096-087-8

Opening the Black Box of III-V Nanowire Growth

Miķelis Marnauza

LUND
UNIVERSITY

Cover illustration front: Artistic imagining of a Au-seeded GaSb nanowire during *in situ* growth illuminated by an electron beam. The growing nanowire is surrounded by metalorganic molecules that supply the growth species. The electron beam illumination of the catalyst nanoparticle results in the creation of characteristic X-rays

Cover illustration back: My cat Mentijs and her pawprints. The pawprints were acquired with assistance from Ellinor Salomonsson.

Faculty of Engineering (LTH)

Department of Chemistry, Centre for Analysis and Synthesis

ISBN (print) 978-91-8096-086-1

ISBN (electronic) 978-91-8096-087-8

Printed in Sweden by Media-Tryck, Lund University

Lund 2025

"It's not impossible that weird things happen."

-Kimberly Dick-Thelander

Table of Contents

Acknowledgements

My deepest gratitude undoubtedly has to be expressed to my supervisor **Kimberly Dick-Thelander**. You have been a true inspiration since the day I started my PhD and are one of the very few people I wholeheartedly trust and admire. I cannot stress enough how much you have taught me about science, and a proper way to do research, but what I will never forget are all the shared coffee breaks, experiments and heart-to-heart talks over the years. Whenever asked to picture a scientist in my mind, you are the person I will always imagine.

I have been lucky enough to have more than one role model in my time as a PhD. **Daniel**, your undying passion for engineering work, nanowire growth and talent in always finding a solution has motivated me to never give up when faced with problems. Sometimes I have even started to think of you as an adult, but then you climb inside the ETEM like a crazed squirrel and prove me otherwise! **Martin**, your vast knowledge of TEM characterization of nanowires has never ceased to amaze me. However, what I will always cherish is your willingness to help and support me in research work, career guidance or by having a friendly chat over some coffee. **Sebastian**, your seemingly limitless knowledge of characterization methods and nanowire growth still baffles me. Despite that, you are one of the most humble, helpful people that I have ever known. It has been great working in the group knowing that you share the same love for dark humour, blunt honesty and painfully long sentences in scientific articles as I do.

Despite starting my PhD during a pandemic, I was still lucky enough to receive knowledge and guidance from postdocs and senior PhDs of the Inorganic NanoMaterials group that was an invaluable aid in finding my "sea legs". **Michael** and **Carina**, you were the hotshot postdocs in our group that seemed to know how to do everything in the ETEM, which made me hope to one day know as much about the system as you did. **Erik** and **Markus**, you were the senior PhD students in the group and the people who were down in the trenches with me aiding in the writing of my first manuscript. I appreciate you sharing your own stressful experiences and sound scientific advice that made my first years less daunting.

A key ingredient for my growth as a researcher was the bustling environment of the ETEM boys office. The magical quartet consisting of myself, **David, Robin, Tianyi**

was the best office environment I could have ever wished for. Together we could solve nearly all administrative, writing, studying and research issues that ever popped up during our PhD studies.

Tianyi, your perseverance in studying complex material systems while always being optimistic is something that has always impressed me. Your positive attitude and willingness to jump to help before even hearing what the problem is, has been exactly what our otherwise pessimistic office needed.

David, the oxygen thief and Mr. Licentiate himself. We have gradually become closer during the years of PhD and had romantic getaways to France and several dates in Sweden, much to dismay of your girlfriend. Your willingness to listen to my research and personal problems has been incredibly important to me. Moreover, our lively debates about research, studies and data have been exciting and driven me to become a better researcher.

Robin, I vividly remember the moment when I knew that we would become close friends. I had worked in the group for about two months and you called me a "bitch". The good cop, bad cop routine we played in teaching and supervision of Master's students, travelling to conferences all over the world, writing papers, grants and simply the time spent hanging out together have been some of my most treasured experiences as a PhD student.

Speaking of Master's students, I have to highlight my academic children **Azemina** and **Aidas**. You have helped me become a better teacher and watching you go from being nanostudents, to defending your Master's projects to becoming PhD students has been a pleasure. Furthermore, I want to mention my adopted academic children... **Hedda**, Ms. Magnetism and Norway, although I will never love magnetism like you do, your passion and excitement for research work is a sight to behold and it warms my heart that someone will continue to grow nanowires in the ETEM. **Fanny**, it has been great to have someone nearby also embroiled in the fight of their lives against a piece of paper aka writing their thesis. Our mental health walks (or hot girl walks as you like to call them), early morning writing sessions and sharing of memes has been a constant source of encouragement to me.

Beyond the office, I am grateful to have worked together with so many amazing people within the Inorganic NanoMaterials group, specifically: **Krishna**, **Christopher**, **Yuanyuan**, **Pei**, **Simon**, **Kshipra**, **Victor**, **Heidi**, **David L.**, **Isshin**, **Max**, **Edvin**, **Erika**, **Hampus** and **Mark** (who I am especially grateful to for proofreading this thesis). These five years would have been so extremely dull without all of you.

No electron microscopy work at Lund University could be imaginable without the dynamic duo of **Reine** and **Crispin**. **Reine**, I am thankful for your support as a departmental representative and giving me so many opportunities to teach students. I appreciate you encouraging me to bring forth my ideas and develop as a teacher. **Crispin**, your humour and never ending stories of research and microscopy are always a treat. You have saved me at the 3000F more times than I can count and I am thankful for all the microscopy wisdom you have given me. I will never forget our long walks to get liquid nitrogen and listen to the soothing sounds of the liquid nitrogen tank degassing.

Even though I have developed some idea of how one should conduct research, I have to admit that I am still completely blind to the administrative nuances of the university. For that, I have to give my thanks to **Sara** and **Maria**. You have been at the mercy of my ignorant questions for years and I thank you for your patience and assistance.

Two households, both alike in dignity, in fair Centre of Analysis and Synthesis (CAS), where we lay our scene, a materials chemist befriended an organic chemist.[1] **Aleks**, you have been a dear friend ever since I realized that you are as loud, sarcastic and annoying as I am during that fated Lucia celebration years ago. We have gossiped, roasted and supported each other for years and it has meant the world to me. After we both leave, the average noise level of CAS will undoubtedly drop significantly.

Thanks to all the colleagues (and ex-colleagues), collaborators and friends who made my time as a PhD student more enjoyable through exciting scientific collaborations or simply fun conversations. I especially want to express my gratitude to the following people: **Linnea L.**, **Pau**, **Linnea J.**, **Claes**, **Julia**, **Marie**, **Pegah**, **Isabell**, **Hannes**, **Niklas**, **Andrit**, **Olivier**, **Oskar**, **Jesper S.**, **Samuel**, **Clara**, **Anna**, **Lisa**, **Oksana**, **Alice**, **Joachim B.**, **Ofentse, Markus A.**, and **Malin**.

Out of all the friends I have made in Sweden I especially want to thank **Ellinor**. You have always been willing to listen to my excited, crazed ramblings of nanowire growth and research (and honestly why wouldn't you, chemical potentials are fun!). Our shared love of absolutely terrible Hallmark movies, potatoes, nanowires and eating five petal lilacs are only a fraction of the reasons why we just "click".

I also want to thank my friends and ex-colleagues from across the Øresund at Center for Quantum Devices (QDev) without whose support I would have never reached a point of starting a PhD: **Denise**, **Sara**, **Rasmus**, **Martin B.**, **Damon**, **Shiv**, and **Karolis**.

[1] Romeo and Juliet, Act 1, Prologue, by William Shakespeare, paraphrased.

I am especially grateful to the people that I would term my original scientific role models: **Thomas**, **Joachim S.**, and **Jesper N**.

Thomas, I am thankful to you for injecting me with the passion for research. You were willing to go the extra mile to help a Master student like me to find my next steps within science and you have always worked with an unmatched dedication. If my students could have the pleasure of seeing you in action, they would undoubtedly see where I got my teaching style from.

Jesper N., without you welcoming me in your group at QDev and letting me play with electron microscopes I would have not gotten where I am. Working at QDev I always felt like a part of the team, which meant so much to me. Our continued interactions in conferences and visits since my time as a Master student always remind me of all the great work we achieved at QDev.

Joachim, you are just about the weirdest person I have ever met and I say that with pure love. Your positive and easy-going attitude really made me see that it is possible to be an amazing researcher (which you are) all the while not living a life drowning in stress. It does not mean I know how to do that last part, but you inspire me to at least try.

I also want to thank to the original study group of weird (again said with pure love) people from my time as a Bachelor's student. **Rota**, **Rihards** and **Dāgs**, studying physics was a scary endeavour, but by having each others backs we all managed to not only graduate, but have loads of fun along the way. Reminiscing about the good old days as dumb students at our yearly meetings over a couple of beers is something I always look forward to. **Dāgs**, I am grateful to you especially since you chose to also embark on the great Danish adventure! I am glad you were there with me to show that random Latvian dudes are not too bad at that whole science thing.

Speaking of dear friends from Latvia… **Elza**, our friendship that started all those years ago has been an incredibly important part of my life. I am grateful for all the joyous moments we have spent together and thankful for your continued friendship. It is always a pleasure to meet for dinners and chat about how weird all those Swedes are!

To my adorable cat, **Mentijs**… mjau, mjau, mjau!

To my family: my mom **Ligita**, my dad **Dzintars**, my sister **Agnese**, my brother **Mārtiņš** and his wife **Lita**, and their kids **Roberts** and **Maija**. Paldies jums visiem! Bez jūsu iedrošinājumiem un padomiem es nebūtu uzdrīkstējies tiekties tik tālu, un bez jūsu nebeidzamā atbalsta es nekad nesasniegtu to pēc kā tiecos. Pēc Agneses ierosinājuma jums mani tagad jādēvē par Dr. Marnauzu.

Abstract

Group III-V semiconductor nanowires are a material platform with potential applications in electronics, photovoltaics and optoelectronic devices. One of the central challenges in the growth of III-V semiconductor nanowires is to understand the dynamic processes that occur during crystallization. However, the growth of these materials is commonly performed in closed systems. There the details of the growth dynamics are hidden from us, resulting in these systems being described as black boxes. Therefore, nanowire growth studies in the past generally have relied on a combination of theoretical modelling coupled with post growth analysis of the as-grown nanowires.

This thesis presents a different approach. Here the black box of nanowire growth is opened by performing the growth of Au-seeded III-V semiconductor nanowires in an environmental transmission electron microscope. This enables us to study nanowire growth *in situ*, effectively coupling the growth with real-time observations at atomic resolution. This gives information about the fundamental interplay between vapour phase precursors, liquid seed nanoparticle and solid nanowire during growth.

The ability to study growth in real time is used in this thesis to describe how the lateral dimensions of GaAs nanowires affect the growth dynamics. This is achieved by acquiring high frame rate videos of the layer-by-layer growth process and correlating the changes in dynamics to nanowire diameter. This is followed by a detailed characterization of GaSb nanowires focused the aspects of morphology and growth dynamics, where I first discuss the impact of growth conditions on the seed nanoparticle composition and morphology. Thereafter, I present how these conditions affect the growing nanowire morphology and growth dynamics. Lastly, I showcase the formation of GaSb/GaAs axial nanowire heterostructures. In addition to examining the growth parameters required for successful heterostructure formation a detailed description of the growth dynamics during heterojunction formation is provided.

The findings presented in this thesis could be used to improve the modelling and growth of III-V nanowires using conventional growth systems, to further our goal of controlling and more importantly understanding the growth of these materials at the atomic scale.

Popular Scientific Summary

As children most of us have played with Lego sets. These tiny building blocks that clip together allowing to construct virtually anything, often recreating real-world objects in smaller, more adorable scale. Just as the Lego bricks were the building blocks of our childhood — so are the atoms the building blocks of the world.

An atom is the basic particle of all chemical elements and similarly to a freshly opened box of Lego containing a disorganised pile of bricks, so too the atoms can exist in a mess with no apparent order. However, nature, like us, loves to build ordered things and atoms can be found in well defined, arranged structures called crystals. One of the most common crystalline materials is table salt that consists of sodium (Na) and chloride (Cl) atoms arranged in neat cubes.

Despite what it may currently seem like, the applications of crystalline materials go far beyond seasoning food. Virtually all modern day electronics utilize silicon (Si) crystals in their processors. Of course, to satisfy the forever growing need for electronic devices, it is not feasible to rely on finding Si crystals in nature. Therefore, we have learned to grow these crystals ourselves. In doing so we have also realized how to grow smaller and smaller crystalline materials reaching the nanoscale (billionth of a meter), which has allowed us to increase the performance of devices while reducing their dimensions.

Often, for use in applications, the grown crystals must be perfect; meaning that any slight misplacement of atoms in the crystal can cause poor device performance. This has resulted in the emergence of a whole field of science termed crystal growth, which essentially tries to understand the crystal growth process on a fundamental level.

The study of crystal growth is somewhat analogous to the process of baking a cake. To figure out the recipe for a tasty cake (or a perfect crystalline material), a variety of conditions of the oven (growth reactor), and the combination of ingredients (growth precursors) need to be tested. Ultimately, this process of trial and error might result in a delightful cake (or an equally delightful crystalline material). When baking a cake, I have often utilized the window in front of the oven to monitor the rise and browning of cake without interrupting the baking process. These observations of the cake inside the oven, or in other words *in situ* observations, are invaluable to obtaining a tasty, well baked cake. Without the ability to monitor the baking process in real time, significantly

more attempts would be required to adjust the temperature, balance of ingredients and baking time.

When growing nanoscale crystalline materials we normally lack the oven window. However, even if we had one, due to the small dimensions of crystals growing, it would be impossible to observe them with a naked eye. This is due to the crystalline materials we want to grow being nanoscale sized, making them about 10 million times smaller than a standard cake. Because of our inability to see the growth process (or baking using our analogy), the growth systems are often regarded as black boxes that rely on comparisons between the recipe and post-growth (baking) observations of the finished material.

Of course, scientists and bakers agree that seeing the growth (or baking) process provides invaluable information for improving the recipes. This has lead to the development of specialized instruments called environmental transmission electron microscopes that allow the study of crystalline material growth in real-time. These instruments combine the ability to facilitate growth of nanoscale crystalline materials, with the ability to investigate the growth process with atomic scale precision.

This thesis marks the most recent results of such real-time *in situ* studies for the specific subclass of crystalline materials termed nanowires (nanoscale, wire-like crystals), which are comprised of group III and group V elements of the periodic table. The overarching aim being to provide fundamental understanding of the growth process unattainable by conventional (*ex situ*) growth systems.

Populārzinātniskais apkopojums

No mazotnes lielākā daļa no mums ir spēlējušies ar Lego. Šie mazie klucīši, kas salīp kopā, ļauj uzbūvēt praktiski jebko, ļaujot mums būvēt lietas no mūsu ikdienas, mazākā, piemīlīgākā izmērā. Tāpat kā Lego klucīši bija mūsu bērnības galvenais būvniecības materiāls, tā atomi ir dabas mīļākais būvniecības materiāls.

Atoms ir ķīmisko elementu mazākā pamatdaļa, kas, tāpat kā tikko uz zemes izbērta kaudze ar Lego klucīšiem, dabā bieži vien ir sastopami bez jebkādas kārtības. Tomēr daba, tāpat kā mēs, mīl būvēt lietas ar noteiktu kārtību, un atomi bieži izvietojas specifiskās, sakārtotās struktūrās, kuras dēvē par kristāliem. Viens no populārākajiem šādiem piemēriem ir sāls kristāli, kas sastāv no nātrija (Na) un hlora (Cl) atomiem izkārtotiem kubiskā kristālstruktūrā.

Protams, kristāliski materiāli ir pielietojumi daudz vairāk lietām kā tikai ēdiena gatavošanā. Praktiski visas mūsdienu elektroniskās ierīcas ir balstītas uz silīcija (Si) kristāliem, kas atrodami to procesoros. Lai apmierinātu vienmēr augošo pieprasījumu pēc elektroniskajām ierīcēm, mēs nevaram paļauties uz dabā atrodamajiem Si kristāliem. Tāpēc mēs esam iemācījušies sintezēt kristālus. Audzējot kristālus mākslīgi, esam arī iemācījušies audzēt tos arvien mazākus un mazākus, sasniedzot nano skalu (metra miljardā daļa). Tas ir atļāvis uzlabot ierīču kvalitāti un jaudu vienlaikus samazinot to dimensijas.

Bieži vien kristāliskiem materiāliem, kas tiek izmantoti ierīču ražošanā, ir jābūt ar perfektu atomu izvietojumu, kas nozīmē, ka pat neliela novirze no noteikta atomu izkārtojuma rezultē ar zemu elektronisko ierīču kvalitāti. Šīs augstās prasības pret kristālu kvalitāti ir radījušas veselu zinātnisko lauku, proti, kristālisku materiālu audzēšana. Tā galvenais fokuss ir izprast kristālu augšanas procesu fundamentālā līmenī.

Viens no saprotamākajiem veidiem, kā aprakstīt kristālu audzēšanas procesu, ir izmantojot kūkas cepšanu kā analoģiju. Lai radītu jaunu recepti garšīgas kūkas cepšanai (vai perfektam kristāliskam materiālam), ir nepieciešams ņemt vērā krāsns (sintēzes reaktora) parameterus un izejvielu daudzumu un sabalansējumu. Šis process iekļauj sevī ilgu testēšanu un vairākus mēģinājumus, līdz beidzot tiek iegūta ilgi kārotā garšīgā kūka (vai perfektais kristāliskais materiāls). Cepot kūku, es bieži vien esmu izmantojis lodziņu krāsns durvīs, lai novērotu kūkas celšanos un gatavību nepārtraucot cepšanas

procesu. Šie cepšanas laikā veiktie novērojumi, ko latīņu valodā apzimētu ar terminu *in situ*, ir ārkārtīgi noderīgi ceļā uz garšīgu, labi izceptu kūku. Bez iespējas novērot kūkas cepšanu reāllaikā, visticamāk, mums nāktos izmantot daudz vairāk cepšanas mēģinājumu, lai atrastu optimālo temperatūru un cepšanas laiku, kā arī pareizu izejvielu balansu.

Audzējot kristāliskus materiālus mums reti kad ir pieejams lodziņš, lai novērtu augšanas procesu, un, pat ja būtu, tad kristālu ārkārtīgi mazā izmēra dēļ ar neapbruņotu aci tos tāpat nebūtu iespējams redzēt. Šo kristālisko materiālu dimensijas ir tik mazas, ka tie ir aptuveni 10 miljonus reižu mazāki kā standarta kūkas forma. Tā kā mēs nespējam novērot kristālu augšanas procesu (vai kūkas cepšanas procesu mūsu analoģijā), reaktori, kuri tiek izmantoti materiālu sintēzē, bieži vien ir dēvēti par melnajām kastēm. Tā rezultātā secinājumi par augšanas procesu lielākoties tiek veikti balsoties uz izmantoto recepti un pēc audzēšanas (pēc cepšanas) novērojumiem.

Protams, zinātnieki viennozīmīgi piekrīt konditoriem, ka audzēšanas (un cepšanas) procesa laikā veikti novērojumi var sniegt unikālu informāciju recepšu uzlabošanai. Tas ir novedis pie jaunu zinātnisko instrumentu radīšanas, kurus dēvē par vides transmisijas elektronu mikroskopiem, kuri mums ļauj pētīt kristālu augšanas procesu reāllaikā. Šie instrumenti apvieno mūsu spēju audzēt kristāliskus nano izmēra materiālus ar spēju pētīt to augšanas procesu ar atoma izšķirtspēju.

Šī disertācija apkopo visjaunākos rezultātus no reāllaika *in situ* pētījumiem specifiskai kristālisko materiālu grupai, kurus dēvē par nanovadiem (nanoizmēra, vadiem līdzīgi kristāli). Manis veiktie pētījumi ir fokusēti uz nanovadiem, kas sastāv no III grupas un V grupas elementiem periodiskajā tabulā. Šīs disertācijas galvenais mērķis ir dot lasītājam fundamentālu izpratni par šo nanovadu augšanas procesu, kas nav iegūstams izmantojot plaši pieejamus sintēzes reaktorus.

List of Publications

This thesis is based on the following publications, referred to by their Roman numerals.
‡ These authors contributed equally.

I **_In situ_ observations of size effects in GaAs nanowire growth**

M. Marnauza, M. Tornberg, E. K. Mårtensson, D. Jacobsson and K. A. Dick

Nanoscale Horizons, 2023, 8(2), 291-296

I formulated the project plan together with K.A. Dick. I carried out experiments together with M. Tornberg and D. Jacobsson. I performed the experimental data analysis and interpretation with input from all co-authors. E. K. Mårtensson and I conceived the model describing the data. Finally, I drafted the manuscript and finalized it based on input from all co-authors.

II **Diameter Control of GaSb Nanowires Revealed by _In Situ_ Environmental Transmission Electron Microscopy**

M. Marnauza‡, R. Sjökvist‡, S. Lehmann, and K. A. Dick

The Journal of Physical Chemistry Letters, 2023, 14(33), 7404-7410

I formulated the project plan and performed *in situ* experiments together with R. Sjökvist. I performed the experimental data analysis and interpretation with input from all co-authors. Finally, I drafted the manuscript together with R. Sjökvist and finalized it based on input from all co-authors.

III ***In Situ* Study of Growth Dynamics in Au-Seeded GaSb Nanowires**

R. Sjökvist‡, M. Marnauza‡ and K. A. Dick

Crystal Growth & Design, 2024, 24(11), 4458-4465

I formulated the project plan and performed *in situ* experiments together with R. Sjökvist. I performed the experimental data analysis and interpretation with input from all co-authors. Finally, I drafted the manuscript together with R. Sjökvist and finalized it based on input from all co-authors.

IV ***In situ* study of axial GaSb/GaAs nanowire heterostructure formation**

M. Marnauza, R. Sjökvist, A. Kraina, D. Jacobsson and K. A. Dick

Manuscript in preparation

I formulated the project plan and carried out the experimental investigation. I performed the experimental data analysis and interpretation with input from all co-authors. Finally, I drafted the manuscript and finalized it based on input from all co-authors.

Publications where I have contributed, but will not be discussed further in this thesis:

V **Growth selectivity control of InAs shells on crystal phase engineered GaAs nanowires**

V. J. Gómez, M. Marnauza, K. A. Dick and S. Lehmann

Nanoscale Advances, 2022, 4(16), 3330-3341

VI **Observation of the Multilayer Growth Mode in Ternary InGaAs Nanowires**

R. Sjökvist, M. Tornberg, M. Marnauza, D. Jacobsson and K. A. Dick

ACS Nanoscience Au, 2022, 2(6), 539-548.

VII **Bismuth-oxide nanoparticles: study in a beam and as deposited**

M. H. Mikkelä, M. Marnauza, C. J. D. Hetherington, R. Wallenberg, E. Mårsell, Y. P. Liu, A. Mikkelsen, O. Björneholm, G. Öhrwall and M. Tchaplyguine

Physical Chemistry Chemical Physics, 2024, 26(13), 10369-10381

VIII **Perfect Zeeman Anisotropy in Rotationally Symmetric Quantum Dots with Strong Spin-Orbit Interaction**

M. Aspergen, L. Chergui, M. Marnauza, R. Debbarma, J. Bengtsson, S. Lehmann, K. A. Dick, S. M. Reimann and C. Thelander

Nano Letters, 2024, 24(26), 7927–7933

Abbreviations

ZB	Zinc-blende
WZ	Wurtzite
HRTEM	High resolution transmission electron microscope
MBE	Molecular beam epitaxy
MOCVD	Metalorganic chemical vapour deposition
ETEM	Environmental transmission electron microscope
CVD	Chemical vapour deposition
MO	Metalorganic
TMGa	Trimethylgallium
TMSb	Trimethylantimony
AsH_3	Arsine
PH_3	Phosphine
VLS	Vapour-liquid-solid
VSS	Vapour-solid-solid
LS	Liquid solid
TEM	Transmission electron microscope
FEG	Field emission gun
STEM	Scanning transmission electron microscope
SAED	Selected area electron diffraction
RGA	Residual gas analyser
SE	Secondary electron
SEM	Scanning electron microscope

ADF	Annular dark field
BF	Bright field
HAADF	High angle annular dark field
FPS	Frames per second
XEDS	X-ray energy dispersive spectroscopy
MEMS	Micro-electromechanical systems
TMP	Turbomolecular pump
DRP	Dry rotation pump
IP	Ion pump
GHS	Gas handling system
MFC	Mass flow controller
PC	Pressure controller
VC	Vapour concentration monitor
PT	Pressure transducer
GT	Gibbs-Thomson
LV	Liquid vapour
TPL	Triple phase line
GPA	Geometric phase analysis
FFT	Fast-Fourier transform

Introduction

At the heart of nearly every modern piece of electronic equipment is a transistor. In simple terms, a transistor is a semiconductor device that can act as a switch for electrical signals. This is made possible by the specific properties of the semiconductor materials that are at the centre of every transistor. The creation of this one device skyrocketed the interest in semiconductors as a materials class. This in turn pushed materials scientists to make smaller and better devices, rapidly going from the macro to micro, and ultimately to nanoscale.[1]

This development sparked an increased interest into understanding the fundamentals of growth and design of semiconductor materials. By downscaling bulk materials to the nanoscale, different material morphologies emerged that are distinguished by their dimensionality and properties.[2–4] Among these, subjectively speaking, the most interesting class of nanomaterials are the so-called nanowires. Nanowires are wire-like nanostructures with a diameter of < 100 nm, while the length can reach up to a few microns.

Since their emergence as a materials system, semiconductor nanowires have gradually increased in popularity due to the plethora of promising applications including, but not limited to, vertical transistors, photodetectors, solar cells and lasers.[2,5] These applications are connected not only to the significant surface-to-volume ratio of nanowires, but also to the more material-specific properties, such as excellent electric transport, ability to form pristine single crystals and, in the case of III-V nanowires, to obtain different crystal structures.[2,5–8]

The III-V nanowires are arguably the most versatile class of semiconductor nanowires, due the vast number of proposed nanowire applications utilizing specifically these materials. This is due to the large number of potential material combinations, among the binary and ternary combinations from group III and V elements, that allow us to design application-specific nanowires.[2] This is where a whole sub-field of nanowire growth was born focused on taming the III-V nanowires, and harnessing their potential as building blocks for next generation electronics. However, in order to utilize their valuable properties we need to understand how the growth conditions relate to the

structure and how this in turn affects the properties of these nanowires. This is where electron microscopes come in.

As opposed to their cousins, the optical microscopes, electron microscopes utilize electrons as the "light source" allowing us to extend the resolution in the sub-nanometre space.[9] This has brought an increased understanding of the crystal growth process, allowing not only for the growth, but also for the characterization of semiconductor nanowires to occur with atomic scale precision. However, up until the last few years we have only been able to examine nanowires after they are fabricated. This means that many of the processes that lead to formation of the final structure remain unseen and up for interpretation. Therefore, the growth reactors where nanowire growth is performed are often regarded as black boxes. In order to address the lack of dynamical information of nanowire growth, modelling in combination with post-mortem electron microscopy investigations is commonly used.[2,10–16] However, this approach can only take us so far. This led to the development of electron microscopes that are able to facilitate nanowire growth, thus leading to *in situ* studies.[17,18]

By conducting *in situ* studies, we can "peek inside the black box" providing a unique insight into the dynamics of nanowire growth. This has enabled us to verify previously theorized concepts of nanowire growth and improve modelling in general.[19–21] However, arguably, the real advantage of *in situ* studies is in the development and study of complex nanowire-based structures and growth phenomena, which the conventional approaches of modelling and post-growth microscopy characterization are unable to address.

Thesis outline

Note that in this thesis, *in situ* studies (conducted by my colleagues and I, as well as other research groups) will often be compared to those using "more standard" growth systems that do not allow real-time observations. To differentiate from the *in situ* studies in the following text these "more standard" growth systems and studies will be referred to as conventional or *ex situ*.

My research aims to expand our fundamental knowledge of III-V nanowire growth. This is done by utilizing the advantages of our *in situ* system to provide real-time observations of nanowire growth dynamics and to put these novel insights into the context of existing knowledge of nanowire growth. This has resulted in four original works on which the thesis is based, which are summarized below.

In **Paper I**, I have examined how the dimensions of Au nanoparticles affect the growth dynamics of GaAs nanowires. This study covered a range of nanowire diameters, where the size effects are expected to start severely affecting the growth dynamics of nanowires. By recording high-framerate videos of the nanowire growth process and constructing a thermodynamic model, I was able to indirectly determine how the reduced nanoparticle size (and nanowire dimensions) affect availability of growth species.

In **Paper II** and **Paper III**, I studied the growth of Au-seeded GaSb nanowires. Here the goal was to provide first-hand experimental data on the interplay between the vapour, liquid and solid phases during growth. This was done by covering a wide range of growth conditions (in terms of precursor partial pressure), and monitoring the effect on nanoparticle and nanowire morphology, as well as growth dynamics. Several of the experimentally determined parameters were subsequently used as inputs for a Monte-Carlo model to simulate the growth of these nanowires. These simulations not only verified the experimentally observed trends, but also provided insight into the kinetics of the growth beyond the experimental temporal resolution.

In **Paper IV**, I combined the knowledge gained from **Papers I - III** about the growth of GaAs and GaSb nanowires, in order to investigate formation of Au-seeded GaSb/GaAs axial nanowire heterostructures. Here, by testing different combinations of growth conditions, I studied how these structures could be formed without kinking. After such conditions were found, the focus was shifted towards examining the dynamics of the nanoparticle and nanowire, as the heterostructure is formed. Based on these observations, it was possible to determine why the III-Sb/III-As heterostructure formation is so challenging and also what it takes to form them.

To provide context to the aforementioned studies and introduce you, the reader, to my field of research, this thesis is split into several chapters. Throughout these chapters, we will collect puzzle pieces that represent the different aspects of knowledge required to open the black box of the III-V nanowire growth. The information contained within these chapters is briefly summarized below.

In Chapter 1, I provide background on III-V nanowires as a material system. This is followed up by a discussion on conventional equipment required to facilitate their growth. I conclude this chapter with a brief description of the thermodynamics behind nanowire growth and the layer-by-layer growth process.

In Chapter 2, I will introduce the instrument that I exclusively used to conduct the *in situ* studies, namely, the environmental transmission electron microscope. Here, I will first introduce the relevant aspects of transmission electron microscopy required to understand the discussion of my experimental results. After this, I will provide a brief description of the gas handling system that controls the environmental part of our

microscope. This will provide a grasp on how the precursor supply to the microscope is controlled and monitored.

In Chapter 3, the nucleation of Au-seeded GaAs nanowires in the environmental transmission electron microscope is described. Thereafter, the contents of **Paper I** are discussed describing the experimental results and the thermodynamic model used to analyse size effects in GaAs nanowire growth.

In Chapter 4, I focus on an extensive description of the Au-seeded GaSb nanowires that is based on the contents of **Papers II** and **Paper III**. Within this chapter, I discuss the two different methods used to facilitate growth of said nanowires, namely, direct nucleation of GaSb nanowires and GaAs/GaSb heterostructures. Subsequently, the interplay among vapour, liquid and solid phases is discussed by examining the nanoparticle, nanowire morphology and growth dynamics. The chapter is concluded by briefly examining the results of the Monte-Carlo model developed to verify the experimental trends.

In Chapter 5, I present the formation of GaSb/GaAs axial nanowire heterostructures based on the content of **Paper IV**. In the beginning of this chapter, I discuss the process and different recipes that were used to ultimately arrive at a growth procedure that allowed us to grow these heterostructures. The second part of this chapter is dedicated to discussing the growth dynamics of GaSb/GaAs axial nanowire heterostructures and relating this to knowledge of GaSb and GaAs nanowire growth established in the previous chapters.

Lastly, in Chapter 6, I summarize the contents of this thesis. Here I aim to present ideas for future *in situ* projects and give a brief outlook on the future of *in situ* studies.

1 Background

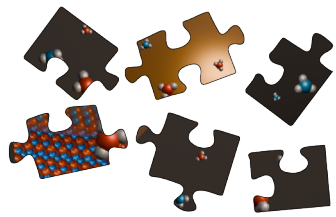

This chapter gives the background of key properties of III-V nanowires as well as the basic knowledge required to interpret the nanowire growth process. We will first start by taking a look at III-V semiconductor nanowires as a material system, which will be followed up by discussing the crystal growth in a conventional system and the related thermodynamics. At the end of this chapter we will combine all this knowledge, and discuss the basic concepts of nanowire growth on which this work is based.

1.1 Group III-V nanowires

A special subclass of semiconductor nanowires are the group III-V nanowires. In the simplest of cases when referring to a III-V nanowire the people in nanowire community refer to a stoichiometric binary compound comprised of group III and group V atoms in a 1:1 ratio. In this thesis, examples of this are GaAs and GaSb nanowires. Although comprised of far less abundant elements than Si nanowires, these materials have attracted attention due to their versatility as a materials system and often superior electrical properties.[2] Consequently, III-V nanowires have been demonstrated as an excellent candidate material system for a variety of applications such as field-effect transistors, lasers and solar cells to name a few.[2,5] The usefulness of III-V nanowires is often directly related to their properties such as polytypism (the ability to change crystal structure) and the ability to form epitaxial, defect-free heterostructures as briefly discussed in the following subsections.

1.1.1 Polytypism

An interesting property of III-V materials is that in bulk phase they are generally found in the cubic zinc-blende (ZB) crystal phase, with the exception of nitrides.[22] However, when their dimensions reach the nanoscale it becomes possible to grow them in the otherwise metastable hexagonal wurtzite (WZ) crystal phase.[16,20,23] This is possible due to lower surface energies of the WZ phase, which play an increasingly significant role at the nanoscale, where the surface-to-volume ratio is large in comparison to bulk

materials.[20,22] Regardless of the specific polytype, nanowire growth is most commonly observed to occur along the ⟨1̄1̄1̄⟩ and ⟨000 1̄⟩ type directions for ZB and WZ, respectively.[2,20,22,24–26] In these directions both ZB and WZ are close-packed, but also polar as can be seen from Figure 1.1, with B-polar growth directions (those terminated by group V atoms) being most common.[24,26] Since the latter chapters of this thesis touch upon both ZB and WZ polytypes it is therefore instructive to examine how these crystal structures differ.

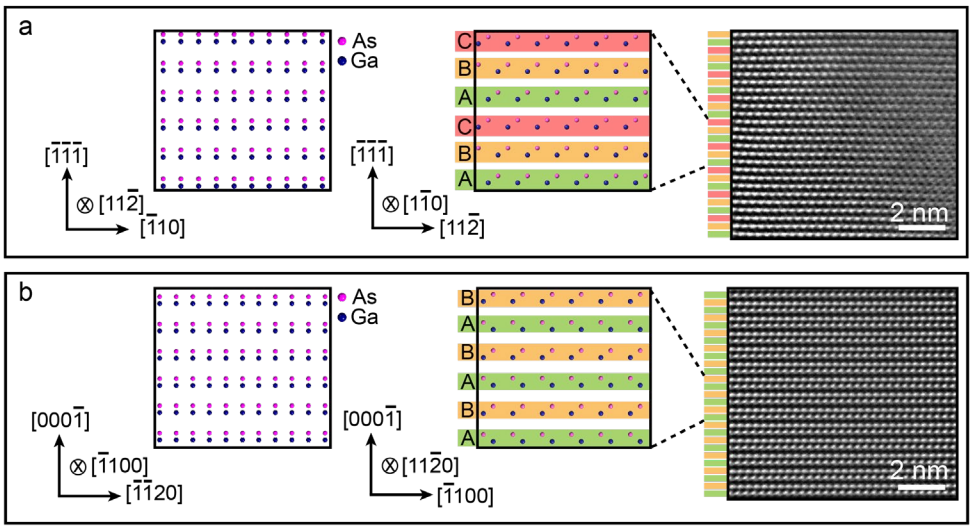

Figure 1.1 Polytypism in III-V nanowires. (a) GaAs in ZB crystal phase depicted from two typically-investigated viewing directions. (b) GaAs in WZ crystal phase depicted from two typically-investigated zone-axes. The images of atomic stacking are reproduced using Vesta software.[27]

Figure 1.1 (a) depicts the atomic stacking sequence of ZB GaAs, while in Figure 1.1 (b) the atomic stacking of WZ GaAs is shown. As can be seen the two crystal structures are nearly indistinguishable when viewed along ⟨11 2̄⟩ and ⟨1 1̄00⟩ directions in ZB and WZ respectively. Therefore, it is much more practically useful to view these structures oriented to ⟨1 1̄0⟩ and ⟨11 2̄0⟩ zone-axes for ZB and WZ, respectively. If we start by examining the ZB crystal structure in panel (a), we can observe the characteristic ABCABC stacking sequence along the ⟨111⟩ type directions, where each letter refers to a bilayer of atoms. Here each atomic bilayer corresponds to a {111} crystal plane. As this polytype is based on a repeating stack of three bilayers and is a cubic crystal structure, it is termed 3C. Both in the crystal model and in the high resolution transmission electron microscope (HRTEM) images in Figure 1.1 (a), it gives an appearance of diagonal stacking. However, if we examine the WZ crystal structure in panel (b), the layers alternate directions with each layer rotated 60° with

respect to the previous one around the plane normal ($[000\bar{1}]$ direction in the schematic). This results in the characteristic ABABAB stacking of WZ that in the model and the HRTEM image shown in Figure 1.1 (b), gives an appearance of a zig-zagged stacking. Here each atomic bilayer corresponds to a $\{0002\}$ plane. Due to the repeating stack of two bilayers and WZ being in a hexagonal crystal structure, this is termed 2H stacking.

In addition to the aforementioned ZB and WZ crystal phases, several higher order polytypes have been demonstrated to occur in III-V nanowires such as 4H and 6H.[28–30] Similarly to WZ these are hexagonal polytypes; however, as opposed to WZ where the period is comprised of two bilayers (AB), in the case of 4H and 6H one repeating unit is comprised of four (e.g. ABAC) and six (e.g. ABCBAC) bilayers respectively. These more uncommon phases (as well as WZ in nanowires in general) are metastable and theorized to be attainable for a very narrow range of conditions. They are often seen in III-V nanowires as a transient crystal phase (as we will also see in Chapter 5 for GaSb/GaAs heterostructures).[28]

1.1.2 Nanowire heterostructures

One of the key advantages of using nanowires as building blocks for advanced electronics is the ability to construct epitaxially-matched heterostructures. Due to the small dimensions of nanowires they are good at strain relaxation, thereby allowing epitaxial matching even between heavily mismatched structures.[31,32] Generally, we can separate heterostructures into two categories depending on how the heterostructure is incorporated into the nanowire geometry.

First are the axial heterostructures, where nanowire composition is changed along the growth direction. A schematic example of such a heterostructure is shown in Figure 1.2 (a). Here initially a nanowire with material composition "A" is grown, which is then followed by changing growth species to grow material "B". Notably, although atomically-sharp axial heterostructures have been demonstrated between select materials, formation of axial heterostructures between arbitrary materials is still a challenging endeavour.[32] Among these challenges is the change in morphology in response to compositional change and the presence of graded, rather than atomically sharp, interfaces between materials. We will examine these challenges in more detail in Chapter 5 for the GaSb/GaAs heterostructures.

Second are the radial (aka core-shell) heterostructures, where the composition is changed perpendicular to the growth direction by covering the initial nanowire core with different composition materials as depicted in Figure 1.2 (b). Here the main

challenge is often balancing the axial and radial growth such that radial growth is favoured. It is worth mentioning that the Figure 1.2 (b) presents an idealized case, where in reality the growth of material "B" would often result in some axial growth (not shown) that would be tapered, since the catalyst particle would be matched in size to the material "A".

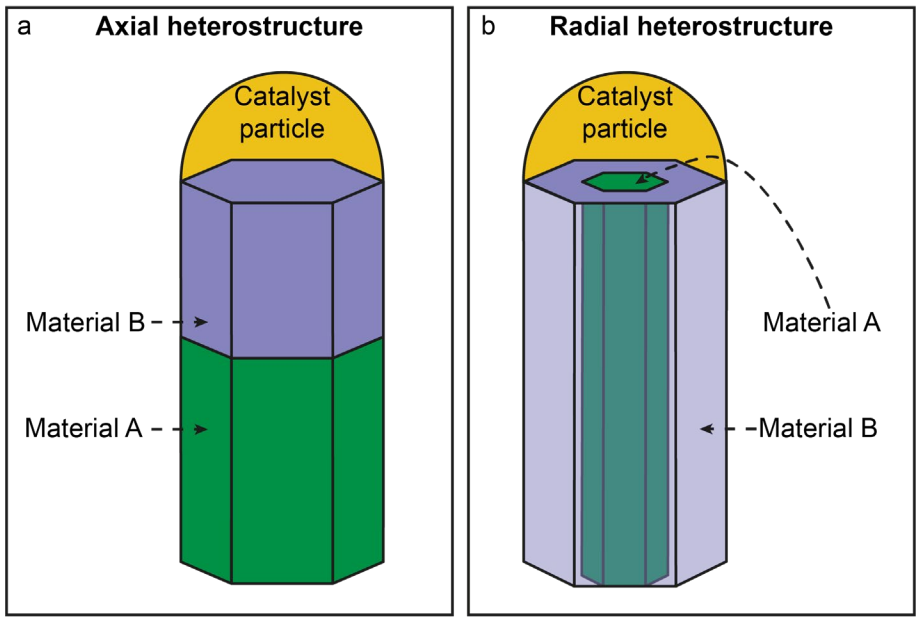

Figure 1.2 Nanowire-based heterostructures. (a) Schematic of an axial nanowire heterostructure, where initially a nanowire of material A is grown. Subsequently material B is grown on top of the initial stem forming a heterostructure. (b) Schematic of a radial heterostructure, where initially a nanowire of material A is grown. This is followed by growing a shell of material B that encapsulates the original nanowire stem.

1.2 Metalorganic chemical vapour deposition

Nanowire growth in general can be conducted using a wide range of physical, chemical vapour or solution based deposition systems.[33] However, when atomic level control of nanowire growth is necessary, molecular beam epitaxy (MBE) and metalorganic chemical vapour deposition (MOCVD) are by far the most popular choices. The work presented in this thesis utilizes The Lund Hitachi HF-3300S environmental transmission electron microscope (ETEM), which (as we will learn more about in the next chapter) is based on an MOCVD system. Therefore, in this section we will focus on the basics of a generic MOCVD system depicted in Figure 1.3.

Generally, an MOCVD reactor consists of a reaction chamber, a susceptor that allows heating of the substrate (a cold wall system is assumed here), a plethora of precursor sources, and an exhaust to get rid of gases after a growth run. What sets MOCVD apart from normal chemical vapour deposition (CVD) techniques is the use of metalorganic (MO) precursors, such as trimethylgallium (TMGa) and trimethylantimony (TMSb). Despite their high toxicity and pyrophoric nature, the use of MO sources is standard procedure when growing III-V materials.[34] This is due to the advantageous properties of MO sources, such as ability to store them at room temperature without degrading over years of storage, and to pyrolyse (break the chemical bond between the metal atom and organic ligands) at desired temperatures for nanowire growth.[34]

Both TMGa and TMSb are found in a liquid phase at room temperature; however, MOCVD relies on a supply of precursors in a gaseous phase to the growth chamber. Therefore, to supply MO precursors to the growth chamber so-called bubblers are utilized. Bubblers are sealed vessels with an inlet valve that is submerged below the liquid level of the MO, and an outlet valve above the liquid level (see Figure 1.3). Inside the bubblers, the precursor (in liquid or solid phase) attains an equilibrium vapour pressure dependent on the bubbler temperature. To create a steady flow of the vapour-containing MO precursors to the growth reactor, a carrier gas (most commonly H_2) is bubbled through the MO. At a set flow and bubbler temperature, this creates a mixture of H_2 + MO that enters the gas line leading towards the growth chamber as schematically shown in Figure 1.3. Note that this is the simplest type of bubbler, and the specific design can vary a lot especially when the MO is in solid rather than liquid phase.[35] Additionally, bubblers are placed in containers, that are very creatively called bubbler baths, within a mixture of glycol + water. The bubbler bath enables temperature control of the glycol + water mixture, which in turn allows control of the vapour pressure and the MO concentration at a set flow of H_2 that will be achieved in the gas lines after the bubbler. In summary, these parameters i.e. carrier gas flow through the bubbler, bubbler temperature, and pressure allow growers to control the amount of MO supplied to the growth chamber.

The other commonly used type of precursors are hydrides such as arsine (AsH_3) and phosphine (PH_3). These already are in a gaseous state and can therefore be directly supplied to the growth chamber without any additional steps. Since conventional MOCVD growth is performed at a constant reactor pressure, ranging anywhere from a few Torr to atmospheric pressure, H_2 is also directly supplied to the growth chamber to make up the growth chamber background pressure.[34]

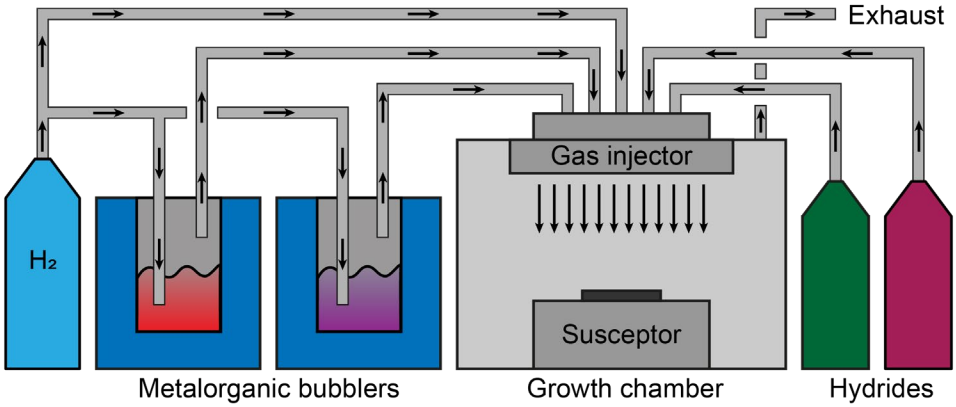

Figure 1.3 Basic schematic of an MOCVD system. Arrows indicate the direction of gas flow in the system.

All the gases eventually meet at the gas injector where they are mixed and injected into the growth chamber. Here a growth substrate is placed on a heated susceptor situated directly below the gas injector. Due to the increased temperature of the substrate, the precursors can undergo pyrolysis (often referred to as cracking). Pyrolysis is thermal decomposition of the MO and hydride sources that occurs via a series of chemical reactions, ultimately allowing the target atom to adsorb onto the substrate. When TMGa and AsH_3 are subjected to growth temperatures in an MOCVD chamber, more than 10 different chemical reactions can take place.[36–38] The desired result in the case of GaAs growth can however be summarized by the following equation:

$$Ga(CH_3)_3 + AsH_3 \rightarrow GaAs + 3CH_4 \uparrow \quad (1.1)$$

As can be seen from Equation (1.1) a substantial amount of carbon atoms are involved in the chemical reactions as a by-product of using MO sources. Carbon atoms can act as amphoteric dopants in III-V materials leading to degraded (or at the least uncontrolled) electronic properties.[34] However, a decrease of C doping in III-V materials has been shown at high AsH_3 pressures (for the specific case of GaAs growth). The proposed mechanism here is that atomic hydrogen generated in the pyrolysis of the AsH_3 can bond with methyl groups to form methane, which is desorbed from surfaces. Therefore, the use of H_2 and hydrides in conjunction with the MO sources also has the added benefit of reducing unwanted carbon doping of III-V materials.

The schematic presented in Figure 1.3 is a simplified depiction of an MOCVD system and does not include gas pathways for additional dilution, mass flow controllers,

concentration gauges, pressure transducers and pressure controllers that are riddled throughout any modern MOCVD system. We will take a more in-depth look at these things in the context of the MOCVD coupled with the ETEM in Section 2.3.

1.3 Thermodynamics of crystal growth

Since we have established the growth system used to facilitate crystal growth, we now need to establish a basic grasp of how crystals nucleate and grow. In this section, I will introduce some the fundamental concepts necessary to understand nucleation and growth. For the thermodynamic description of nucleation the book titled "Epitaxy of Semiconductors" by Udo Pohl is used, which the reader can refer to for more details.[39]

Before getting into nucleation and growth we will first start from a place of relaxation and peace, namely, the equilibrium. Every system if left undisturbed for long enough will eventually reach a state where it will be unchanging with time. Such a state is termed a thermodynamic equilibrium and is characterized by a minimum Gibbs energy G (aka Gibbs free energy). The Gibbs free energy is used to describe the state of a system, which can consist of multiple components. Associated with each component is its chemical potential μ_i, which is a partial derivative of the Gibbs free energy.

$$\mu_i = \left(\frac{\delta G}{\delta n_i}\right)_{T,P,n_{j\neq i}} = \mu_i\left(T, P, x_1, \dots, x_{N_c}\right) \tag{1.2}$$

Therefore, the total energy of a thermodynamic system can be described as a sum of the individual component chemical potentials.

$$G = \sum_{i=1}^{N_c} \mu_i n_i \tag{1.3}$$

For crystal growth to occur a system must be pushed outside of thermodynamic equilibrium by a driving force. Therefore, we are not necessarily interested in determining the absolute value of the Gibbs free energy (and by extension chemical potentials) at each state, but rather the difference in chemical potentials or in other words which way the thermodynamic driving force is leading us. For a phase change between a vapour phase with a chemical potential μ_V, and a liquid phase μ_L, the difference $\Delta\mu_{VL}$, in chemical potentials is the thermodynamic driving force.

$$\Delta\mu_{VL} \equiv \mu_V - \mu_L \tag{1.4}$$

Here it is worth noting that when the thermodynamic driving force $\Delta\mu$, is used to describe a phase change from liquid to solid, the nanowire growth community (and more broadly the CVD community) use the more snappy term of supersaturation. In the spirit of tradition throughout this thesis, the term supersaturation will be used interchangeably to describe the thermodynamic driving force.

Now that there is a driving force for phase change nucleation may occur. In simple terms nucleation is a process in which a new thermodynamic phase is created, which in this thought experiment, is the nucleation of a liquid droplet from vapour. To understand why and when nucleation can happen, we will now examine the energetics behind this process. To do this, we will consider the nucleation of a liquid spherical droplet from a vapour phase (as shown in Figure 1.4 (a)), and as is customary examine it in terms of change in the Gibbs free energy ΔG_N.

$$\Delta G_N = \Delta G_V + \Delta G_S + \Delta G_E \tag{1.5}$$

To describe the energetics of nucleation there are three major components to consider. The first one is ΔG_V, which describes the energy gained by creating a new volume of the more thermodynamically stable phase. However, as the new volume is created, we also create new surfaces and interfaces that previously did not exist, which invokes an energy cost that is summarized in the term ΔG_S. Lastly, there is an additional term ΔG_E, describing the elastic stress if the nucleus is subject to strain (think nucleation of a new material on a substrate with different lattice spacing). Similarly to ΔG_S, the elastic stress term ΔG_E invokes an energy cost, and in extreme cases can also suppress nucleation. However, for the case of an unstrained liquid spherical nucleus from a vapour phase, the term ΔG_E does not play a role, and therefore will be omitted for the rest of the discussion.

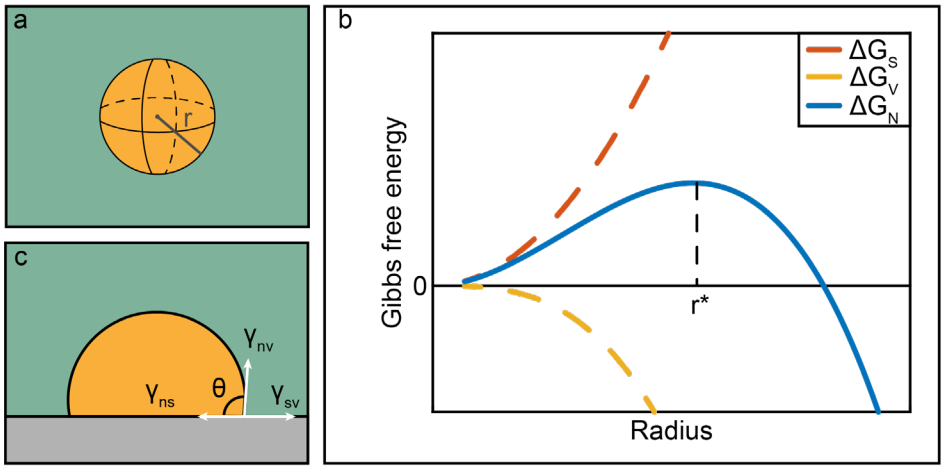

Figure 1.4 Schematics of the energetics of isotropic nucleation. (a) Schematic of a nucleation of an isotropic nucleus from a vapour phase. (b) Schematic of a typical Gibbs free energy curve for the nucleation process, where the elastic stress term is omitted. (c) Schematics of an isotropic, heterogeneous 3D nucleation on a solid substrate.

Now assuming that the liquid nucleus is isotropic with a surface energy, γ, we can expand the Equation (1.5) into the following equation:

$$\Delta G_N = \Delta G_V + \Delta G_S = -\frac{4\pi r^3}{3\Omega_L}\Delta\mu + 4\pi r^2\gamma \qquad (1.6)$$

Here r is the radius of the nucleus while Ω_L, is the volume of monomers, where monomer refers to the smallest indivisible unit undergoing phase change (in III-V nanowire growth this would be an atomic pair of III-V atoms). As can be seen from Equation (1.6), the first term that describes volume is negative as it reduces the overall energy of the system, whereas the second one is positive and describes an energy cost of forming new surfaces as discussed above. Both terms are in competition and for small radii the surface-to-volume ratio is large; therefore, the surface term dominates leading to an increase in the overall Gibbs free energy as depicted in Figure 1.4 (b). However, if larger nuclei can form, the volume term gradually offsets the energy cost of creating new surfaces until ΔG_N reaches a critical radius r^*. At this point the volume term starts to dominate, and the Gibbs free energy of the system is dramatically reduced if the radii of nuclei further increase. In simple terms, nuclei with a radius smaller than r^* are unstable and tend to disband, whereas nuclei with a radius larger than r^* are more likely to grow as it is energetically favourable. We can find the critical radius by calculating a

derivative of ΔG_N, with respect to radius, and setting it equal to zero. The critical nucleus size is then given as:

$$\frac{d\Delta G_N}{dr} = 0 \;\Rightarrow\; r^* = \frac{2\Omega_L \gamma}{\Delta\mu} \tag{1.7}$$

After inserting the critical radius back into Equation (1.6) we can then obtain the Gibbs free energy required for nucleation, i.e. the nucleation energy:

$$\Delta G_N^* = \frac{16\pi\gamma^3 {\Omega_L}^2}{3\Delta\mu} \tag{1.8}$$

We can easily extend the case for isotropic nucleation described in Equation (1.6) to heterogeneous 3D nucleation on a solid substrate as schematically shown in Figure 1.4 (c). As before we have an overall energy-reducing volume term and an energy cost associated surface term, albeit with more interfaces created during the nucleation process:

$$\Delta G_N = \Delta G_V + \Delta G_S = -V\frac{\Delta\mu}{\Omega_L} + A_{nv}\gamma_{nv} + A_{sv}\gamma_{sv} + A_{ns}\gamma_{ns} \tag{1.9}$$

Here, V refers to the specific volume of the created nucleus (depending on its geometrical shape), with A_{nv}, A_{sv}, A_{ns} and γ_{nv}, γ_{sv}, γ_{ns} referring to the nucleus-vapour, solid-vapour, nucleus-solid interface areas and surface energies, respectively. Moreover, the surface energies are related through the Young equation:

$$\gamma_{sv} = \gamma_{ns} + \gamma_{nv}\cos\theta \tag{1.10}$$

Here, theta θ refers to the contact angle at the triple phase line between the nucleus, substrate and vapour. The Young equation is most commonly referred to when discussing thin film growth modes as the balance of energies dictates whether thin film formation happens layer-by-layer (Frank-van der Merwe), as isolated islands (Volmer-Weber) or a mixture of both (Stranski-Krastanow).[39]

1.3.1 Vapour-liquid-solid mechanism

To grow vertical nanowires instead of thin films, we need to manipulate the surface energies such that nucleation and growth are significantly easier along a specific crystallographic direction. This is achieved through using solid or liquid catalyst materials, in the form of nanoparticles placed on the growth substrates that drive the formation of nanowires.

Depending on the phase of the nanoparticle used to catalyse nanowire growth, we refer to nanowire growth occurring via the vapour-liquid-solid (VLS) or vapour-solid-solid (VSS) mechanism. In these methods the vapour refers to the phase of precursors, the liquid/solid refers to the state of the catalyst nanoparticle, whereas the solid refers to the nanowire crystal. In this thesis, however, I have exclusively used the VLS method to carry out nanowire growth. Therefore, in this subsection we will cover the basics of this method while referring to the basic thermodynamic concepts introduced previously.

The VLS mechanism was originally proposed by Wagner and Ellis back in 1964 for microscale Si whiskers.[40] The VLS method relies on supplying vapour phase precursors to a growth chamber where a growth substrate with particles (self-assembled from annealing thin films or deposited pre-growth) that serve as catalysts for the growth of nanowires.[6] Nowadays, a wide array of options are available for the nanoparticle material, with Au nanoparticles being the most common choice.[6,41] This is a direct consequence of Au forming low temperature liquid alloys with group III and V elements, at temperatures that are suitable for III-V nanowire growth.[6,41,42] Additionally, Au does not easily oxidize when exposed to air and it can be used for VLS and VSS growth (depending on the used growth temperature).

The basic steps of Au-seeded GaAs nanowire growth are schematically shown in Figure 1.5. For the typical growth temperatures that are used for the growth of III-V nanowires, Au nanoparticles are solid. However, as the growth precursors are supplied to the growth chamber the Au nanoparticle forms an alloy (predominantly with the group III element), which lowers its melting point turning the nanoparticle liquid.[6] At some point, the now-liquid alloy reaches a point where group III and V atoms added from the vapour make the particle supersaturated, which may result in the nucleation of a solid GaAs crystallite. If the supply of growth precursors and elevated temperature are maintained, this will result in a steady-state growth process as depicted in Figure 1.5. In Section 3.1 and Section 4.1.1, we will examine the nucleation process in the more practical terms of a real *in situ* experiment for Au-seeded GaAs and GaSb nanowires, respectively.

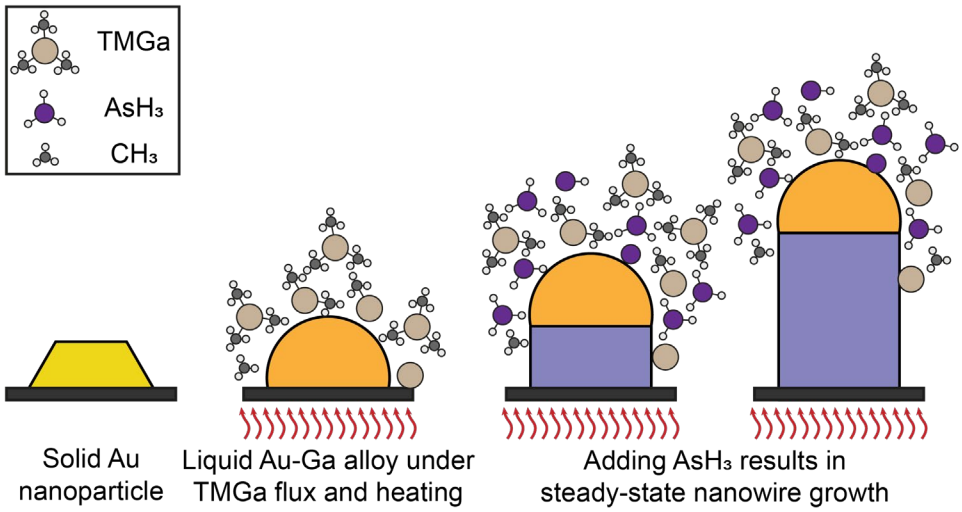

Figure 1.5 Schematics outlining the basic principle of VLS growth mechanism using growth of Au-seeded GaAs as an example. In the first step solid Au nanoparticles reside on the growth substrate. When the substrate is heated to a sufficient temperature and TMGa is supplied to the growth chamber the precorsor can pyrolyse, freeing Ga atoms that can alloy with the Au nanoparticle turning it into a liquid Au-Ga alloy. In addition to the supply of temperature and TMGa precursor, if AsH_3 is added this can result in nucleation and steady-state nanowire growth.

Note that the VLS method is not limited to only using a foreign metal nanoparticle as a growth catalyst. Over the past years the use of "self-catalysed" growth approaches have increased in popularity.[41] Here the growth still follows the basics of VLS method by having a vapour, liquid and a solid phase present; however, the liquid "catalyst" is a nanoparticle of the group III element (Ga or In).[41,43] The main advantage of a self-seeded growth approach is an easier integration with Si for device fabrication, as Au is notorious for forming deep level charge carrier traps that hinder electron transport.[44] The main drawback of the "self-catalysed" approach is the possibility for the nanoparticle to be incorporated into the nanowire during growth, which sets more strict requirements for the usable growth conditions.

1.3.2 Layer-by-layer growth

As we learned in previous sections, phase change requires a thermodynamic driving force. In a steady-state VLS growth process there exists a thermodynamic driving force for the material in vapour phase, with the chemical potential μ_V, to be moved to liquid phase, with chemical potential μ_L, and to crystallize in a solid phase nanowire with chemical potential μ_S, as shown in the following equation:

$$\mu_V > \mu_L > \mu_S \tag{1.11}$$

However, to accurately describe the nanowire growth process thermodynamics are often insufficient, and we also have to consider kinetics. In simple terms, I like to think as thermodynamics being the driving force behind any phase transformation and kinetics being the energy barrier standing in the way i.e. defining rates at which processes happen.

Even though there are a plethora of processes to consider during nanowire growth, most modelling efforts focus on examining processes occurring at the liquid-solid (LS) interface such as nucleation and layer-by-layer growth. In part, this is done to reduce complexity of the models, but also because these processes have a strong impact on compositional and crystalline purity of the nanowire. If we only consider thermodynamics for crystallization to occur, the supersaturation, $\Delta\mu_{LS}$, has to be:[45]

$$\Delta\mu_{LS} = \mu_L - \mu_S > 0. \tag{1.12}$$

However, if we also consider the kinetics, we have an additional constraint that needs to be overcome, i.e. the nucleation barrier (similar to the case of isotropic nucleation that we examined before). In order to understand the interplay between kinetics and thermodynamics, modelling is often utilized.[13,46–49]

If the nanowire growth is modelled, specifically, by examining the supersaturation, $\Delta\mu_{LS}$, as a function of time during the layer-by-layer growth process, a characteristic saw tooth profile can be obtained as shown in Figure 1.6 (a). Here we can observe the supersaturation as a function of time for a steady-state nanowire growth process, with nucleation events marked by arrows. Furthermore, we can identify two distinct processes that repeat in a cyclic manner throughout the growth. If we examine the area outlined by the grey box in Figure 1.6 (a), we can see that at some point in time there is a gradual increase in supersaturation. As the supersaturation increases (for example by accumulating more material in the catalyst nanoparticle), a critical point will be reached whereby nucleation can occur. This process where material accumulates is termed incubation (sometimes referred to as waiting time). When nucleation has occurred, new III-V atomic pairs can be easily added, since the kinetic barrier for this process is low, until this new layer is finished.[22] This process is termed step-flow (sometimes also referred to as layer-propagation). After nucleation (and during the step-

flow process), the nanoparticle is in a depleted state, meaning that the supersaturation is not sufficient to overcome the nucleation barrier. Therefore, after the step-flow process is complete, the nanoparticle enters the incubation process again to increase supersaturation until a new nucleation event can occur. Under steady-state conditions, these processes (incubation and step-flow) repeat in a cyclic manner resulting in nanowire growth.

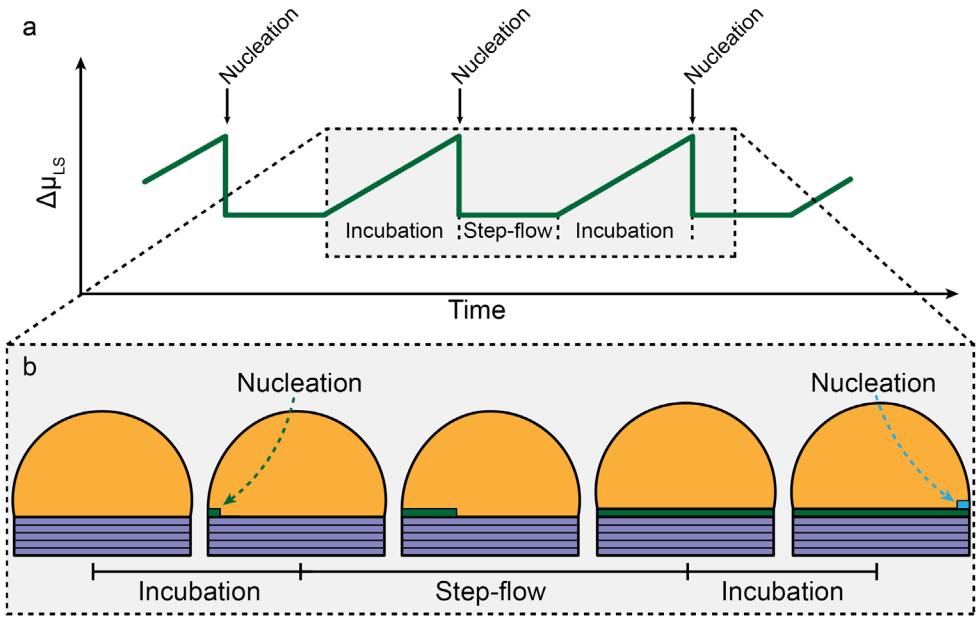

Figure 1.6 Layer-by-layer growth process. (a) Supersaturation of a steady-state nanowire growth process as a function of time with nucleation events marked by arrows. The grey box with dashed outline marks the region depicted in panel (b). (b) Schematic of the nanowire layer-by-layer growth process observed during *in situ* studies illustrating how incubation, nucleation and step-flow processes correlate with modelled supersaturation. Yellow is used to depict a liquid Au nanoparticle, whereas purple depicts the grown III-V nanowire. Green and blue mark the new layers formed during the examined growth time-frame.

In the recent years, there has been a big leap in our understanding of nanowire growth thanks to the introduction of *in situ* systems. This also has made a significant impact on how modelling of growth is carried out, allowing us to develop and improve the models based on real-time experimental observations of nanowire growth.[19,21,50,51] With this in mind we need to bridge the gap between kinetic and thermodynamic modelling of the layer-by-layer growth, and experimental observations. In Figure 1.6 (b) the "*in situ* view" of the layer-by-layer growth process from Figure 1.6 (a) is depicted.

Here the incubation process can be observed as the time that it takes for a new crystalline island to nucleate on top of a previously flat LS interface as schematically

depicted in Figure 1.6 (b). It is important to note here that the observed island is by no means the critical nucleus, which is hard to visualize during growth due to insufficient spatial and temporal resolution.[52–54] However, after the creation of the critical nucleus there is a large driving force to expand the nucleus into a larger crystalline island (until a depleted state is reached), which is what we observe *in situ*. The nucleation concludes the incubation process and simultaneously marks the beginning of the step-flow process. Here the newly-nucleated island gradually expands across the LS interface until it is finished (and a flat LS interface is established), eventually starting a new incubation process.

As a last remark in this section I have to highlight the works by Harmand et al.[19] and Malliakal et al.[21] as these two papers have had a significant impact on my research. These studies were among the first to combine atomic resolution layer-by-layer growth studies of Au-seeded III-V nanowires with growth modelling. In the work by Harmand et al., morphology and surface energies of the growing layer were examined showcasing the dynamics of the step-flow process.[19] Maliakkal et al. were able to demonstrate the independent nature of incubation and step-flow processes, showing that the incubation process is predominantly controlled by the group III precursor and the step-flow process by the group V precursor.[21]

The aforementioned research articles marked the state-of-the art of *in situ* studies in III-V nanowires when I started my PhD, and were among the first papers I read. In Chapter 3 we will see how the layer-by-layer growth was used as a means to study size effects in GaAs nanowires, while Chapter 4 will show experimental observations and modelling of the growth dynamics of GaSb nanowires.

2 Environmental transmission electron microscopy

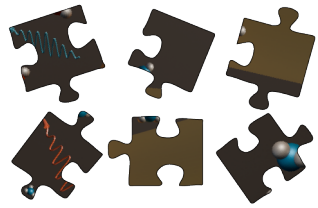

In this chapter we will discuss the experimental setup used to facilitate *in situ* nanowire growth. We will begin our discussion by examining some of the pertinent aspects of a transmission electron microscope (TEM). Subsequently, we will examine special features and considerations that one has to keep in mind when performing *in situ* studies. At the end of the chapter we will discuss the beating heart of The Lund Hitachi HF-3300S environmental TEM (ETEM), namely the gas handling system.

2.1 Transmission electron microscope

In this section we will examine the TEM as an imaging system, and discuss the detectors and types of contrast associated with TEM imaging of nanoscale samples. This section is not meant as an exhaustive description of the basic operation of a TEM, but rather a reflection on the most important concepts. For more detailed information the reader is directed to the fantastic textbook by Williams and Carter, which is also used as the main reference in this chapter.[9]

2.1.1 Imaging system

In this section we will examine the TEM as an imaging system from top to bottom covering the electron source, different lens systems and apertures found in the TEM. The schematic of The Lund Hitachi HF-3300S is shown in Figure 2.1. The topmost part of the microscope is called the gun chamber as it contains the electron source, which can be sealed off from the rest of the column using a gun valve. As an electron source, this microscope uses a cold field emission gun (FEG). The cold-FEG offers superior brightness and minimal energy spread as opposed to Schottky FEG (which is

operated at elevated temperatures) or a thermionic gun (which uses thermionic emission rather than field emission to generate electrons). However, in comparison to the other electron sources cold-FEG requires the highest vacuum to operate (lowest pressures). We will discuss the implications of this for *in situ* experiments in Section 2.2.

After the gun chamber, we find the condenser lens system that forms the electron probe. The condenser lens system is adjacent to the condenser aperture, that allows to limit the electron dose that will reach the sample. A large condenser aperture results in a larger electron dose, which generally can improve signal-to-noise ratio in images; however, increased electron dose can lead to sample damage. Additionally, the use of smaller apertures allows to limit the amount of high angle electrons used to probe the sample.

Moving downwards in the column there is an additional aperture used when the microscope is operated as a scanning transmission electron microscope (STEM). Similar to the condenser aperture it allows to affect the electron dose and limit the amount of high angle electrons that reach the specimen.

If we continue moving down the column, we arrive at the objective lens system. The objective lens system is split between the area above and below the sample forming the pole-piece gap. The objective lens is responsible for image formation with the objective aperture, situated below the sample, enabling bright and dark field imaging of samples. These imaging modes enhance diffraction contrast (discussed in Section 2.1.4) and are highly useful for investigating crystalline samples. In the case of III-V nanowires exhibiting polytypism field imaging, especially dark field, is used to identify the location of a specific crystal phase in the nanowires.[50]

To improve the spatial resolution the microscope is fitted with a CEOS BCOR image corrector. This is an incredibly complex piece of instrument, but in a few words it allows us to correct the axial aberrations induced by the objective lens up to the 4^{th} order in addition to correcting the off-axial coma aberration up to the 3^{rd} order, through the use of several hexapole correctors.[54,55]

After the image corrector, we can see the selected area aperture, the intermediate lens system, and the projector lens system. As the name strongly implies the selected area aperture can be used to carry out selected area electron diffraction (SAED) imaging of samples. This method is used to acquire diffraction patterns over a large sample area (determined by the aperture size) to determine sample crystallinity. Lastly, the intermediate lens system in tandem with the projector lens system is responsible for providing the majority of the magnification in TEM imaging.

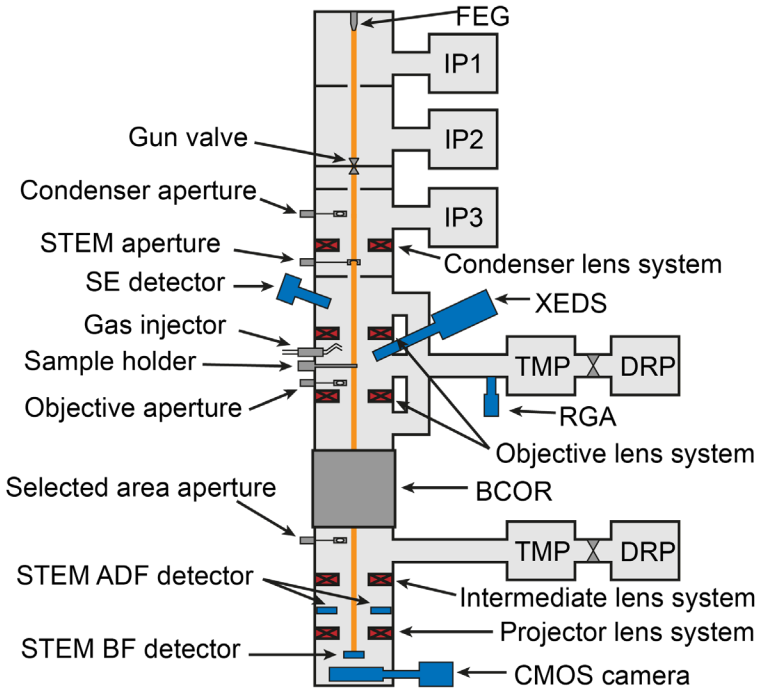

Figure 2.1 Schematic of The Lund Hitachi HF-3300S microscope. Detectors are shown in blue, while the electron beam is shown in orange. Note that lenses are shown as lens systems for simplicity rather than showing each individual lens, and are depicted using red rectangles with crosses.

2.1.2 Detectors

In this section we will examine the detectors available in The Lund ETEM, which are depicted in blue in Figure 2.1. Since the residual gas analyser (RGA) is more relevant in the context of *in situ* experiments it will be discussed in Section 2.3.

In the column, above the pole-piece gap the secondary electron (SE) detector is located. This type of detector can typically be found in scanning electron microscopes (SEMs). Secondary electrons yield information of the sample morphology, which in TEM provides valuable complementary information about the specimen since TEM images depict a 2D projection of the investigated samples.[56] However, the interpretation of SE images in TEM is quite complex as the electron beam penetrates the sample and is transmitted through the specimen, therefore giving signal simultaneously from the bottom and top of the sample. The SE detector is used when the TEM is operated in STEM mode, where instead of illuminating the sample with a parallel beam the sample is raster scanned with a relatively small probe.

When operating the microscope as a STEM, in addition to the SE detector, we can also utilize both the annular dark field (ADF) and bright field (BF) detectors. Depending on the chosen microscope settings (camera length) the ADF detector can be used to detect electrons scattered to high angles. To indicate this operational condition the ADF detector is then termed a high angle annular dark field (HAADF) STEM detector. The electrons scattered to high angles contain information about atomic mass and thickness of the sample excluding diffraction and phase contrast (see Section 2.1.4), which allows us to infer information about sample composition (provided thickness is uniform).

At the very bottom of the TEM column, we find the Gatan OneView IS camera. This, in my personal opinion, is the most indispensable detector of the whole TEM column as it allows acquisition of HRTEM images, but more importantly videos. The camera can be operated at a variety of frame rate/pixel resolution combinations ranging from 25 frames per second (FPS) recording at 4K resolution all the way to 300 FPS acquisition rate at 512 x 512 pixel resolution.

If we take a step back and once again examine the pole-piece gap of the ETEM, we can observe that opposite the sample holder the X-ray dispersive spectroscopy (XEDS) detector is positioned. Nowadays, XEDS detectors are a staple detector in most electron microscopes as they enable compositional analysis of samples, which is an invaluable piece of information also during *in situ* studies. Due to the importance of this detector, we will briefly examine how X-rays are generated and how the quantification of X-ray data is carried out.

2.1.3 Mechanism of X-ray generation in electron microscopy

When the electron beam interacts with a sample electrons can be scattered inelastically. In Figure 2.2 (a) the mechanism for generating characteristic X-rays is shown. A primary beam electron has a chance to collide with an inner shell electron (1), ejecting it (2), while the primary beam continues on a changed trajectory (3). After this collision the inner shell of the atom contains a hole leaving the atom in an excited state. The ionized atom can minimize its energy by filling the inner shell vacancy with an electron from an outer shell (4). This transition is accompanied by an emission of a characteristic X-ray (5) or an Auger electron (not depicted in the schematic). The energy of the characteristic X-ray is unique to a specific transition between electron shells in a particular atom making them a sort of “fingerprint” of the sample. Due to this, the characteristic X-rays can be used for quantification of sample composition with the most common being the Cliff-Lorimer ratio technique as shown in Equation (2.1).

$$\frac{C_A}{C_B} = k_{AB}\frac{I_A}{I_B} \tag{2.1}$$

Here the C_A and C_B are atomic percent, of elements A and B with measured characteristic intensities I_A and I_B in the XEDS spectrum. These are related by a factor k_{AB} that is termed the Cliff-Lorimer factor or simply the k-factor. The k-factor varies depending on the used TEM and XEDS setup as well as the used acceleration voltage, and therefore is specific to the used experimental setup.[57,58] However, often theoretical k-factors are used for quantification, which is also the case for XEDS data presented in this thesis. The theoretical k-factors are estimated using element-specific parameters to circumvent the need for experimental standards prior to performing XEDS analysis.[57–59]

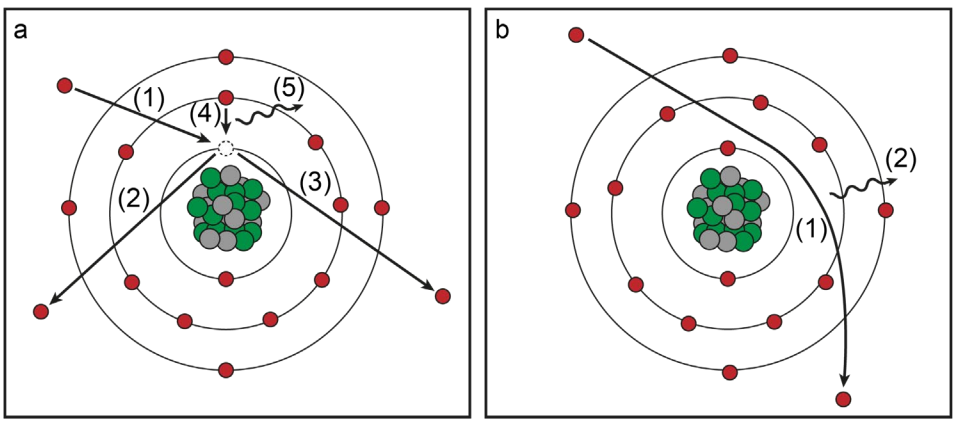

Figure 2.2 Mechanism of X-ray generation in electron microscopy. Here the red circles respresent electrons, grey circles represent neutrons, and green circles represent protons. (a) Mechanism of generating characteristic X-rays. (1) Primary beam electron collides with an inner shell electron of the sample atom. (2) Due to this collision the inner shell electron is ejected, while (3) the primary beam electron continues on a changed trajectory. (4) The atom is in an excited state whereby energy can be reduced if a higher shell electron fills the created vacancy at the inner shell. (5) The excess energy released in this transition creates a photon that is the characteristic X-ray. (b) Mechanism of creating bremsstrahlung. (1) Primary beam electron is attracted by the positive nucleus resulting in it slowing down and changing trajectory. (2) The energy loss during braking creates the continuous bremsstrahlung.

In addition to the characteristic X-rays we also have to consider bremsstrahlung (braking radiation) for which the mechanism is schematically shown in Figure 2.2 (b). Bremsstrahlung is generated when primary beam electrons undergo a change in momentum due to the Coulomb interaction between the beam electrons and the positively charged atomic nucleus (1). During this interaction the electrons lose energy and may emit X-rays (2). The energy of these X-rays depends on the strength of the

interaction and form a continuous background in the XEDS spectra (although the background is low relative to the characteristic peaks in the case of thin samples such as the nanowires investigated in this thesis).

2.1.4 Contrast types in transmission electron microscopy

As a part of my research imaging and *in situ* video acquisition were most often carried out by operating the microscope in TEM mode. Therefore, it is prudent to discuss the different types of contrast that contribute to the final image of our samples. Whenever an electron wave interacts with a specimen it can change both its amplitude and phase with both of these changes giving rise to image contrast. Naturally, we then separate the types of contrast observed in TEM images broadly as amplitude and phase contrast.

Amplitude contrast results from variation in atomic mass or thickness of the samples (or a combination of both). In practice, whenever regions of a TEM sample are relatively thicker or of heavier atomic mass they will appear darker in regular TEM imaging, due to additional scattering of electrons.

An additional type of amplitude contrast is the diffraction contrast. As opposed to mass-thickness contrast, which is generated due to incoherent elastic electron scattering, diffraction contrast can be thought of as a special case of amplitude contrast where the scattering occurs at specific angles and is coherent (and elastic). This type of contrast is present in crystalline or poly-crystalline samples since it relies on Bragg diffraction of electron waves on sample atomic planes. Since amorphous samples lack long range ordering of atomic planes diffraction contrast in such samples does not occur. In order to enhance the diffraction contrast, especially when the specimen is aligned to a high symmetry zone-axis, bright and dark field imaging modes can be used. These imaging modes rely on placing an objective aperture on the central (transmitted beam) spot or any diffracted spot, respectively, in the reciprocal space.

Phase contrast can best be described as electron wave interference, since it arises whenever more than one electron beam contributes to the image. In phase contrast constructive or destructive interference of electron waves results in specific image contrast in the form of bright and dark spots, respectively. This type of contrast is why interpretation of TEM images is such a complex endeavour, since phase contrast is extremely sensitive to sample thickness, orientation, focus and astigmatism. However, phase contrast also yields information on the sample atomic structure and gives the highest spatial resolution (of the discussed types of contrast, when the microscope is operated in TEM mode).

Although nearly synonymous with atomic resolution imaging, phase contrast can also often be seen at relatively low magnifications in TEM in the form of moiré fringes or Fresnel fringes. Moiré fringes arise whenever two or more crystalline grains overlap giving rise to a new set of fringes with a spacing that is a convolution of the crystals creating the moiré pattern. Interestingly, moiré patterns are not only limited to TEM and can be often observed in nature, for example when looking at the back of an office chair with a mesh back support. Fresnel fringes are only observable when a sample is out of focus and therefore can be used as a tool for sample focusing. In practice, whenever dark fringes surrounding the specimen are observed this means that the sample is overfocused i.e. the focal plane of the objective lens is below the sample, whereas bright fringes mean that a sample is underfocused i.e. the objective lens focal plane is above the sample.

2.2 *In situ* experiments

The Lund ETEM can be operated as a conventional TEM; however, it can also facilitate *in situ* growth of III-V nanowires as is the focus of this thesis.[17,55,60] In order to do this, the microscope has several unique features that will be discussed in this section. Before we get into these details, we will first qualitatively examine what an *in situ* nanowire growth experiment looks like.

2.2.1 Nanowire growth performed *in situ*

Similarly to conventional nanowire growth, discussed in Section 1.3.1, in order to grow nanowires *in situ* we also need to use a substrate and supply heating. Here this is neatly combined into a single micro-electromechanical systems (MEMS) chip fabricated by Norcada Inc. The MEMS chip with attached contact pads is schematically depicted in Figure 2.3 (a). The chips are made from Si with the central area consisting of a W heating coil embedded between two thin, electron transparent layers of SiN_x that is schematically shown in Figure 2.3 (b). As depicted in panel (c) at the center of the heating coil 19 openings are situated. One such opening is schematically shown in Figure 2.3 (d) with deposited Au nanoparticles. In these openings the SiN_x that surrounds the holes (lighter grey coloured ring) is thin enough to allow atomic resolution imaging. However, the main idea behind using chips with this particular design is that after nucleating nanowires on the SiN_x some of the nanowires will tend to grow over the central part of the opening, as shown in Figure 2.3 (e). Here the

nanowires can be imaged at the highest attainable spatial resolution, due to the absence of the supporting film.

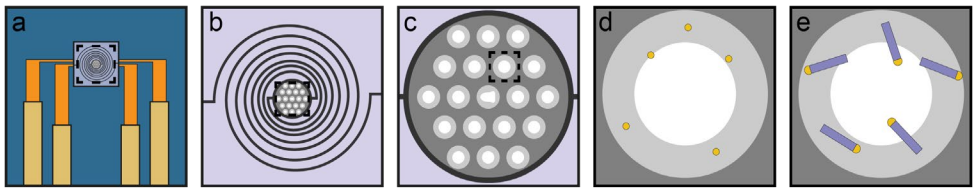

Figure 2.3 Schematics showcasing the Norcada MEMS chips used as a heat supply and substrate. (a) MEMS chip with the contact pads. (b) The central area of the chip containing a W heating coil embedded into SiN_x film. (c) At the center of the thick SiN_x film 19 openings each surrounded by a ring of thin SiN_x film are positioned. (d) Schematic of a single opening, where deposited Au nanoparticles can be seen on the thin SiN_x film. (e) After starting the nanowire growth process the direction of nanowires is random resulting in some nanowires growing into the opening.

In order to nucleate and grow nanowires *in situ* we have to ensure a precursor supply to the growth chamber. This is done via side-mounted gas injectors with two independent gas lines that are pointed directly at the tip of the sample holder as can be seen from the schematic in Figure 2.1. The direct gas injection into the microscope column means that the *in situ* nanowire growth studies are conducted in an open cell system. This has several significant advantages for the growth studies.

First, the spatial resolution attainable during *in situ* growth studies is comparable to the spatial resolution that can be reached during normal imaging conditions resulting in atomic resolution images and videos of growth.[55,60] Secondly, the sample holders used in my experiments allow the samples to be tilted (enabling double tilt functionality). This allows imaging in zone axis conditions that allow us to extract information about crystal structure, composition and growth dynamics (as shown in the following chapters). Lastly, the open cell design means that XEDS can be utilized with good signal to noise ratio, which enables compositional analysis of samples during *in situ* growth studies.[55,60]

It is worth noting that another way to perform *in situ* reactions is using a closed cell system. The closed cell setups have become increasingly popular in the last years, since little to no modification of the microscope column is required to enable *in situ* studies. Contrary to the open cell setups, here the gas (or liquid) environment is contained only at a small area of the holder, which is isolated from the microscope environment by thin electron transparent windows. This allows for higher gas pressures pressures (≥ 1 atm) which can be useful when studying catalytic reactions as it allows *in operando* studies.[61,62]

The main drawback of closed cell systems is the presence of electron transparent windows are used to confine the gas (or liquid) environment to the sample area. This often comes at a price of spatial resolution, limited ability to tilt the sample and more challenging compositional analysis of specimens.[17,63]

2.2.2 *In situ* experiments and their impact on the microscope

As we have established, during *in situ* experiments the gaseous precursors are directly injected into the microscope column near the sample (see Figure 2.1) reaching a maximum pressure of a few Pa.[55] Since the ETEM at its core is a TEM, which requires high vacuum (low pressure) to operate we need to ensure that the high pressure is contained at the sample area only (in the pole-piece).

This is achieved by two turbomolecular pumps (TMPs), backed by dry rotation pumps (DRPs), that are connected not only to the sample area, but also above and below it as shown in Figure 2.1. This is a key component that allows us to achieve up to 6 Pa of pressure at the sample area (without the use of an optional lid that allows to reach estimated pressures of ≈400 Pa), while simultaneously allowing TEM investigation of samples.[55,60] As we already discussed at the beginning of Section 2.1.1 The Lund ETEM uses a cold-FEG, which requires a high vacuum (≈10^{-9} Torr) for continued operation. To enable this several ion pumps (IPs) are positioned at and just below the gun chamber as shown in Figure 2.1.

However, the electron gun can suffer from a slow build-up of surface contaminants that lower the emission and result in gradual reduction of beam intensity during imaging. This process is especially pronounced due to the type of electron source in the ETEM (since the increased temperature of Schottky and thermionic guns mitigate this effect) and when high gas pressures are employed during *in situ* experiments. To clean the tip flashing is utilized, which in this context means reversing the potential and "blowing off" the contaminants (in the case of thermionic sources this is alternatively sometimes done by rapid heating). In extreme cases the flashing procedure has to be repeated approximately every 10 minutes to retain sufficient beam intensity for useful imaging (this timescale varies depending on the gas pressure and composition).

Since *in situ* studies are routinely conducted at elevated temperatures, one must consider the effect of temperature on XEDS acquisition. When the MEMS chips are heated there is an increase in thermal radiation from the chips which effectively reduces the signal to noise ratio and dramatically increases the detector dead time.[60,64] This effect is particularly severe at temperatures >500 °C, which is beyond the temperatures used for nanowire growth in this thesis. Additionally, the heating gives rise to shifts of

the X-ray peaks, which are most severe towards the strobe (aka zero energy) peak. This might sound like a drawback, but it actually gives an opportunity to use the position of the strobe peak as a tool for temperature calibration, which was done before the start of every experiment.[60]

2.3 Gas handling system

The beating heart of the ETEM arguably is the gas handling system (GHS). In the Lund ETEM, this is designed after a conventional MOCVD system meaning that the precursors are supplied to the microscope in a gaseous state. A somewhat simplified schematic of the ETEM gas handling system can be viewed in Figure 2.4, depicting all the available precursors and process gases in The Lund ETEM. As can be seen from the schematic in Figure 2.4 the GHS consists of metalorganic (MO) and pure gases.

To start our discussion on the gas handling system we will start from the precursors and gas canisters shown in the left side of Figure 2.4. Similarly to a conventional MOCVD system described in Section 1.2, H_2 gas is bubbled through the MO bubblers in order to initiate a supply of the metalorganics. The flow of H_2 can be set for each MO bubbler independently via the mass flow controllers (MFCs). Furthermore, the bubblers reside in temperature-controlled bubbler baths schematically shown in Figure 2.4 by the blue rectangles surrounding MO bubblers. The temperature of the bubbler bath determines the MO partial pressure which in turn affects the gas concentration under a set H_2 flow.

Moving further to the right we encounter pressure controller (PC) units that limit gas flow downstream until a set pressure is reached. In the case of gas sources like AsH_3 this does not influence the gas concentration, since it is a pure gas. However, since MOs enter the gas lines as a mixture of MO + H_2 the set pressure of the PC directly affects the MO concentration downstream with lower PC pressures giving higher concentration of MO in the MO + H_2 mixture. In summation, H_2 flow supplied to the bubblers in addition to the set temperature of the bubbler baths combined with the PC set pressure will yield the initial precursor concentration, which is measured by vapour concentration monitors (VC).

After the PCs for both lines the gases can be further diluted by adding additional H_2, which adds another degree of freedom for fine tuning gas concentration in the system. Subsequently, there is a final set of MFCs for each gas line to set the final gas flow that will be supplied to the microscope. The last set of MFCs is also coupled with a pressure

transducer (PT) to determine an approximate pressure in each line, thus enabling us to monitor which part of the GHS is the low pressure side.

Lastly, the GHS also has a common gas vent line, where residual gasses from both the group III and group V line can be vented to avoid pressure build-up. The vent line is a low-pressure region due to a vacuum pump (not shown in the schematic) and scrubber further down the line. The need for venting residual gases arises whenever the additional H_2 dilution is used, since the gas supply to the microscope is relatively much lower than the gas flows used upstream. Whenever additional H_2 dilution is used for both group III and group V lines residual pressure will need to be vented from both lines. This poses a risk of mixing group V and group III precursors in the gas lines and can potentially result in, for example, a back flow of group V precursor into group III line or vice versa. Therefore, **great care needs to be taken whenever dilution of both gas lines is used!**

In Figure 2.4 the black arrows depict the gas flow throughout the gas lines from the high pressure side (bubblers and gas canisters) to the low pressure side (microscope and vent line). The GHS shown in Figure 2.4 based on the gas valve positions is depicted in a state that supports supply of TMGa, TMSb and AsH_3 to the microscope with additional H_2 dilution to both gas lines.

After every experiment or whenever gas lines need to be emptied of current precursors a purging cycle can be carried out using N_2 gas. As can be seen from Figure 2.4 the N_2 gas canister is attached to both the group III and group V lines via gas valves, which allows independent purging of each line. This was utilized when forming the GaAs/GaSb heterostructures discussed in Chapter 4 and GaSb/GaAs heterostructures discussed in Chapter 5, when only the group V precursor was switched, therefore not warranting a purge cycle of the group III line. In order to carry out a purge cycle for either of the gas lines the line length from bubbler to the vent line was filled with N_2. Subsequently, N_2 supply was stopped and the gas line was opened to the vent line until gas line pressure (monitored by PTs) was reduced below a certain value.

In order to monitor the gas composition injected into the microscope a type of mass spectrometer, residual gas analyser (RGA), situated at the exhaust line of the microscope, is used (see Figure 2.1). The use of RGA in conjunction with the knowledge of gas input and data recorded from XEDS and the TEM camera has been a great addition in understanding the nanowire growth process, which will be discussed in more detail in Chapter 5.

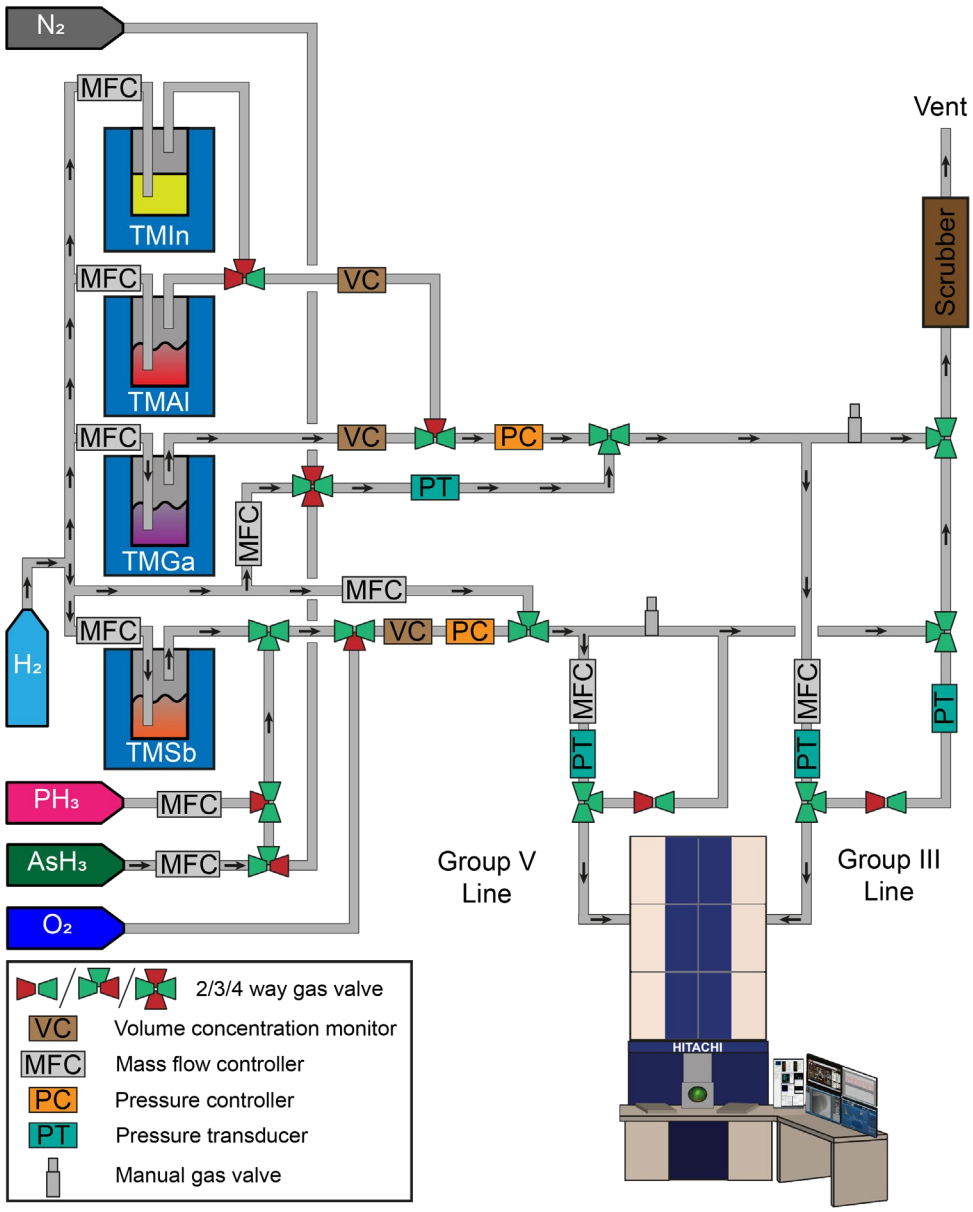

Figure 2.4 Schematic of the gas handling system used in the Lund ETEM.† Note the gas handling system is set up to supply TMGa, TMSb and AsH_3 with additional H_2 dilution on both the group III and group V gas lines to the microscope column with arrows illustrating gas flow in the lines.

† The bubblers of the GHS can be exchanged and the schematic depicts the precursors available during my PhD.

3 Size effects in GaAs nanowire growth

In III-V semiconductor nanowires the lateral dimensions are known to affect nanowire growth rate and crystal phase.[65–69] Furthermore, the nanowire diameter plays an important role in the radial confinement of charge carriers and in the strain relaxation of nanowire heterostructures.[70–73] Since controlling the growth process with atomic precision is becoming increasingly important for modern electronic devices, it is crucial to develop fundamental understanding of how the lateral dimensions of III-V nanowires affect their growth dynamics. Therefore, in **Paper I**, the aim was to provide experimental evidence of how nanowire diameter affects the growth dynamics of Au-seeded GaAs nanowires. However, before we delve into the results of that study we will first examine how we can nucleate GaAs nanowires *in situ*.

3.1 Nucleation of GaAs nanowires

At its most basic, the way to nucleate GaAs nanowires involves heating the MEMS chip with deposited Au nanoparticles on it to 420 °C, then supplying TMGa and AsH_3 to the microscope. More often than not, this exact workflow did indeed result in the nucleation of GaAs nanowires; however, as this is a PhD thesis titled "Opening the black box of III-V nanowire growth" we will examine the nucleation in closer detail.

The *in situ* growth studies discussed in this thesis rely on nanowires grown from Au nanoparticles using the VLS process. Therefore, before we can nucleate GaAs we have to obtain Au nanoparticles on the heating chips. The go to method for obtaining Au nanoparticles has been through gas phase deposition (carried out by Sebastian Lehmann) as it allowed to deposit nanoparticles on multiple chips with good size and density control. For more information on the used method please see the paper by Magnusson et al.[74] In Figure 3.1 (a) a Au nanoparticle is shown residing on the SiN_x membrane of a MEMS chip heated to 420 °C. Since the nanoparticle diameter is about 25 nm the melting point is almost the same as for bulk Au (≈1065 °C) and the

nanoparticle is solid.[75,76] Thereafter, we can start to supply TMGa to the microscope, which will undergo pyrolysis (described in Section 1.2). This will result in free Ga atoms on the surface of the MEMS chip, which can diffuse on the surface and start alloying with the Au nanoparticles. This dramatically lowers the melting temperature until the Au-Ga nanoparticle undergoes a phase change from solid to liquid phase as shown in Figure 3.1 (b).[42] At this point if we add AsH_3 to the microscope, there is a chance to nucleate a GaAs crystal from the nanoparticle (provided sufficient supersaturation is reached as discussed in Section 1.3), which is indicated by the black arrow in Figure 3.1 (c). In the initial stages, after a nanowire is born, the crystallite is often dynamic and mobile (if it does not nucleate in contact with the underlying SiN_x thin film).[26] This is due to the crystallite/nanoparticle system trying to establish a stable growth front along the most energy-efficient pathway, which are the $\langle \bar{1}\bar{1}\bar{1} \rangle$ and $\langle 000\bar{1} \rangle$ type directions for ZB, and WZ, respectively.[2,20,22,24–26] If the precursor supply and temperature are kept constant the nanowire/nanoparticle system eventually stabilizes, transitioning to a steady-state growth regime as shown in Figure 3.1 (d).

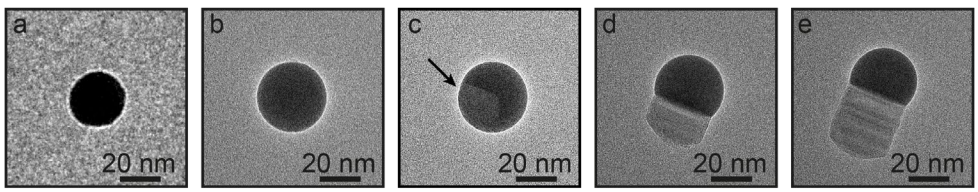

Figure 3.1 HRTEM images showcasing GaAs nanowire nucleation from a Au nanoparticle. (a) Solid Au nanoparticle. (b) Liquid Au-Ga nanoparticle. (c) GaAs crystallite (as indicated by the black arrow) shortly after nucleation from the liquid nanoparticle. (d-e) Nanoparticle, nanowire system once steady-state growth of GaAs is achieved. In all the HRTEM images nanoparticle, nanowire resides on SiN_x thin film.

The described procedure is quite simple; however, several things should be considered to maximize the chance of successful nucleation (meaning a high yield of nanowires nucleated from Au nanoparticles). Firstly, the partial pressure of TMGa has a dramatic effect on the amount of Ga atoms deposited on the surface. If a high enough partial pressure is used this can result in the formation of Ga droplets on the chip surface. In extreme cases, this can lead to no or very few Ga atoms alloying with Au nanoparticles as Ostwald ripening takes place and a high density of large Ga droplets are formed on the chip. Secondly, the sequential supply of precursors is used to minimize the risk of parasitic growth on the chip surface. For nucleation to occur from the nanoparticle, a sufficiently high supersaturation must be reached in the nanoparticle, as discussed in Section 1.3. Depending on the partial pressures used this can take anywhere between a few seconds and several minutes. However, if both TMGa and AsH_3 are supplied to the microscope concurrently, parasitic nucleation of GaAs can happen without the catalyst. A potential explanation for this could be surface roughness, or residues of the support

SiN_x film, which can act as preferential nucleation sites resulting in surface growth. The parasitic growth was most often observed to happen in conjunction with high TMGa partial pressures and resulted in formation of 3D GaAs crystallites.

In these cases, where the nucleation stages did not work out as intended due to suboptimal growth conditions, the grown material can be thermally decomposed to "reset" the chip for a new nucleation attempt. As discussed in Section 1.3.1, nanowire growth using the VLS method is dependent on the difference in chemical potential between all three phases, with the vapour phase having the highest chemical potential and solid phase the lowest one. If, however, this is reversed, the thermodynamic driving force will now favour evaporation of the solid phase through the liquid into the vapour phase. In practical terms, if the precursor supply to the microscope is stopped, while remaining at an elevated substrate temperature, the nanowires will be decomposed by the liquid nanoparticle.[77] Since this process is temperature dependent, higher temperatures will result in faster decomposition rates. At high enough temperatures, combined with low background precursor pressures, this will also result in sublimation of parasitic GaAs crystallites.

3.2 Nanowire diameter and its effect on growth

Now that we have successfully nucleated GaAs nanowires, we can tackle the age-old question: "Does size matter in the growth of GaAs nanowires?". Investigating size effects in nanowire growth has been a topic of interest ever since VLS method was first proposed as a mechanism for growth of 1D semiconductor materials. Here it is worth highlighting the studies by Givargizov as being among the first attempts to give a detailed explanation of how diameter affects growth of 1D semiconductors.[69,78]

Typical investigations into size effects have previously relied on either theoretical modelling of the growth process, and/or post-growth electron microscopy investigations of the nanowires.[65,66,68,79–81] The main drawback of these approaches is the inability to probe the growth dynamics. As demonstrated by previous *in situ* studies of Au-seeded GaAs nanowires, layer-by-layer growth is comprised of two distinct processes, namely, the incubation and step-flow processes (although nomenclature can differ between authors).[19,21] Furthermore, as demonstrated by Maliakkal et al., during *in situ* growth of Au-seeded GaAs nanowires, incubation and step-flow processes are primarily dependent on the TMGa and AsH_3 partial pressures, respectively.[21] Therefore, the primary focus of **Paper I** was to track how the timescales of both of these processes were affected by nanowire diameter, which, in turn, allowed us to determine how the diameter affects the availability of each of the growth species.

The incubation and step-flow processes are demonstrated in Figure 3.2 using schematics coupled with HRTEM images exported from an *in situ* "birds eye" view video of a Au-seeded GaAs nanowire. These videos provide complementary information to the on-axis imaging and video acquisition, since we are able to infer the 3D morphology of the growing layer throughout the step-flow process. This has previously been investigated in a paper by Harmand et al. to which curious readers are referred.[19]

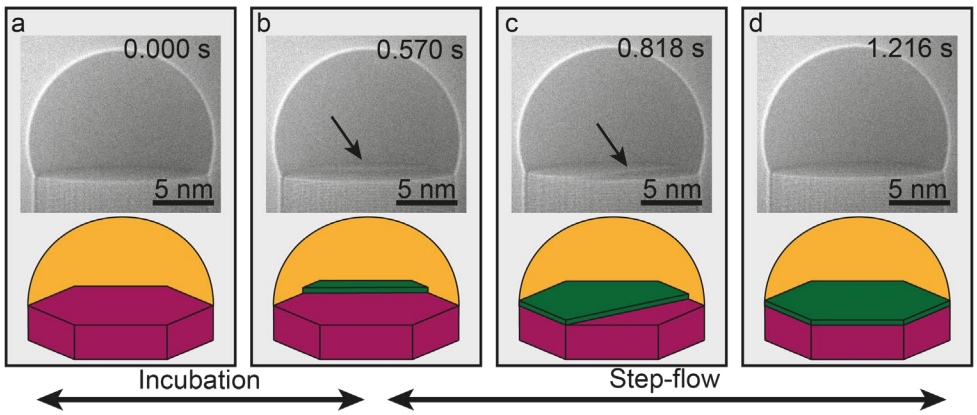

Figure 3.2 Incubation and step-flow process in GaAs nanowires. (a-b) HRTEM images and schematics showing the incubation process. Incubation is concluded and simultaneously the step-flow process is started when a new layer is nucleated indicated by the black arrow (b), and the green island in the schematic. (b-d) HRTEM images and schematics showing the GaAs bilayer step-flow process. The black arrow in (c) indicates the step between the growing layer and the previously flat liquid-solid interface. Timestamp in the images represents time since the last step-flow process was observed to be completed. In the schematics the liquid Au-Ga-As alloy is shown in yellow, solid GaAs crystal in red and the newly nucleated layer in green. Figure adapted from **Paper I**.

Incubation and step-flow processes were described in Section 1.3.2 and are briefly reintroduced again here. The incubation process can be understood as the waiting time required for the nanoparticle to reach sufficient supersaturation to allow nucleation of a new bilayer. This is depicted in Figure 3.2 (a-b) with the black arrow in Figure 3.2 (b) used as a guide to the eye pointing towards the partially completed new layer, which in the schematic is shown in green. The end of the incubation process marks the start of the step-flow process as shown in Figure 3.2 (b-d), with the black arrow marking the position of the growth front of the partially completed layer. The step-flow process describes the time in which a bilayer progresses across the liquid-solid (LS) interface until a flat LS interface is restored. Under steady-state conditions, these processes continuously repeat thus comprising the layer-by-layer growth.

In this study, the diameters of the investigated nanowires were < 30 nm, since size effects, such as the Gibbs-Thomson (GT) effect, are expected to affect the growth

process more strongly at small nanowire diameters. The GT effect for the growth of III-V nanowires introduces an additional term for calculating the effective supersaturation between liquid and solid phase.[78,82] This term is inversely dependent on the nanoparticle radius, and is a consequence of the curvature-dependent vapour pressure i.e. the Kelvin effect discussed more below.[65] The GT correction term essentially lowers the thermodynamic driving force (supersaturation) for layer-by-layer growth. Therefore, from Mårtensson et al.[65] the bulk supersaturation $\Delta\mu_{LS}$ for nanowire growth is replaced by the effective supersaturation $\Delta\mu_{GTE}$ for the GT case.

$$\Delta\mu_{GTE} = \Delta\mu_{LS} - \frac{2\gamma_{LV}(\Omega_S - \Omega_L)\sin\beta}{r} \tag{3.1}$$

Here γ_{LV} is the liquid-vapour (LV) interface surface energy, Ω_S and Ω_L are the volumes of a III-V atomic pair in solid and liquid, respectively, while the nanoparticle contact angle is β, and nanowire radius is r. From Equation (3.1) it then becomes apparent that there is a critical nanowire radius where the supersaturation $\Delta\mu_{GTE} \leq 0$. This means that there is no driving force for nucleation of new layers and nanowire growth stops (see Section 1.3.2 for discussion on layer-by-layer growth). In literature this is described as the Gibbs-Thomson radius.[52]

In order to analyse the incubation and step-flow time as a function of nanowire diameter we acquired high frame rate (50 - 200 FPS) videos of the growth. In Figure 3.3 (a) and (b), HRTEM images of typical nanowires used in this study with diameters of 13 nm and 26 nm, respectively, are shown. The growth conditions of nanowires were chosen such that the 26 nm nanowires grew in a WZ crystal phase, and were kept constant for all the studied nanowires. Regardless of the examined nanowire diameter the crystal phase remained unchanged.

We will start by examining the effect of nanowire diameter on the incubation process time shown in Figure 3.3 (c). Here each of the data points represents a single nanowire with 20 consecutive analysed incubation events, while the error bars describe the standard deviations. It can be observed that the incubation time remains stable within most of the diameter range except for a sharp increase at 11.5 nm diameter. This increase could be interpreted to signify nanowire dimensions approaching the Gibbs-Thomson radius. However, since only a single nanowire was examined at this diameter it is difficult to verify this hypothesis.

It is important to note that throughout all the observed incubation events, when videos were acquired in the "birds eye" view as shown in Figure 3.2, (regardless of the diameter) the newly nucleated islands were always observed to be anchored to the triple

phase line (TPL). Moreover, we always observed the nucleated islands to be attached to at least two of the nanowire facets with no preference for a specific location around the perimeter of the TPL. The stochastic nature of where newly nucleated islands were observed is not a surprise, as the nanowire facets of the same crystallographic family have the same surface energy and nucleation of new islands is predicted to be energetically more efficient at TPL.[19,20] However, we did observe that the preference of the nucleation site could be affected by locally increasing electron dose to the point where all consecutive nucleation events happen on a particular side of the LS interface.

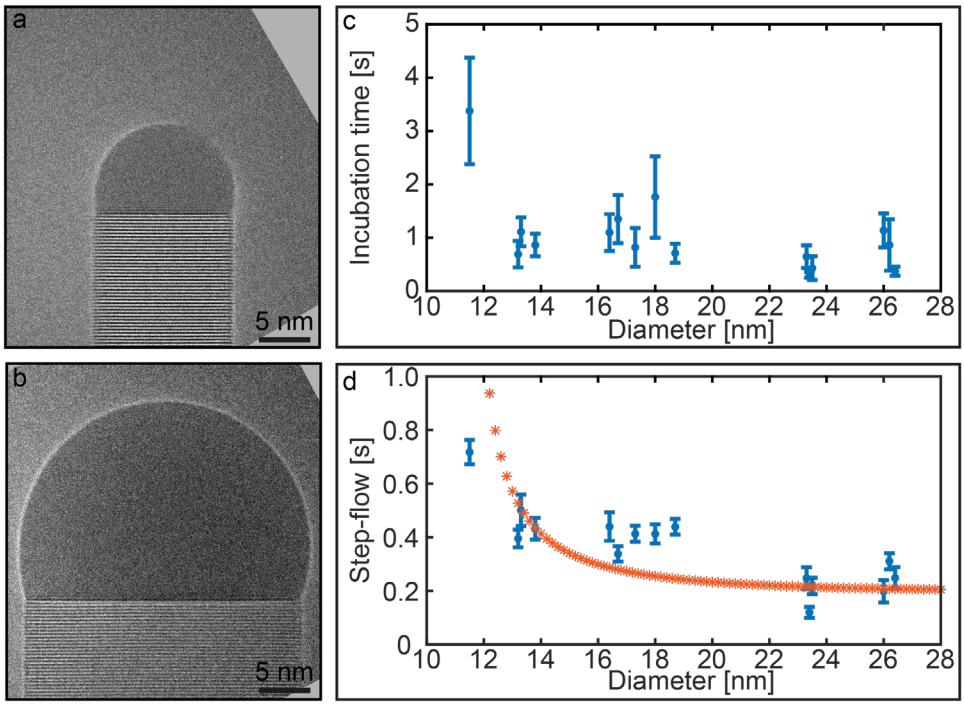

Figure 3.3 Effect of nanowire diameter on incubation and step-flow process time. (a-b) Au-seeded GaAs nanowires growing in a WZ crystal phase with diameter of 13 nm and 26 nm, respectively. (c) Incubation time as a function of GaAs nanowire diameter with error bars representing standard deviations. Each data point corresponds to a nanowire for which 20 events were recorded. (d) Step-flow time as a function of GaAs nanowire diameter with error bars representing standard deviations. Each data point corresponds to a nanowire for which 21 events were recorded. Orange stars depict the modelled step-flow time curve. Figure adapted from **Paper I**.

Now we turn our attention to the step-flow process time as a function of nanowire diameter depicted in Figure 3.3 (d). Similarly to the incubation time, each data point here represents a single nanowire with 21 consecutive step-flow events and error bars depicting the standard deviations. Here we could observe that the step-flow time increased gradually when moving towards smaller nanowire diameters with a similarly

sharp increase at the smallest nanowire diameter, as was observed also for the incubation process time in Figure 3.3 (c). Since the incubation time was stable across the majority of the diameter space within the standard deviation, the focus instead was directed towards developing a model that could aid in understanding the underlying cause behind the increasing step-flow time with reduced nanowire diameter.

As discussed before, the incubation and step-flow processes are dependent primarily on partial pressures of TMGa and AsH_3, respectively.[21] This means that increase in step-flow time is likely related to a decreased abundance of As atoms in the nanoparticle. Since the growth conditions were constant for all the investigated diameters these observations could be caused by an increased As atom desorption from the nanoparticle due to curvature effects (also known as Kelvin effect). To demonstrate this effect a thermodynamic model was devised that is a simplified version of the model used previously in the work of Maliakkal et al.[21] Based on the data in their study they showed that the step-flow time is inversely proportional to the net flux of As atoms across the LV interface:

$$t_{SF} \propto \frac{1}{J_{As,LV}} \tag{3.2}$$

Here t_{SF} is the step-flow time while $J_{As,LV}$ is the effective As atom flux across the LV interface. In order to approximate the step-flow time as a function of vapour pressure, we can expand the effective As flux $J_{As,LV}$ using the Hertz-Knudsen equation:

$$t_{SF} = \frac{A_{LS}\sqrt{2RM_{As}T\pi}}{A_{LV}N_A\left(P_{As,Vapour} - P_{As,Liquid}(r)\right)} \cdot \frac{h}{\Omega_{GaAs}} \tag{3.3}$$

Here A_{LS} and A_{LV} are the LS and LV interface areas, respectively. Height of a GaAs bilayer is h, Ω_{GaAs} is the volume of a GaAs atom pair, $P_{As,Vapour}$ and $P_{As,Liquid}(r)$ is the As pressure in the vapour and liquid phase, respectively. The As vapour phase pressure was set to be constant and calculated assuming no desorption from the nanoparticle occurs. Lastly, R is the ideal gas constant, M_{As} is molar mass of As and T is temperature in Kelvin.

To be able to model the impact of diameter on the vapour pressure we expand the liquid phase As pressure $P_{As,Liquid}(r)$ using the Kelvin equation, which describes the increase of vapour pressure for curved LV interfaces. This transforms the Equation (3.3) into the following expression:

$$t_{SF} = \frac{A_{LS}\sqrt{2RMT\pi}}{A_{LV}N_A\left(P_{As,Vapour} - \eta \exp\left(\frac{2\gamma_{LV}V_L}{rRT}\right)\right)} \cdot \frac{h}{\Omega_{GaAs}} \qquad (3.4)$$

Here γ_{LV} is the LV interface surface energy, V_L is the molar volume of Au from DeHoff,[75] and η is a fitting parameter used to describe the As pressure of a flat liquid surface, which in our model is set to the same value as in the model by Maliakkal et al.[21] The chosen value of γ_{LV} was based on data reported by Tornberg et al. for a fixed nanoparticle contact angle.[83]

The modelled fit is shown in Figure 3.3 (d) using orange stars, and is in good agreement with the experimental data (shown in blue) incorporating the stable region at large nanowire diameter as well as the sharp increase at the smallest diameter. This model demonstrates that increased vapour pressure of the nanoparticle can potentially explain the observed trend in step-flow time. It is possible that a similar trend could also be present in the case of Ga-dependent incubation time, which however is obscured by the large standard deviations. On the other hand, the effect for Ga might be more pronounced at smaller diameters as alluded to by the sharp increase in incubation time at the 11.5 nm diameter nanowire. This could be tested in future experiments by examining the growth of nanowires < 11 nm diameters.

The difference in how nanowire diameter affects step-flow and incubation is likely caused by the elemental differences of As and Ga atoms. Relative to the Ga atoms, the As atoms are more volatile and can desorb from surfaces easily.[84,85] Additionally, As atoms alloy poorly with Au leading to the concentration of As atoms in the nanoparticle being estimated as < 1 at.% during growth.[42] In contrast to As atoms, the Ga atoms alloy readily with Au and are found to have a concentration of 25 – 55 at.% in the nanoparticle.[42] Previous theoretical studies of the growth process have shown that a decrease in As concentration can a have significant effect on the growth process, even supressing nucleation of new layers.[86–88] This could mean that also the observed increase in incubation time for 11.5 nm diameter ultimately is caused by a decrease in the net As flux.

To summarize, the observations made from **Paper I** clearly show how the Ga-dependent incubation process and As-dependent step-flow process are affected by nanowire diameter differently. The As-dependent step-flow process is affected by diameter leading to a significant change in the growth dynamics. However, the Ga-dependent incubation time remained robust across the majority of investigated diameters.

4 Growth of GaSb nanowires

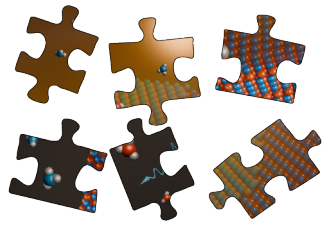

The ETEM offers a unique way to study materials and phenomena that are difficult or even impossible to study with conventional growth and modelling. This makes the ETEM an excellent testbed to research materials such as the III-Sb nanowires, which are often regarded as one of the more challenging subtypes of III-V nanowires to grow.[7,8,89,90] This is largely due to the material properties of elemental Sb. In comparison to the more commonly used group V elements, Sb has a lower vapour pressure, a higher solubility in Au, and is known to behave as a surfactant.[7,8] Consequentially, Sb is also known to contaminate growth reactors – thereby affecting any subsequent growths if thorough cleaning procedures are not used. So you can imagine my surprise and delight that I was actually allowed to study these materials in our precious ETEM!

It is worth noting that **Paper II** and **Paper III** are the first *in situ* growth studies of any of the III-Sb nanowires. Therefore, in these studies my colleagues and I aimed to give a comprehensive and detailed description of Au-seeded GaSb nanowires as a materials system. This chapter is structured to give an overview of the approaches to begin growth of GaSb nanowires *in situ*, followed by a detailed discussion of the nanoparticle composition and morphology during growth. Thereafter, the interplay between nanoparticle and nanowire morphology is discussed, which was the focus of **Paper II**. Lastly, the growth dynamics of GaSb nanowires and how they are affected by the nanoparticle composition is examined, which was the focus of **Paper III**.

Before delving into the chapter contents, I would like to point out the difference in V/III ratio between the original figures from **Paper II,** and the adapted figures in the thesis. Between publishing **Paper II** and **Paper III,** the mass-flow controllers of the gas handling system were recalibrated. The data from **Paper II** was replotted using the new calibration to enable comparison between data from **Paper II** and **Paper III** presented in this chapter.

4.1 Pathways to achieve growth of GaSb nanowires

The complexities of working with antimonides also extend to challenges regarding nucleation and growth of vertical nanowires. As discussed in Section 1.3.1, nucleation and growth of III-V nanowires is often carried out using metal catalyst nanoparticles that provide an energetically preferential nucleation site on a substrate.[6] In the case of III-Sb nanowires this has proven to be a difficult endeavour as instead of the desired vertical growth the metal nanoparticle is "pushed" along the surface of the growth substrate.[7] Consequently, in the majority of studies focused on growth of III-Sb nanowires, such as GaSb or InSb, it is far more common to grow them in an axial nanowire heterostructure using stems consisting of other III-Vs.[7,8,31,89–92] This was also the initial approach used to enable growth of GaSb nanowires *in situ*; however, at later stages of my PhD a method for direct nucleation was realized. In this section, I summarize *in situ* results of both approaches to facilitate growth of GaSb nanowires.

4.1.1 Direct nucleation of GaSb

The procedure of nucleating GaSb nanowires is very similar to that of nucleating GaAs nanowires described in Section 3.1. However, some key differences between these systems have to be taken into account. When probing parameters required for direct nucleation, it became apparent that nucleating GaSb required a significantly higher concentration of Ga in the nanoparticle, relative to nucleation of GaAs. This observation is quite reasonable when examining the results from post-growth XEDS analysis of Au-seeded GaSb nanowires grown *ex situ*. There the estimated concentration of Ga in the nanoparticle during growth exceeds 50 at.% (which as you will see later in this chapter is also observed *in situ*).[7,90] This contrasts with the growth of Au-seeded GaAs nanowires, where recent *in situ* studies have shown that the Ga composition in the nanoparticle during growth is approximately 25 - 55 at.% depending on the growth conditions.[42]

Similarly to nucleation of GaAs described in Section 3.1, here the precursors are also introduced sequentially, meaning that initially only TMGa is supplied to the microscope, while TMSb is supplied later. As the substrate is heated to 420 °C, while TMGa is supplied to the microscope, the precursor is pyrolysed and a Au-Ga alloy forms. This is depicted in Figure 4.1, where HRTEM images of Au nanoparticles are shown with increasing dimensions due to increasing uptake of Ga. The Au nanoparticles are initially solid as shown in Figure 4.1 (a). However, when enough Ga is incorporated into the nanoparticle the melting point is lowered to the point where they turn liquid, as seen in Figure 4.1 (b).[42] From the experimental study into

nucleation it was determined that in order to increase the yield of nucleation, the Ga concentration in the nanoparticle before supplying TMSb should ideally exceed 90 at.%, which is the case for nanoparticles shown in Figure 4.1 (c). To estimate the composition of these nanoparticles XEDS can be used; however, since only TMGa is supplied the volume increase of nanoparticles happens due to Ga accumulation. Therefore, a simple calculation of nanoparticle volume (assuming it is spherical) could be used to give a good estimate of the composition.

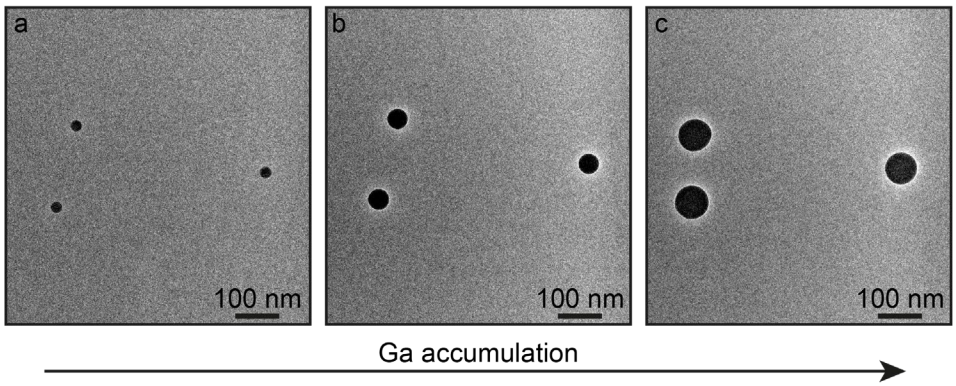

Figure 4.1 Accumulation of Ga in the Au nanoparticle before nucleation. (a) HRTEM image of solid Au nanoparticles before initiating supply of TMGa. (b) HRTEM image of liquid Au-Ga nanoparticles. (c) HRTEM image of the same nanoparticles later in time when the Ga composition in the nanoparticle is estimated to exceed 90 at.%.

When the desired nanoparticle composition is reached, TMSb can be supplied to the microscope and nucleation should occur. However, this procedure often resulted in mixed success with low nucleation yields being a problem, especially when high TMSb flow was used. Although the mechanism of high TMSb flow inhibiting nucleation is not yet fully clear, conventional studies examining the growth of GaAs with GaAsSb inserts have theorized that Sb can lower supersaturation.[30] In practical terms this means that the nucleation probability is decreased resulting in lower yields and poor control of the process.

Therefore, a more reliable nucleation procedure involving a rapid temperature change was devised, utilizing the fact that MEMS chip temperature can be rapidly changed. With this approach the nucleation again starts by saturating Au nanoparticles with Ga until >90 at.% is reached as depicted in Figure 4.2 (a). Thereafter, the TMSb is introduced to the growth chamber, which is immediately followed by lowering the MEMS chip temperature by 100 °C. This results in nucleation of a solid GaSb crystal as shown in Figure 4.2 (b). By lowering the temperature the nanoparticle enters a supersaturated state, thereby increasing the driving force for solidification.

Subsequently, the temperature can be increased to the growth temperature of 420 °C. Occasionally, part of the newly nucleated crystal was observed to be dissolved by the nanoparticle during the increase in temperature. This presumably occurred in order to restore the equilibrium concentration of the nanoparticle; however, it was generally observed that at least a part of the crystal remained as seen in Figure 4.2 (c).

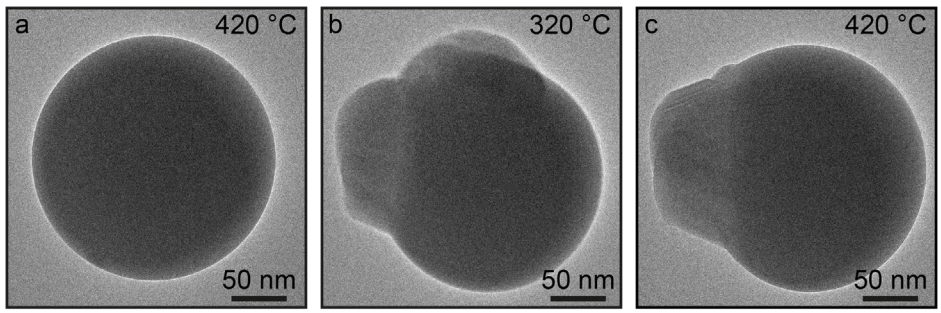

Figure 4.2 HRTEM images depicting direct nucleation of GaSb using rapid temperature shifts. (a) Image of a Au-Ga nanoparticle at 420 °C. (b) Nucleation of GaSb crystal due to lowering temperature by 100 °C. (c) Nanowire/nanoparticle system after reaching growth temperature of 420 °C.

4.1.2 GaAs/GaSb heterostructures

In the heterostructure approach, GaAs nanowires are nucleated and grown for a period of time using methodology described in Section 3.1. Thereafter the growth system is prepared to initiate GaSb growth. The key steps here involved lowering the MEMS chip temperature (to prevent decomposition of the as-grown GaAs stem), stopping the precursor supply to the microscope, and purging the group V line of AsH_3 using the procedure described in Section 2.3. Subsequently, TMGa and TMSb were introduced to the microscope, and the MEMS chip temperature increased to growth temperature. The realization of a GaAs/GaSb axial heterostructure *in situ* is shown in Figure 4.3 (a), where the white arrow is used to indicate when growth was restarted using TMGa and TMSb. The data pertaining to the growth of Au-seeded GaSb nanowires discussed in the remainder of this chapter was obtained from nanowires using the heterostructure approach.

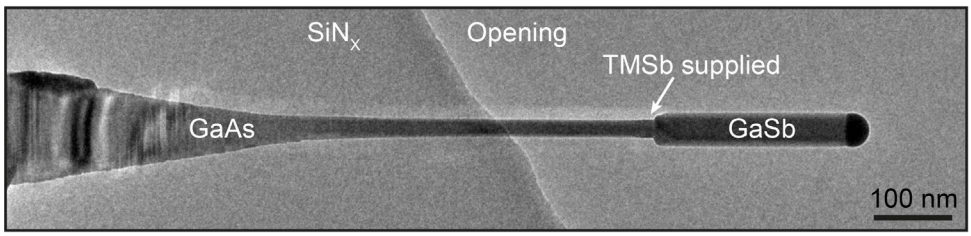

Figure 4.3 GaAs/GaSb nanowire heterostructure.

4.2 Nanoparticle composition and morphology during growth

To develop a comprehensive understanding of the nanowire growth process we will first examine the nanoparticle composition during steady-state growth, as it plays an important role in determining growth dynamics and nanowire morphology.[6,22,42,51] The nanoparticle composition was determined using XEDS by positioning the electron beam (in TEM mode) on the nanoparticle, and collecting X-rays for 120 s during steady-state growth. Therefore, the XEDS results present an average composition of the liquid nanoparticle during steady-state growth of the Au-seeded GaSb nanowires.

In Figure 4.4 (a), the nanoparticle composition is demonstrated as a function of V/III ratio. The limits of V/III ratio represent the boundaries of our established growth window. Lowering the V/III ratio beyond the represented range resulted in nanowires changing growth direction/kinking, whereas higher V/III ratios lead to a stop in axial nanowire growth. As can be seen from Figure 4.4 (a), the compositional data is shown using two data series (marked by striped and filled shapes). Since the V/III ratio often hides the impact of a particular precursor on the nanowire growth, the V/III ratio was altered by changing either the TMGa or the TMSb supply to the microscope, while keeping the other precursor influx constant. Here, and in **Paper II** and **Paper III**, these are referred to as TMGa and TMSb series and depicted with striped and filled shapes, respectively, in Figure 4.4 (a).

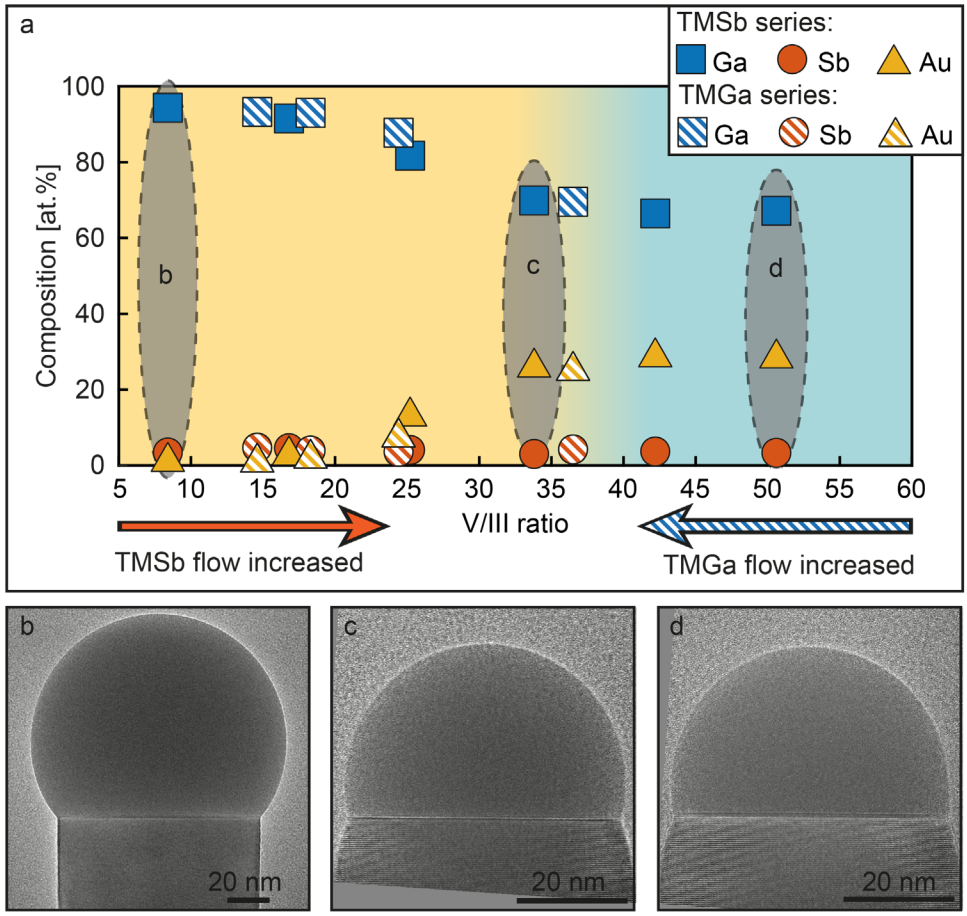

Figure 4.4 Nanoparticle composition and morphology. (a) Composition of the nanoparticle during GaSb nanowire growth as a function of V/III ratio measured by XEDS. The TMSb and TMGa series are depicted with filled and striped shapes respectively, while the yellow and cyan shaded regions mark the dynamic and stable regimes, respectively. (b-d) HRTEM images of nanowires at low (b), medium (c) and high (d) V/III ratio, as indicated by grey shaded areas in (a). Figure adapted from **Paper II**.

If we take a look at the data depicted in Figure 4.4 (a) we can notice several interesting things. Firstly, the measured Ga composition is in the range of 66 – 94 at.%, with the highest concentration measured at the lowest V/III ratio. Moreover, the Sb concentration is measurable at 3 – 4 at.% throughout the investigated V/III ratio range. Furthermore, the compositional data, depending on the V/III ratio, seemingly exists in two distinct groups. When the nanowires are grown at high V/III ratios (> 35) the nanoparticle composition remains virtually unchanged. Conversely, at low V/III ratios (≤ 35) there is a strong correlation between V/III ratio and nanoparticle composition.

These distinct regimes are represented in Figure 4.4 (a) by cyan and yellow shaded regions and here, as well as **Paper II** and **Paper III,** are referred to as stable and dynamic regimes, respectively. It is worth noting that the data for the TMSb and the TMGa series follow the same trend. Based on the observations of nanoparticle composition, it is clear that the TMSb series offers a slightly larger accessible growth window, and that the same nanoparticle composition can be attained by adjusting either precursor flow.

At this point it is worth considering what happens to the nanoparticle morphology during all of this. In Figure 4.4 (b-d), a series of images of Au-seeded GaSb nanowires during growth at different V/III ratios is shown. As can be clearly observed, the change in nanoparticle composition has a significant effect on the nanoparticle volume. To quantify this impact, we can assume the nanoparticle is a hemisphere and calculate the nanoparticle volume by fitting a circle to the nanoparticle circumference in HRTEM images. This method has been used previously by Tornberg et al.[83] and is schematically depicted in Figure 4.5 (a). The volume could then be calculated using the following equation:

$$V = \frac{4 \cdot \pi \cdot r^3}{3} - \frac{\pi \cdot h^2 \cdot (3r - h)}{3} \tag{4.1}$$

Here the first term is used to calculate volume of a sphere with radius, r, while the second term is the spherical cap that reaches into the nanowire at a height, h, allowing to calculate nanoparticle volume, V. The calculated nanoparticle volume as a function of V/III ratio is depicted in Figure 4.5 (b). Here we can see that nanoparticle volume is stable for high V/III ratios (> 35), but rapidly increases for low V/III ratios (≤ 35). This trend was observed for both the TMSb and TMGa series, with the only observable difference being a marginally larger increase in volume (when moving to lower V/III ratios) for the TMGa series in comparison to TMSb series. By comparing the trend in nanoparticle composition shown in Figure 4.4 (a) to the one observed here for nanoparticle volume, we can clearly see that the change in nanoparticle composition strongly affects its morphology.

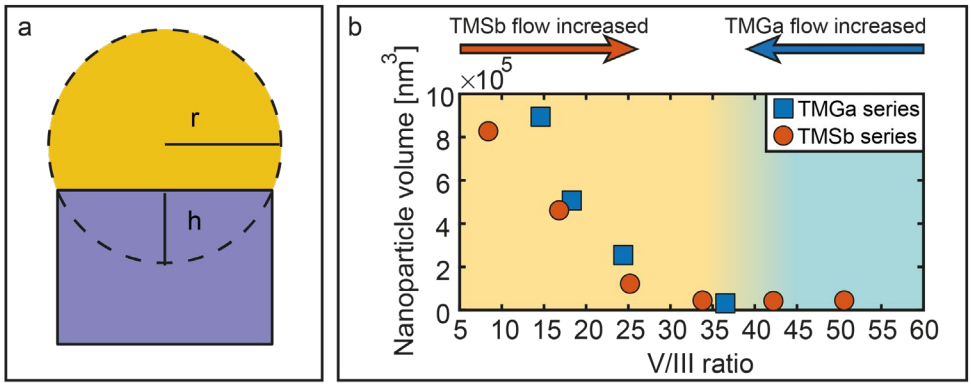

Figure 4.5 Nanoparticle volume and its dependence on V/III ratio. (a) Schematic of measurements needed to calculate nanoparticle volume. (b) Nanoparticle volume as a function of V/III ratio. The TMSb and TMGa series are depicted by blue and orange shapes respectively, while the yellow and cyan shaded regions mark the dynamic and stable regimes, respectively. Figure adapted from **Paper II**.

The dramatic change in nanoparticle volume is not represented when the composition is expressed in at.%. Therefore, by using the calculated nanoparticle volume, shown in Figure 4.5 (b), and utilizing XEDS data from Figure 4.4 (a), we can express the nanoparticle composition in number of atoms through the following equation:

$$N_x = \frac{N_A \cdot c_x \cdot V \cdot \rho_{avg}}{M_{avg}} \tag{4.2}$$

Here, N_x is the number of atoms for a specific element with a measured concentration of c_x, N_A is the Avogadro number, V represents the nanoparticle volume, ρ_{avg} is the average density and M_{avg} is the average molar mass based on the nanoparticle composition.

The composition expressed as number of atoms plotted as a function of V/III ratio is shown in Figure 4.6. The calculated number of atoms depicted in Figure 4.6 was normalized with respect to number of Au atoms in the nanoparticle. Since the number of Au atoms in the nanoparticle is not expected to change, this allows to better visualize change in number of Ga and Sb atoms. When comparing the compositional data represented as at.% in Figure 4.4 (a) and recalculated as number of atoms in Figure 4.6, we can see that the latter provides significantly more information about the true change in composition. Similarly, we can clearly see that the dynamic and stable regimes are still represented as before (depicted with yellow and cyan background). Additionally, we can observe the previously discussed increase in Ga content in the

nanoparticle when moving from high to low V/III ratio. However, the major advantage of representing composition as number of atoms can be seen when examining the Sb content. In Figure 4.4 (a) the Sb content seemingly is constant at 3-4 at.%; however, as the number of atoms includes information on nanoparticle volume, now we can clearly see that in addition to number of Ga atoms increasing towards low V/III ratio so does the number of Sb atoms.

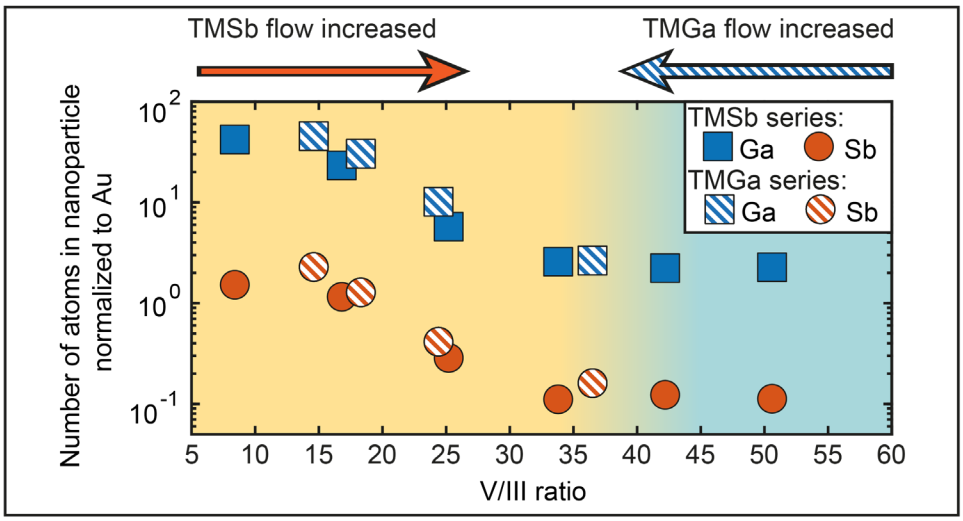

Figure 4.6 Nanoparticle composition represented in number of atoms normalized to Au signal as a function of V/III ratio. The TMSb and TMGa series are depicted with filled and striped shapes respectively, while the yellow and cyan shaded regions mark the dynamic and stable regimes, respectively. Figure adapted from **Paper III**.

4.3 Nanowire morphology

In the previous section, we examined how the vapour phase composition affects nanoparticle composition and morphology. Here we will continue on the road to establishing a comprehensive understanding of Au-seeded GaSb nanowire growth by examining how the nanoparticle affects the nanowire morphology.

In Figure 4.7 (a), nanowire diameter is plotted as a function of V/III ratio with the key observation being that lower V/III ratio leads to a dramatic increase in nanowire diameter. This means that we can effectively tune the nanowire diameter in the range of 50 to 100 nm by using Au nanoparticles with nominal diameter of 30 nm. Additionally, it is worth noting that the nanowire diameter is set during stages of axial

growth, with radial overgrowth being observed only at the highest investigated V/III ratio. This means that the nanowire diameter is predominantly affected by nanoparticle volume, which in turn is affected by its composition ultimately set by the V/III ratio as discussed in the previous section. Furthermore, when growth conditions are changed during the growth process of a nanowire, segments grown at different V/III ratios retain their morphology forming diameter modulated nanowires as depicted in Figure 4.7 (b). The white dashed outline marks the original GaAs nanowire stem that was overgrown with Sb rich solid when V/III ratio of > 35 was used.

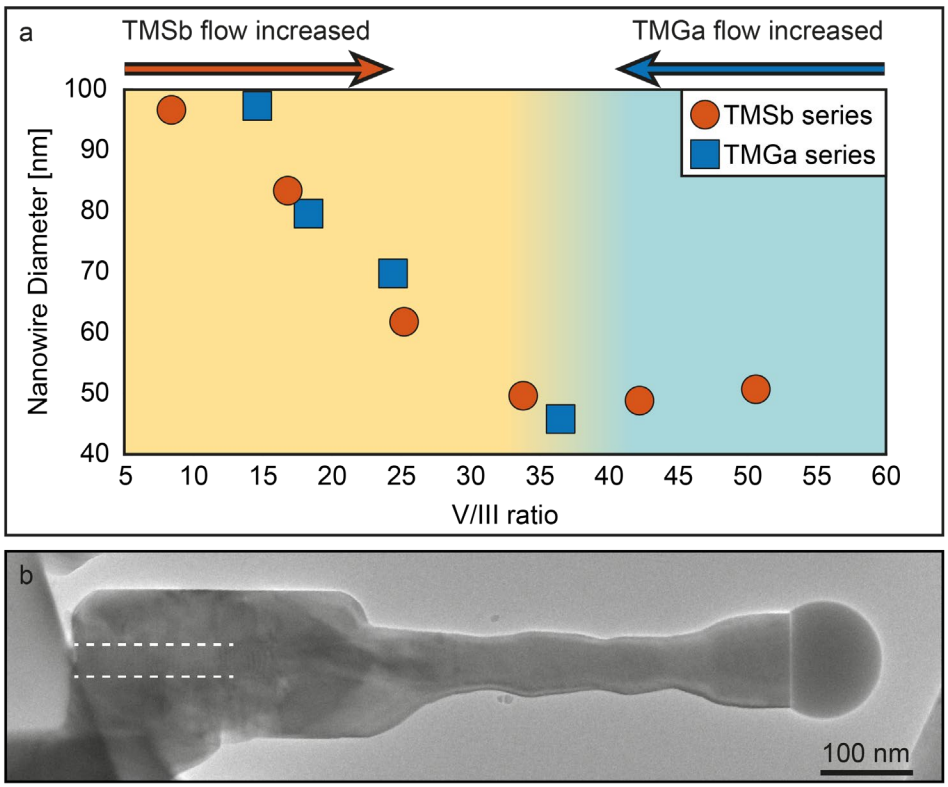

Figure 4.7 Change in nanowire diameter. (a) Nanowire diameter as a function of V/III ratio. The TMSb and TMGa series are depicted by blue and orange shapes respectively, while the yellow and cyan shaded regions mark the dynamic and stable regimes, respectively. (b) Resulting nanowire after recording the TMSb series. The white dashed line marks the original GaAs stem. Figure adapted from **Paper II**.

Controlling nanowire morphology and specifically diameter is a basic prerequisite for any nanowire-based device. Since the *in situ* studies often involve growth conditions that differ from conventional systems, a natural question to consider is how transferable the *in situ* knowledge is to conventional growth systems. In order to investigate this,

complementary *ex situ* growths of Au-seeded GaSb nanowires were conducted in a conventional MOCVD system at different V/III ratios, shown in Figure 4.8 (a). Similarly to the *in situ* growths these experiments were carried out using 30 nm Au nanoparticles as the catalyst, with GaSb nanowire growth achieved via the GaAs/GaSb axial heterostructure approach. Moreover, the growth conditions were chosen such that the GaSb diameter at reference conditions (V/III ratio of 2.0) matched the smallest diameter nanowires obtained from our *in situ* growth study (V/III ratio of 33.8 – 36.5). For the *ex situ* growths the change in V/III ratio was achieved by changing TMSb partial pressure.

The measured diameter as a function of V/III ratio for the GaSb nanowires grown using a conventional MOCVD system is shown in Figure 4.8 (b). Here we can observe that at high V/III ratios the nanowire diameter remains quite stable, whereas below V/III ratio of 2.0, it starts to gradually increase. Due to technical limitations further decrease of V/III ratio by lowering TMSb flow was not possible. However, the observed diameter increase is expected to continue similarly to that observed *in situ*. These results demonstrate that *in situ* studies can be effectively used to gain additional insights regarding growth and are transferrable to conventional growth systems.

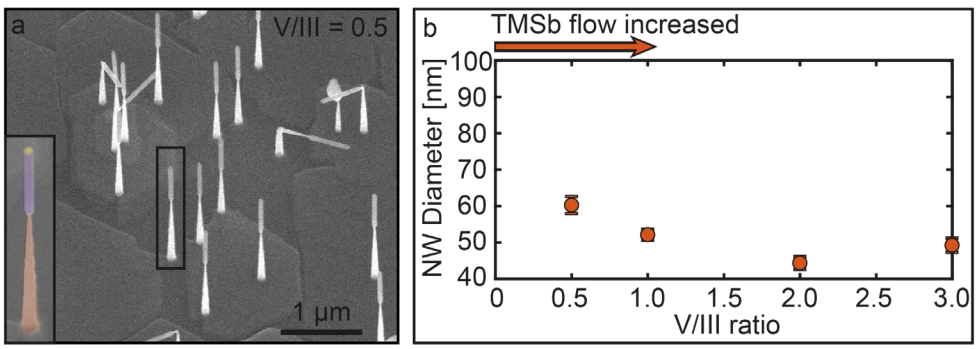

Figure 4.8 Morphology of nanowires grown in a conventional MOCVD setup. (a) 30° tilted view SEM image of Au-seeded GaAs/GaSb nanowires growth at V/III ratio of 0.5. The inset in (a) is a magnified, false-coloured nanowire where GaAs segment is indicated in brown, GaSb in purple and the Au nanoparticle in yellow. (b) GaSb segment diameter as a function of V/III ratio. Figure adapted from **Paper II**.

4.4 Growth dynamics

To continue our deep dive into developing an extensive understanding of Au-seeded GaSb nanowire growth, we will now consider the growth dynamics of these nanowires as discussed in **Paper III**. The analysis here is based on decoupling the growth into

incubation and step-flow processes, which describe the time it takes to nucleate a new bilayer, and for it to cover the liquid-solid (LS) interface. For a more detailed description of these processes see Section 1.3.2 and/or Section 3.2. To establish an understanding of the growth dynamics in Au-seeded GaSb nanowires, 4-10 consecutive events for step-flow and incubation were tracked across a wide range of growth conditions. These results are summarized in Figure 4.9. As before, the V/III ratio was altered by changing either the TMGa or TMSb supply to the microscope while keeping the other precursor influx constant. In the text here, and in **Paper II** and **Paper III,** these are referred to as TMGa and TMSb series and depicted with blue squares and orange circles in Figure 4.9, respectively.

We will start our investigation by examining the incubation time plotted as a function of V/III ratio for TMGa and TMSb series shown in Figure 4.9 (a). We can see that the incubation time remains consistent between 1-10 s across majority of the investigated V/III ratio range, with significant increases observed at the lowest and highest V/III ratios. The increase in incubation time at the lowest V/III ratio can be simply interpreted as a lack of Sb to facilitate new nucleation events (as the TMSb supply here is at its lowest). At the highest V/III ratio, however, the increase in incubation time could be attributed to the radial overgrowth of the nanowires discussed in Section 4.3 (see Figure 4.7 (b)). Overgrowth of the nanowire stem can essentially be interpreted as a material sink, meaning that only a fraction of material is reaching the nanoparticle. Furthermore, in conjunction with the increase in incubation time, we also observed an increase in standard deviation of the incubation process time (as shown by the error bars), which can be attributed to the stochastic nature of the nucleation process.[19,21]

If we now turn our attention to the step-flow process shown in Figure 4.9 (b) we can see a more complex trend than that observed for the incubation process time. At low V/III ratios (< 35), the step-flow process frequently appeared to be instant resulting in average step-flow times of (or near) 0 s. The instant step-flow process time here should be interpreted as occurring faster than the frame rate of the *in situ* camera (20 - 100 FPS) used to acquire videos of the growth. If we continue moving to higher V/III ratio, we can observe a sudden increase in step-flow time reaching about 1.5 s, followed by a subsequent gradual decrease. This decrease in step-flow time with increasing V/III ratio follows an intuitively simple explanation, namely, that a more TMSb-rich vapour phase results in a faster step-flow process. Although this does not directly influence the nanoparticle composition (as shown in Figure 4.6), the vapour composition can have an effect on the exchange rate of Sb atoms across the liquid-vapour (LV) interface during growth. This means that the refill rate of the nanoparticle is increased with increasing TMSb supply (and by extension V/III ratio), which results in faster step-flow time. This dependence is similar to the growth dynamics studied for *in situ* grown

Au-seeded GaAs nanowires, where higher partial pressure of AsH_3 led to faster step-flow time.[21]

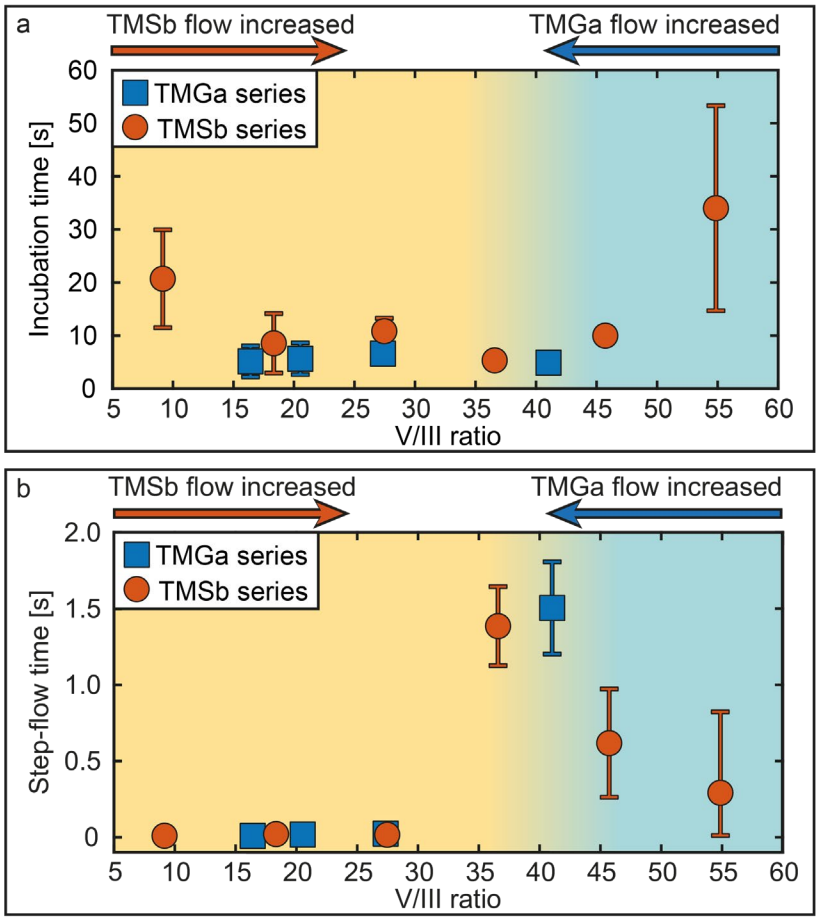

Figure 4.9 Growth dynamics of Au-seeded GaSb nanowires. (a) Incubation time plotted as a function of V/III ratio for the two precursor series, presented as an average with standard deviations. (b) Step-flow time plotted as a function of V/III ratio for both precursor series, presented as an average with standard deviations. The TMSb and TMGa series are depicted by blue and orange shapes respectively, while the yellow and cyan shaded regions mark the dynamic and stable regimes, respectively. Error bars in graphs (a-b) represent standard deviation. Figure adapted from **Paper III**.

However, to explain the complex trend across the whole investigated growth window observed for step-flow in Figure 4.9 (b), we once again must examine the nanoparticle composition. As can be seen, the instant and measurable step-flow time regimes coincide well with the dynamic and stable composition regimes for the nanoparticle, introduced in the previous section and depicted here using the same colour coding of yellow and cyan background, respectively. This alludes to the fact that the step-flow

process is dependent on nanoparticle composition. To make this connection clearer we will now examine the composition as a ratio of number of atoms in the liquid nanoparticle, and number of atoms required to form a single solid bilayer.

Figure 4.10 (a) shows a schematic of a nanowire, where a finite number of Sb atoms comprises a bilayer of GaSb, marked Sb_S, in addition to a number of Sb atoms being dissolved in the liquid nanoparticle, marked Sb_L. To determine how many Sb atoms comprise a single bilayer at a given nanowire diameter, we assume that the nanowire cross-section is a regular hexagon. Furthermore, by dividing this area with the unit cell area of a (111) plane, we can calculate the number of Sb atoms in a single bilayer using the following equation:

$$N_{Sb_S} = \frac{\frac{3d^2\sqrt{3}}{8}}{\frac{a^2\sqrt{3}}{4}} = 1.5\left(\frac{d}{a}\right)^2 \tag{4.3}$$

Here N_{Sb_S} is the number of Sb atoms in one bilayer, d, represents nanowire diameter, while, a, is the lattice spacing for ZB GaSb.[93] Lastly, to obtain a ratio between Sb atoms in the nanoparticle and solid bilayer we can use the number of Sb atoms in the liquid from Figure 4.6.

In Figure 4.10 (b) the ratio between Sb atoms in a liquid nanoparticle and solid bilayer is plotted as a function of V/III ratio. Here we can see that the number of Sb atoms in the liquid phase always surpasses the number of Sb atoms required to form a single bilayer by at least a factor of seven. At V/III ratio > 35 (cyan background), we can observe that the ratio of Sb atoms is quite stable at 7 - 10. This is of course due to the nanoparticle composition (see Figure 4.6), and nanowire diameter (see Figure 4.7) being stable in this regime. However, if we examine the region of the graph with V/III ratio < 35 (yellow background), a dramatic increase in ratio of Sb atoms is apparent with lower V/III ratio. Once again, the trend for both the TMGa and TMSb series is similar, with the TMSb series seemingly plateauing at the lowest measured V/III ratios and the TMGa series data exhibiting a higher ratio of Sb atoms at the lowest measured V/III ratio.

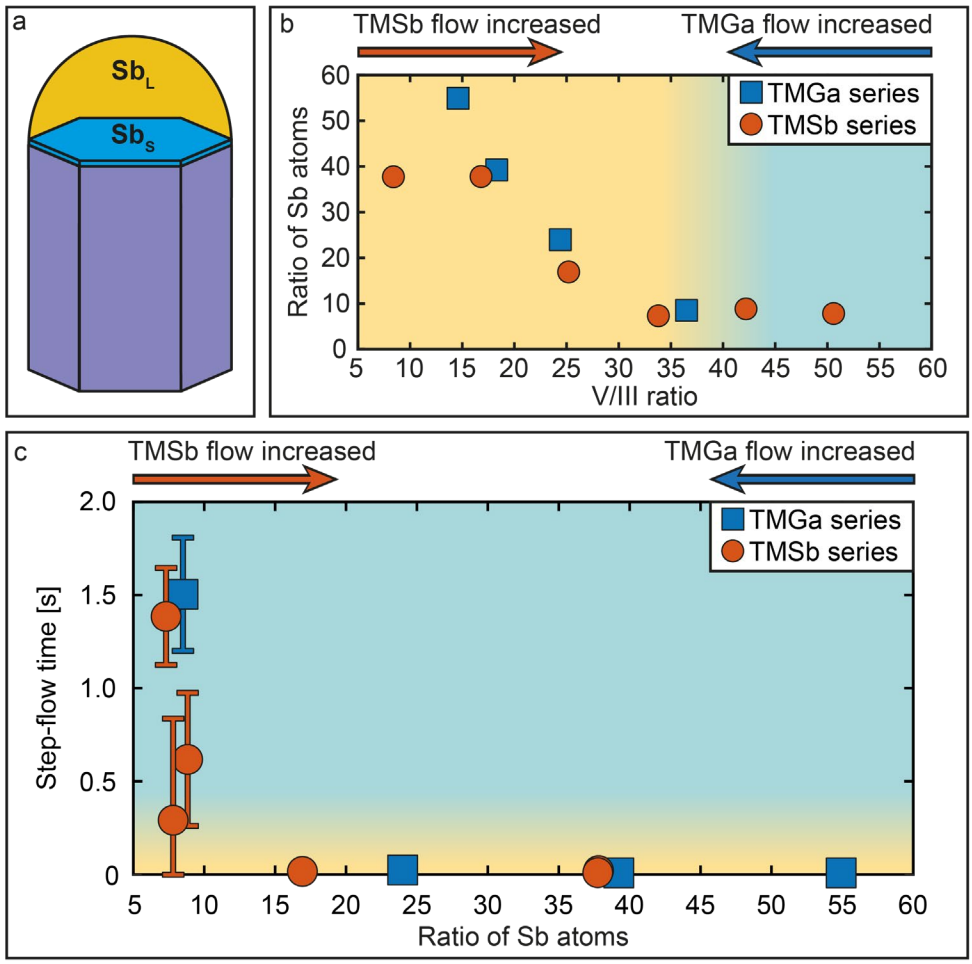

Figure 4.10 Ratio of Sb atoms and its impact on step-flow. (a) Schematic of the nanowire showing Sb atoms in liquid and layer at the LS interface marked Sb_L and Sb_S. (b) Ratio of Sb atoms between liquid and solid phases as a function of V/III ratio. (c) Step-flow time plotted as a function of Sb atom ratio. The TMSb and TMGa series are depicted by blue and orange shapes respectively, while the yellow and cyan shaded regions mark the dynamic and stable regimes, respectively. Figure adapted from **Paper III**.

Now finally the time has come to relate the ratio of Sb atoms shown in Figure 4.10 (b) to the step-flow time depicted in Figure 4.9 (b). In Figure 4.10 (c) the step-flow time is plotted as a function of the ratio of Sb atoms. Note that since this graph is not plotted as a function of V/III ratio, but as a function ratio of Sb atoms, the lower part of the graph (yellow background) refers to the dynamic composition = instant step-flow regime, whereas the top part (cyan background) refers to the stable composition = measurable step-flow regime. From this graph it is evident that when the ratio of Sb

atoms is relatively low (< 10), the step-flow time is measurable, i.e. takes more than a single frame of the *in situ* video. This means that the number of Sb atoms in the liquid nanoparticle above the steady-state level is insufficient to complete a full bilayer instantly. Therefore, after nucleation only a partial layer can be formed, with further growth enabled after more Sb atoms are added from the vapour phase. This results in the step-flow time becoming proportional to the arrival rate, and by extent, the TMSb flow (and V/III ratio). On the other hand, when the ratio of Sb atoms is high (> 10) the step-flow process time appears to be instant. This means that if the nanoparticle contains more than ten-times the number of Sb atoms required for a single bilayer, the step-flow process can conclude without the nanoparticle entering a depleted state and needing to rely on the material supply from the vapour phase, once nucleation happens. Therefore, the step-flow process across the whole investigated parameter space is primarily dependent on the Sb.

Since the incubation and step-flow processes are generally inaccessible for most conventional growth studies, we also investigated changes in growth rate as a function of V/III ratio for these nanowires as shown in Figure 4.11. Since the timescale of the step-flow process is, for the most part, several times shorter than the timescale of incubation the latter has a larger impact on the nanowire growth rate. Similarly to the incubation time plot from Figure 4.9 (a), we can observe the same symmetric trend here with growth rate decreasing at the lowest and highest V/III ratios, while remaining relatively stable for intermediate V/III ratio. It is worth noting that the calculated growth rate for our nanowires mimics what has been previously reported in conventional growth studies of similar temperatures.[7,90] This further supports the fact that *in situ* growth studies can be used to explain trends observed in conventional growth studies. Furthermore, the *in situ* studies offer significantly more insights as the trend in growth rate originates from fundamentally different processes that are only apparent when examining the growth *in situ*.

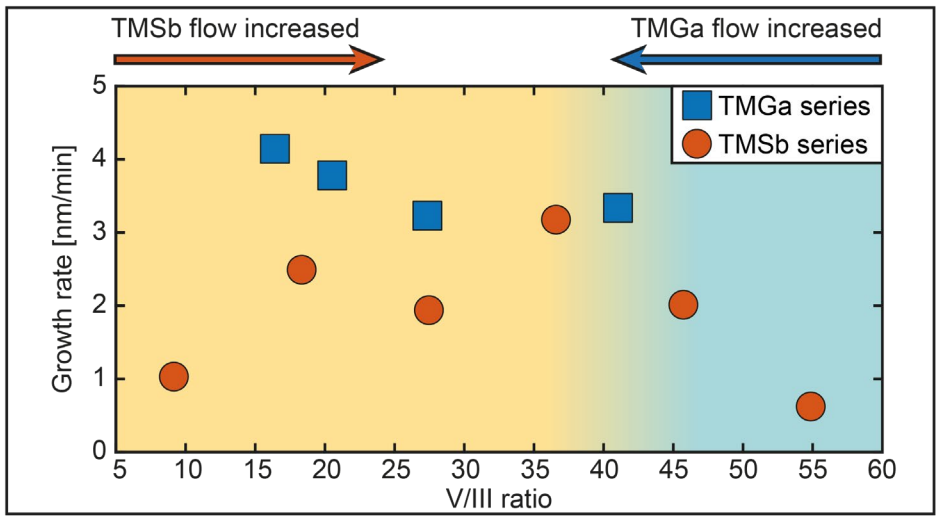

Figure 4.11 Growth rate plotted as a function of V/III ratio. The TMSb and TMGa series are depicted by blue and orange shapes respectively, while the yellow and cyan shaded regions mark the dynamic and stable regimes, respectively. Figure adapted from **Paper III**.

4.4.1 Modelling of the growth process

To provide additional insights into the growth dynamics and look beyond the temporal resolution of the *in situ* videos, Monte Carlo simulations of the growth process were carried out. The simulations are based on a model previously used in the study by Maliakkal et al. [21], which was adapted for GaSb by Robin Sjökvist in **Paper III**. A detailed description of the model can be found in the supporting information of **Paper III**; therefore, here I will only give a brief description of the key model components.

In short, the model simulates mass transport of atomic species through the liquid nanoparticle evaluated at time steps of 1 ms. The number of available atomic species for growth is determined based on the supplied material, direct impingement to and evaporation from the nanoparticle, with impingement and evaporation being surface area dependent. This dependency is schematically shown in Figure 4.12 (a) for the low V/III ratio = large particle volume, and high V/III ratio = small particle volume. The arrows in Figure 4.12 (a) are used to signify the relative impact that the three allowed material pathways in the model, namely, evaporation (E), condensation (C) and solidification (S), have on the material transport in and out of the liquid nanoparticle.

To replicate the experimental observations we used several experimental parameters as model inputs: Firstly, the number of Au atoms in the nanoparticle was set using the

calculated number of Au atoms for the smallest nanoparticle volume from data in Section 4.2. This was done because the smallest nanoparticle has the lowest relative error in number of Au atoms based on XEDS measurements. Secondly, we used the experimentally measured concentrations of Ga and Sb for different V/III ratios from Section 4.2, which, together with the number of Au atoms, determined the nanoparticle volume. Before starting the simulation, this volume was compared to the calculated nanoparticle volume during experiments and the Ga and Sb concentrations were adjusted (by < 2 at.%) to make the volumes comparable. Lastly, the volume was used as a control parameter to determine whether steady-state growth occurs by checking if the nanoparticle shrinks or starts swelling by a significant amount in over 300 s of simulated growth time.

The modelled incubation and step-flow process times are shown in Figure 4.12 (b) and (c), respectively. The error bars here represent standard deviations in both processes from the events occurring during a simulated 300 s of steady-state growth. Similarly to the experimental data, the Monte-Carlo simulation of growth was also performed as a function of V/III ratio, which was altered by changing either the TMGa or TMSb supply while keeping the other precursor pressure constant. These are referred to as TMGa and TMSb series and depicted with blue squares and orange circles in Figure 4.12, respectively. If we start by examining the incubation time depicted in Figure 4.12 (b), and more specifically data for the TMGa series, it is evident that the modelled data matches well with the experimental results shown in Figure 4.9 (a). The same observation can be made for majority of modelled data in TMSb series, except for the high V/III ratio case. For the experimental data depicted in Figure 4.9 (a), an increase in incubation time was observed, which is absent from the modelled data in Figure 4.12 (b). This discrepancy could be explained by the observed increase in radial overgrowth of the nanowires at high V/III ratios discussed in Section 4.3 (shown in Figure 4.7 (b)). As the radial overgrowth is not included as a material pathway into the model, this could explain the differences between experimental and modelled incubation data for the high V/III ratio.

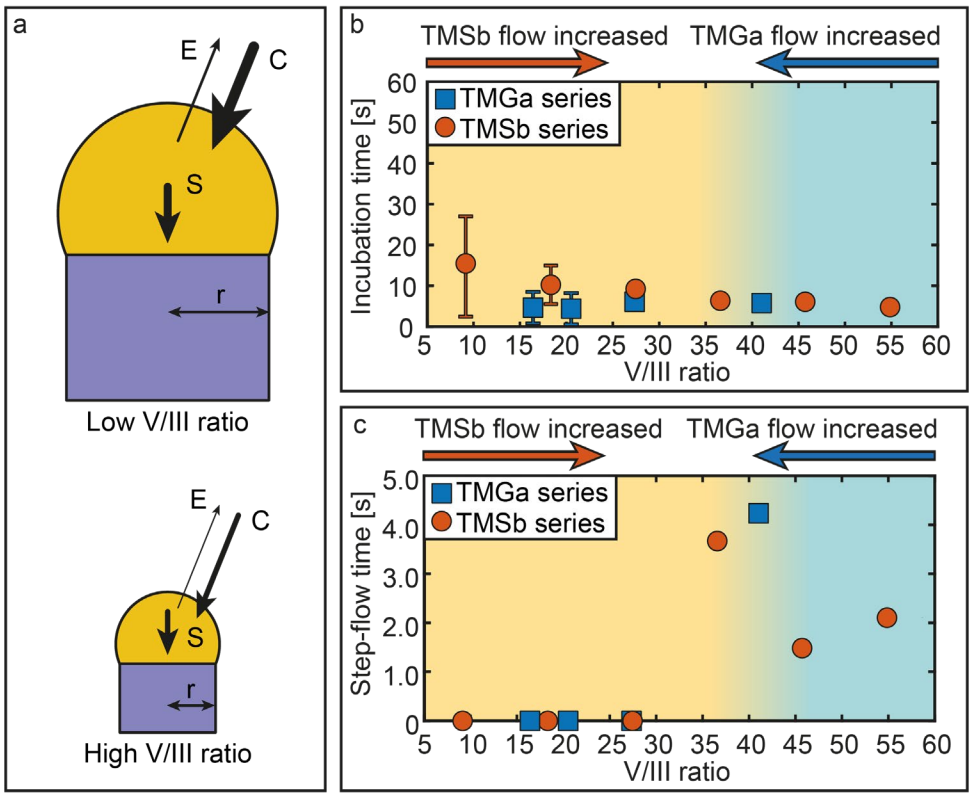

Figure 4.12 Simulated nanowire growth and its atomistic pathways. (a) Atomistic pathways of the nanowire growth simulation for large (low V/III ratio) and small (high V/III ratio) nanowire diameters, nanoparticle volumes. (b) Simulated incubation process time as a function of V/III ratio. (c) Simulated step-flow time as a function of V/III ratio. The TMSb and TMGa series are depicted blue and orange shapes respectively, while the yellow and cyan shaded regions mark the dynamic and stable regimes, respectively, based on the experimental data. Figure adapted from **Paper III**.

Similarly to the modelled incubation time the modelled step-flow time, shown in Figure 4.12 (c), also exhibits a good match to the experimental data shown in Figure 4.9 (b). The model is able to accurately replicate the experimentally observed trends with the instant step-flow present at low V/III ratios (yellow background in Figure 4.12 (c)), followed by a spike in step-flow time for intermediate V/III ratio, and a gradual decrease at high V/III ratios (yellow background in Figure 4.12 (c)).

As we have seen, Monte Carlo simulation of the growth process is able to accurately replicate even non-trivial trends of the layer-by-layer growth process. Additionally, the simulation framework can be used to extract new information about the growth process and even move beyond the limits of temporal resolution imposed by experimental tools. This is because we can determine the liquid nanoparticle composition and

supersaturation with sub-second temporal resolution. In Figure 4.13 the number of Ga and Sb atoms in the liquid nanoparticle during steady-state growth for different V/III ratios is shown in left column (panels a,c,e,g), while complimentary data on supersaturation for the same V/III ratios is shown in the right column (panels b,d,f,h). Here the supersaturation is calculated as the difference in chemical potential between liquid Ga and Sb, and solid GaSb.

We will start the discussion by first examining the results from the highest investigated V/III ratio 54.9 (stable volume, composition regime) for variation in number of atoms as a function of time in Figure 4.13 (a). Here the typical saw tooth profile of layer-by-layer growth with intermittent flat regions can be seen (discussed also in Section 1.3.2). The rise in the curves indicates a build-up of the number of atoms found in the liquid nanoparticle, which occurs during the incubation process. The build-up of material increases the supersaturation depicted in Figure 4.13 (b), and once sufficient supersaturation is reached a nucleation event occurs. This results in a sharp decrease in number of atoms and supersaturation. After nucleation the nanoparticle enters a depleted state (as indicated by the flat regions of the curves), meaning that material incorporated from the vapour into nanoparticle is used for the growing layer. A similar behaviour can also be observed when the V/III ratio is decreased to 36.6, moving to the edge between dynamic and stable regime, for the number of atoms and supersaturation depicted in Figure 4.13 (c) and (d), respectively.

When the V/III ratio is reduced even further to 27.5 we enter the dynamic regime of nanowire growth, and can observe some changes from the higher V/III ratios. Here for the number of atoms and supersaturation, shown in Figure 4.13 (e) and (f), respectively, the saw tooth profile is present. However, the flat regions within the saw tooth profile present for higher V/III ratios are now absent. This suggests that there is a sufficient amount of material dissolved in the nanoparticle to complete the step-flow process once nucleation occurs, without entering a depleted state (which experimentally was observed as instant step-flow).

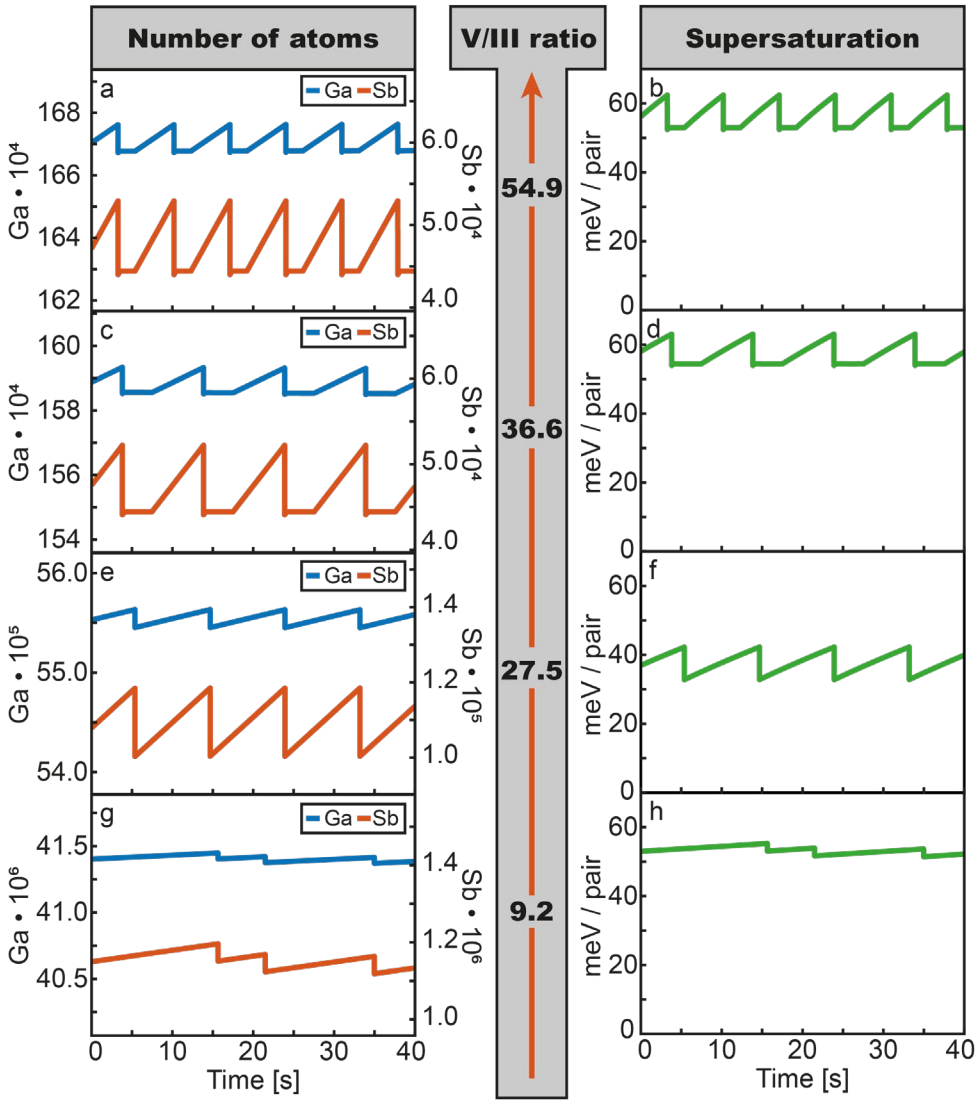

Figure 4.13 Modelled number of atoms and supersaturation of GaSb nanowire growth at different V/III ratios as a function of time. (a,c,e,g) depict the change in number of Ga and Sb atoms for V/III ratios of 54.9, 36.6, 27.5 and 9.2 (shown in bold on grey background in the figure center), respectively. (b,d,f,h) depict the supersaturations for the same V/III ratios. Note the difference in scale for the plots showing the number of atoms across different V/III ratios.

For the lowest modelled V/III ratio of 9.2, the periodicity that was seen for the higher V/III ratios both in the number of atoms Figure 4.13 (g) and supersaturation Figure 4.13 (h) is now absent. Here several nucleation events in close succession and with short incubation times could be probable as the supersaturation after a nucleation event is

still high. However, if this occurs for subsequent nucleation events a relatively longer incubation time is expected. This is a consequence of the large nanoparticle volume combined with the low availability of Sb atoms in the vapour phase. If several nucleation events happen in quick succession, there will be a significant reduction in Sb concentration in nanoparticle, and therefore supersaturation. Furthermore, the refill rate of nanoparticle will be slow due to the low availability of Sb in the vapour phase (due to low V/III ratio). Additionally, since the nanoparticle volume is large, the addition of Sb atoms has a relatively small impact on the concentration and by extension supersaturation (at least when compared to high V/III ratio = smaller nanoparticle volumes). The non-periodic, disordered behaviour ultimately results in a large spread for the modelled incubation times shown in Figure 4.12 (b), which also fits well with the experimental results depicted in Figure 4.9 (a).

To summarize, in this chapter the morphology and growth dynamics of Au-seeded GaSb nanowires was examined. In the first part of this chapter, the interplay between nanowire diameter and nanoparticle composition in response to vapour phase composition (V/III ratio) was discussed. This discussion culminated in demonstrating that these *in situ* observations can be effectively transferred to conventional systems. In the second half of this chapter the nanowire growth dynamics were investigated through experimental observations and modelling. This allowed us to demonstrate that the growth of GaSb nanowires is predominantly Sb-limited for the used growth conditions. Lastly, the experimentally observed non-trivial growth behaviour of these nanowires was explained through careful consideration of all present phases and species, with the same complex trends recreated in modelling.

5 GaSb/GaAs heterostructure formation

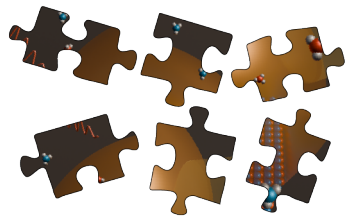

One of the main advantages of nanowires as a material system is the ability to combine different materials into axial and radial heterostructures. This is largely due to their efficient strain relaxation, and therefore the potential to form of epitaxial structures between lattice-mismatched materials. We already touched upon an example of axial heterostructures in Section 4.1.2 when discussing GaAs/GaSb heterostructure formation, where this heterostructure was used to study GaSb nanowire growth. Likewise, several other III-V combinations have been shown to result in axial heterostructures while retaining straight morphology.[31,32,94] However, we do not yet possess the ability to form axial heterostructures between arbitrary materials without nanowires kinking or changing growth direction. This is especially true for nanowires involving III-Sb, where numerous publications exist showcasing successful InAs/InSb and GaAs/GaSb axial heterostructures.[7,8,31,90,91] On the other hand studies for the opposite heterostructure directions are rare (As segment grown on top of Sb segment), especially for pure III-Sb to III-As binaries.[95,96]

The difficulty in forming III-Sb/III-As axial heterostructures is likely a combination of several factors. Firstly, Sb is a known surfactant material, which can have a strong effect on the interfacial energies of a system.[7] This can influence the morphology of axial heterostructure nanowires and exhibit different effects depending on the heterojunction direction (III-Sb/III-As or III-As/III-Sb).[32] Secondly, the low vapour pressure and higher solubility of Sb (in comparison to As) in Au nanoparticles during growth often causes difficulty in removing Sb from the growth system after III-Sb growth. This "contaminant effect" of the Sb is described by the reservoir and memory effects, when referring to Sb contamination in Au seed nanoparticle and growth reactors, respectively (albeit often these terms are used interchangeably).[95–97] The aforementioned causes ultimately limit our ability to form III-Sb/III-As axial heterostructures.[95,96]

In short, the formation of pure III-Sb/III-As axial heterostructures is an extremely challenging task not demonstrated in literature thus far. Having extensively studied the growth of Au-seeded GaSb nanowires *in situ* (as discussed in the previous chapter), it seemed only natural to pursue the question: "*What does it take to form Au-seeded GaSb/GaAs axial heterostructures?*". This was the focus of **Paper IV**. Answering this question would expand our "toolbox" of nanowire growth and enable growth of more complex multi-heterojunction nanowires.

5.1 Approaches to GaSb/GaAs axial heterostructure formation

The experiments discussed in this chapter were always started by directly nucleating Au-seeded GaSb nanowires using the approach discussed in Section 4.1.1. Once steady-state growth of GaSb nanowires was achieved we tested different growth conditions with the highlights discussed in this section.

As a starting point to obtain GaSb/GaAs axial heterostructures, the initial attempts were carried out by purging the group V line from TMSb using N_2 (the purging is described at the end of Section 2.3) and initiating a supply of AsH_3. This was done while having a constant flow of TMGa and staying at growth temperature. This approach was used as an inferred starting point from results of GaAs/GaSb heterojunction formation, since the sharp change in growth precursors could potentially have resulted in atomically sharp interfaces between the two materials.

A representative nanowire before and after carrying out such a procedure without residual TMSb in the gas line is demonstrated in Figure 5.1 (a). Here we can observe that after switching the precursors, the catalyst nanoparticle "eats into" the previously grown GaSb nanowire. This result suggests that the lack of Sb available for growth (due to stopping the supply of TMSb and instead initiating a supply of AsH_3) has a dramatic effect on the supersaturation. The etching of the existing nanowire suggests that the supersaturation is negative (chemical potential of the solid phase is higher than for the liquid phase). This in turn means that the solid GaSb is dissolved by the nanoparticle to maintain an equilibrium concentration of Sb in the nanoparticle, due to desorption from the nanoparticle to vapour phase. Etching of a nanowire by a liquid nanoparticle has previously been shown in Au-seeded GaAs nanowires by Tornberg et al.[77], and is the same principle used for "resetting the chip" in cases of suboptimal growth as described at the end of Section 3.1.

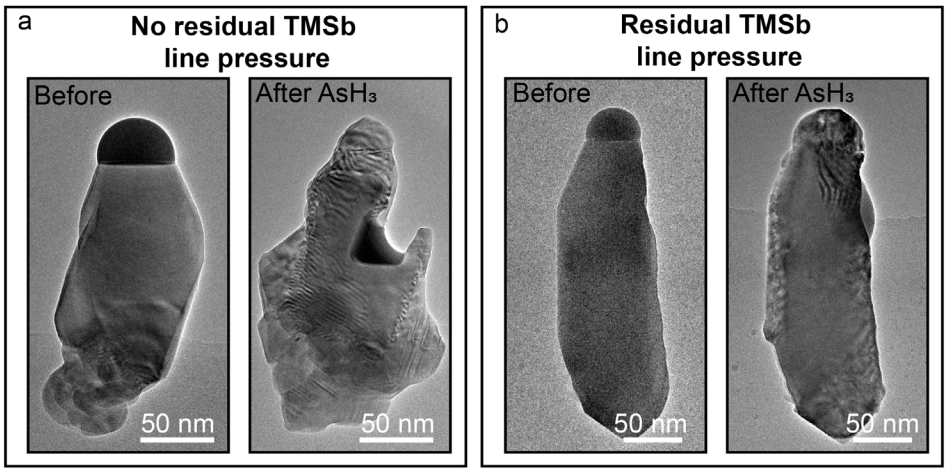

Figure 5.1 Summary of axial GaSb/GaAs heterostructure formation procedures. (a) Before and after HRTEM images of nanowires where full purging of group V line was used resulting in no residual TMSb pressure in the gas line. (b) Before and after HRTEM images of nanowires, where the group V line was not purged prior to initiating a supply of AsH_3. Figure adapted from **Paper IV**.

To circumvent the problem of the nanoparticle being toppled and etching the GaSb nanowire, we next attempted a procedure where heterostructure formation was carried out by stopping the TMSb flow and immediately starting the flow of AsH_3, without the intermediate step of purging group V line. A representative nanowire before and after this procedure in the gas lines is shown in Figure 5.1 (b). Here we can appreciate a marginal progress in the resulting nanowire morphology, as the presence of residual TMSb in the gas lines has mitigated the nanoparticle etching process. However, similarly to the previous case, the Au nanoparticle still migrates away from the original liquid-solid (LS) interface. In most cases, this was preceded by the growth of a crystalline island, which effectively pushed the nanoparticle off the LS interface. The sequence of nanowire kinking induced by formation of a 3D island can be seen in Figure 5.2. In Figure 5.2 (a), the GaSb nanowire shortly before the heterojunction formation is shown. When the growth conditions are changed to initiate the heterostructure formation, the nucleation and growth of a crystalline 3D island is observed, as shown by the black arrow in Figure 5.2 (b). This island rapidly grows in size, pushing the nanoparticle away from the original LS interface and resulting in kinking, which is depicted in Figure 5.2 (c).

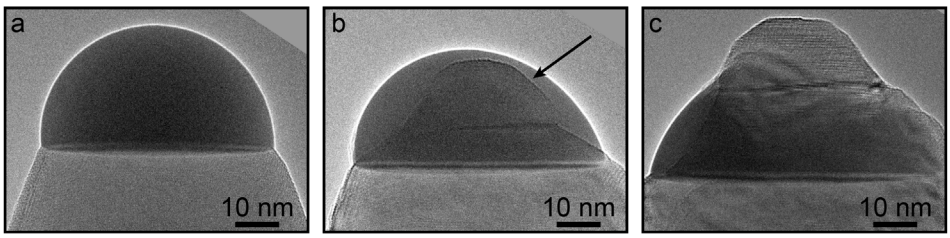

Figure 5.2 HRTEM images of nanowire kinking caused by formation of 3D island during GaSb/GaAs heterojunction formation. (a) GaSb nanowire before GaSb/GaAs heterostructure formation process. (b) During the formation of the heterojunction a crystalline island nucleates and grows in size (highlighted by the black arrow). As the island grows in size the nanoparticle pushed off the original LS interface and the nanowire kinks as shown in (c). Figure adapted from **Paper IV**.

We were also able to observe that on several occasions the toppling is caused by the formation of a multilayer stack. In multilayer growth, multiple layers grow at the same time, as opposed to the previously discussed layer-by-layer growth. Multilayer growth has recently also been observed to cause kinking during InGaAs nanowire growth.[98] An example of a multilayer stack prior to displacing the nanoparticle is shown in Figure 5.3. Specifically, in Figure 5.3 (a) a nanowire is shown shortly after the supply of AsH_3 is initiated to the microscope, where a stack of partially complete layers (multilayers) can be seen on the left side of the LS interface. Since the illustrated image is extracted from a video capturing the kinking process, it is not possible to determine the composition of the solid through XEDS. However, we can utilize the difference in lattice spacing between GaSb and GaAs, with Vegard's law to indirectly estimate the composition of the solid, by measuring the (111) plane lattice spacing. To clarify, Vegard's law in our specific case states that a ternary formed of two binary compounds, will have a lattice spacing that is a linear combination of the binary lattice parameters in accordance with Equation (5.1).

$$\mathrm{GaSb_xAs_{1-x}} = \mathrm{x} \cdot \mathrm{GaSb} + (1 - \mathrm{x}) \cdot \mathrm{GaAs} \tag{5.1}$$

To better visualize the difference in lattice spacing we can apply geometric phase analysis (GPA) to the original HRTEM image shown in Figure 5.3 (a) to obtain the colour plot depicted in Figure 5.3 (b). Here each image pixel represents a difference in distance between the $(\bar{1}1\bar{1})$ spot and the (000) spot (transmitted beam) in the fast-Fourier transform (FFT), resulting in a colour plot.

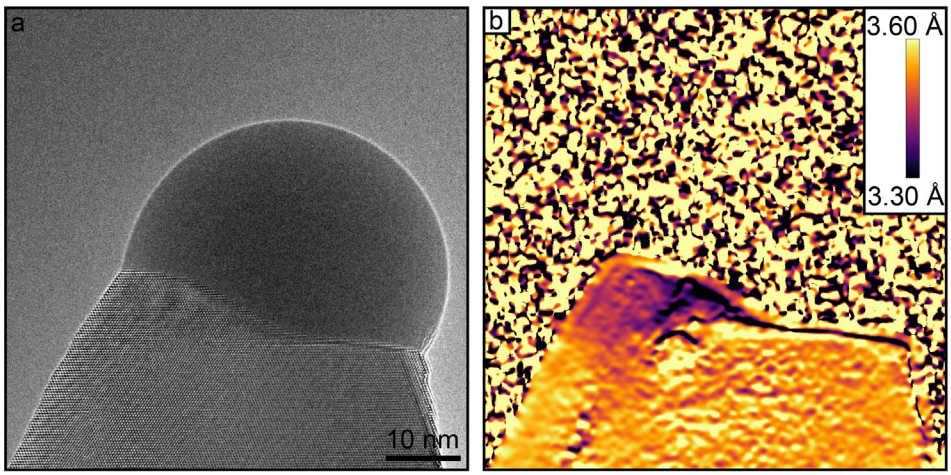

Figure 5.3 Nanowire kinking caused by multilayer growth during GaSb/GaAs heterojunction formation. (a) HRTEM image of a GaSb nanowire during GaSb/GaAs heterostructure formation process with a multilayer stack. (b) GPA treated image from (a), where the color represents (111) plane interplanar distance in Å. The smaller lattice spacing (darker color) represents a more As-rich composition (the multilayer stack). Figure adapted from **Paper IV**.

By comparing Figure 5.3 (b) with Figure 5.3 (a), it is evident that the multilayer stack exhibits a smaller lattice spacing in comparison to the rest of the nanowire (which is GaSb). This means that the multilayer stack is As-rich in accordance to Vegard's law. In terms of the growth dynamics, this implies that the nucleation of As-rich partial layers is energetically more preferred than completion of layers, resulting in the multilayer growth mode. These observations suggest that to enable successful growth of axial GaSb/GaAs heterostructures, an intermediate step of ternary $GaSb_xAs_{1-x}$ growth would be necessary, which was implemented in subsequent experiments.

To grow a ternary $GaSb_xAs_{1-x}$ segment that would allow formation of straight axial GaSb/GaAs heterostructures, a growth recipe was used that utilized a step of concurrent supply of TMGa, TMSb and AsH_3. The resulting nanowire heterostructure from such a growth recipe is shown in Figure 5.4 (a) (for compositional maps of this structure acquired using XEDS, see the supporting information of **Paper IV**). The growth recipe to attain such a structure is schematically shown in Figure 5.4 (b). Here, the TMGa partial pressure is kept constant (blue line) throughout the heterostructure formation process. To initiate the compositional switch, a supply of AsH_3 is started to the microscope (green line) in addition to the TMSb supply (shown in orange in the schematic). After 60 s of concurrent supply of TMSb and AsH_3, the supply of TMSb is stopped and the AsH_3 partial pressure is increased. The growth conditions for the GaAs (following the growth of the ternary segment) were chosen to support growth of

WZ GaAs.[21,42] This, combined with the fact that growth of GaSb nanowire always occurs in a ZB crystal phase, allowed us to indirectly track the compositional change occurring in the nanowire as well as provided information on crystal phase selection during heterostructure formation.[91] This will be discussed in more detail in Section 5.2.2. A close-up image of the dashed region from panel (a) is shown in Figure 5.4 (c), where the majority of the compositional switch occurs. This can be inferred by the presence of strain fields (illustrated by the white arrow) which occur due to an As-rich solid overgrowing on the GaSb core.

In the following sections we will take a closer look at the dynamics of the heterojunction formation process and discuss the real-time information that can be extracted from *in situ* videos acquired during growth.

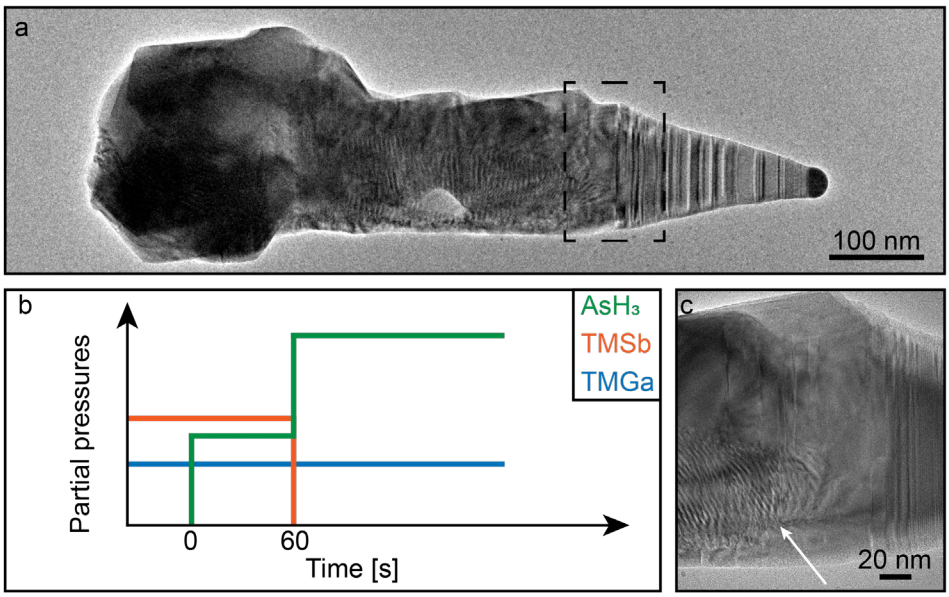

Figure 5.4 Summary of the succesful ternary approach for growth of axial GaSb/GaAs heterostructures. (a) HRTEM overview image of an axial GaSb/GaAs nanowire heterostructure. (b) Schematic overview of the percursor balance that enabled the heterostructure formation. (c) HRTEM close-up image of the dashed region from (a) where the majority of the compositional switching occurs. The white arrow points towards the area in the nanowire where strain fields are visible due to As-rich overgrowth on the GaSb nanowire core. Figure adapted from **Paper IV**.

5.2 Dynamics of the heterojunction formation

In order to gain information on the growth dynamics, the *in situ* videos were analysed with the specific focus on extracting quantitative parameters such as nanoparticle volume, growth rate and lattice spacing. By tracking the change in these parameters as a function of time, it is possible to infer information about the kinetics of growth, as well as composition of the solid nanowire.

In Figure 5.5 (a) the Au-seeded GaSb nanowire is shown 18 s before the supply of AsH_3 is initiated to the microscope (as indicated by the timestamp in the lower left corner of the panel). As can be seen from the FFT shown in the inset, the nanowire is in a ZB crystal phase imaged along the $[1\bar{1}0]$ zone axis. In Figure 5.5 (b), the nanoparticle volume, growth rate, and lattice spacing (measured near the LS interface) are summarized as a function of time throughout the heterojunction formation. The data plotted with blue circles refer to the nanowire growing in ZB crystal phase, whereas the blue rhombus shapes refer to the nanowire growing in 4H-WZ mixed crystal phase. Additionally, 5 key moments are shown in the graphs by numbered circles and dashed grey lines, which are as follows:

① AsH_3 supply is initiated (corresponds to time of 0 s in the graphs);

② TMSb supply to the microscope is stopped/AsH_3 partial pressure is increased;

③ Growth rate starts to rapidly increase/lattice spacing decreases;

④ Twinning is observed in the nanowire;

⑤ Nanowire starts to form WZ segments.

In Figure 5.5 (c) the same nanowire is shown 713 s after initiating the AsH_3 supply to the microscope (as indicated by the timestamp). Here we can see that the nanoparticle and nanowire dimensions have significantly reduced in comparison to Figure 5.5 (a), as indicated by the red dashed outline showing the original nanoparticle dimensions. Furthermore, from the FFT pattern we can observe that the topmost region in the nanowire is in a WZ crystal phase imaged along the $[11\bar{2}0]$ zone axis.

If we start to examine the dynamics by looking at the nanoparticle volume as a function of time (topmost graph in Figure 5.5 (b)), we can see that it remains largely unaffected by the onset of AsH_3 supply (indicated by dashed line (1)). As time progresses, shortly before stopping the supply of TMSb (dashed line (2)), an increase in nanoparticle volume can be observed which peaks shortly after the TMSb supply is stopped. By examining the growth rate for this same period (up until ≈ 80 s mark) we can see that the increase in nanoparticle volume is caused by the axial growth rate dropping to zero.

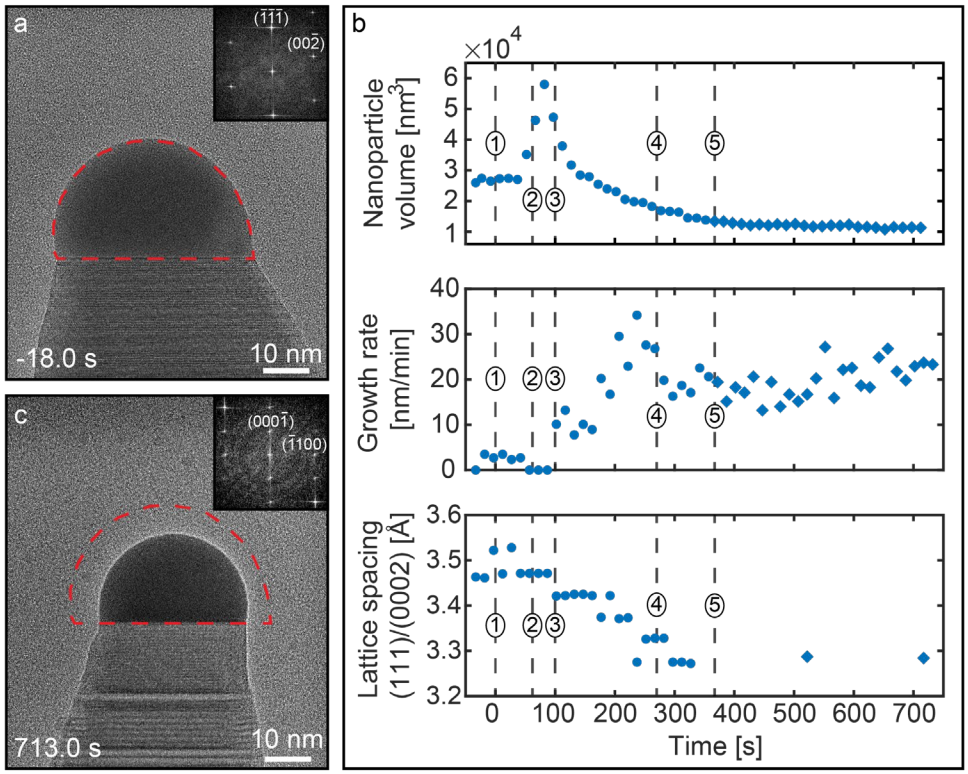

Figure 5.5 Summary of the data extracted from the *in situ* video capturing the GaSb/GaAs heterojunction formation. (a) HRTEM image of a Au-seeded GaSb 18 s before commencing the supply of AsH_3. Inset shows an FFT of the crystal region near the LS interface indicating that it is ZB oriented to the $[1\bar{1}0]$ zone axis. (b) Change in nanoparticle volume, growth rate and (111)/(0002) lattice spacing as a function of time extracted from the *in situ* video of the heterojunction formation. The dashed numbered lines in the plots indicate: (1) time when AsH_3 is supplied to the microscope, (2) AsH_3 supply is increased/TMSb supply is stopped, (3) nanowire growth rate rapidly increases/lattice spacing decreases, (4) nanowire starts to form ZB twins (5) nanowire starts to form WZ segments. Data marked with blue circles and blue diamonds indicate when the nanowire grows in a ZB and a 4H-WZ regime, respectively. (c) HRTEM image of a Au-seeded GaAs nanowire 713.0 s after commencing the supply of AsH_3. Inset shows an FFT of the crystal region near the LS interface indicating that it is WZ oriented to the $[11\bar{2}0]$ zone axis. Red dashed outline in (a) and (c) is used as a guide to the eye, depicting change in nanoparticle dimensions when nanowire growth is changed from GaSb to GaAs. Figure adapted from **Paper IV**.

The combination of zero axial growth and increasing nanoparticle volume suggests an increase in the nucleation barrier when TMSb supply is stopped/AsH_3 partial pressure is increased. The theorized mechanism is that this is likely caused by the vapour phase being AsH_3 rich (and relatively depleted of TMSb), which forces the nucleation of an As-rich $GaSb_xAs_{1-x}$. However, as there is a 7.8 % lattice mismatch between GaAs and GaSb, the interfacial strain increases the nucleation barrier in accordance with Equation (1.5). To overcome the increased nucleation barrier, the nanoparticle has to accumulate

more material to increase the liquid chemical potential, which increases the supersaturation until nucleation can occur.

In Figure 5.5 (b), the point where sufficient supersaturation is reached to continue nanowire growth is indicated by dashed line (3) (around the 100 s mark). At this point, the axial growth restarts and rapidly increases, while the nanoparticle volume sharply decreases. The cause for this dramatic change in the growth dynamics is due to the change in nanowire composition. This can be inferred from measuring the (111)/(0002) lattice spacing as shown in the bottom graph of Figure 5.5 (b). Since GaAs has a smaller lattice parameter than GaSb, a smaller measured lattice spacing of the (111)/(0002) planes suggests an As-rich ternary $GaSb_xAs_{1-x}$ compound (and later on pure GaAs), as confirmed by XEDS analysis (see the supporting information of **Paper IV**). As discussed in Chapter 4 during steady-state growth of Au-seeded GaSb nanowire, the Ga concentration in nanoparticle is approximately 66-94 at.%. This is in contrast to the lower Ga concentration in the Au nanoparticle during steady-state growth of GaAs (around 25-55 at.%).[42] Therefore, when the nanowire composition becomes more As-rich, the nanoparticle composition far exceeds that required for steady-state GaAs growth, resulting in a massive increase in growth rate and decrease in nanoparticle volume.

At around 270 s the nanowire growth rate stabilizes, which coincides with the time when twinning in the nanowire could first be observed (as indicated by the dashed line (4) in Figure 5.5 (b)). Subsequently, at around the 380 s mark, the nanowire started to form 4H-WZ segments as indicated by the dashed line (5) in Figure 5.5 (b). Only at this point were both the nanoparticle volume and the lattice spacing of (111)/(0002) planes observed to be stable. This indicated that the nanowire has reached a steady-state growth regime. In summary, we have formed an axial heterostructure going from a GaSb nanowire with a diameter of 42 nm growing in ZB crystal phase shown in Figure 5.5 (a), to a GaAs nanowire with a diameter of 32 nm growing in WZ crystal phase shown in Figure 5.5 (c).

5.2.1 Sharpness of the compositional switch

The measurements of lattice spacing of (111)/(0002) planes, shown in Figure 5.5 (b), indicate the compositional change occurring during heterostructure formation. However, they fail to convey the length of the ternary region. To visualize the length of the transition region we can once more utilize GPA. In Figure 5.6 (a) an image of the same nanowire discussed in Figure 5.5 is shown at the 247 s mark (recall that the timestamp refers to time elapsed since AsH_3 supply and by extent heterostructure formation is started). A complementary GPA colour plot of this same nanowire is

shown in Figure 5.6 (b), where the colour depicts interplanar spacing for the (111) lattice planes. The smaller lattice spacing (darker colour) indicates an As-rich ternary $GaSb_xAs_{1-x}$ compound, while the larger lattice spacing indicates GaSb (light yellow colour). By comparing the GPA-treated image with the real space image, it becomes apparent that the compositional switch i.e. length of ternary $GaSb_xAs_{1-x}$ region is approximately 50 nm.

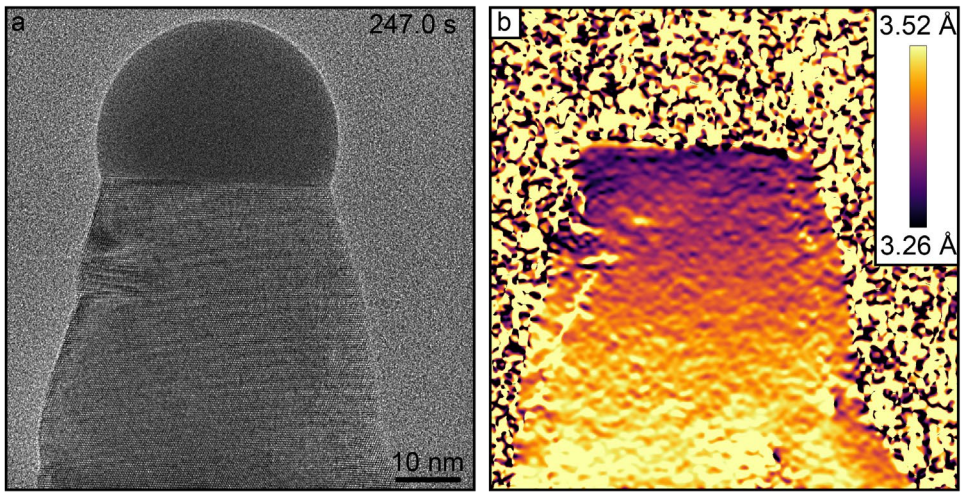

Figure 5.6 Length of the ternary region between GaSb and GaAs. (a) HRTEM image of a nanowire during the GaSb/GaAs heterostructure formation process 247 s after initaing the supply of AsH_3. (b) GPA treated image from (a), where the color represents (111) interplanar distance in Å. The smaller lattice spacing (darker color) represents a more As-rich composition. Figure adapted from **Paper IV**.

5.2.2 Crystal phase stability

By correlating the change in lattice spacing with the onset of twinning (dashed line (4)) and the first appearance of 4H-WZ (dashed line (5)) in Figure 5.5 (b) it becomes apparent that the change in crystal structure seemingly lags relative to morphological changes in the nanowire. To investigate why this happens we analysed the data extracted from the residual gas analyser (RGA) attached to the exhaust of our ETEM (see Figure 2.1). It is important to note that since the RGA is in the exhaust line of the ETEM, it is not an exact representation of the gas environment at the sample; however, it gives an indication of the precursor ratio present in the gas phase.[55,60]

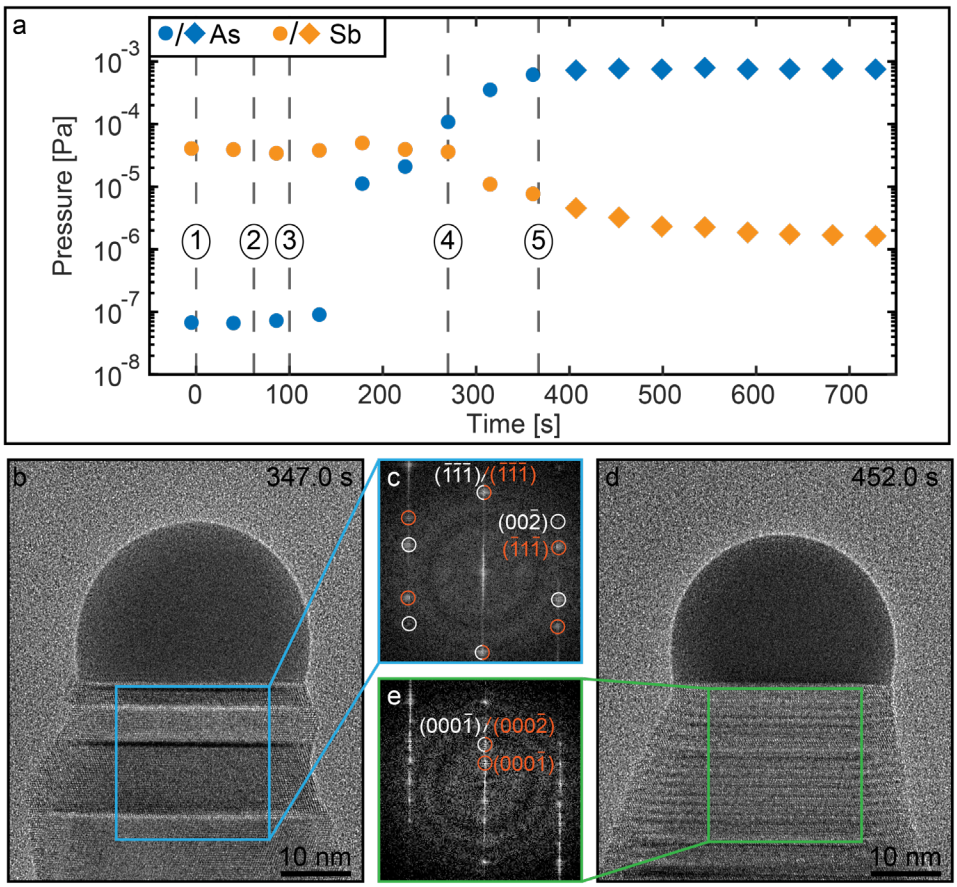

Figure 5.7 Evolution of crystal phase as a function of vapour phase composition. (a) RGA pressure data for As (blue shapes) and Sb (orange shapes) during the heterostructure formation process. The data marked with circles and diamonds indicate when the nanowire grows in a ZB and a 4H-WZ regime, respectively. In the plot dashed numbered lines indicate: (1) time when AsH_3 is supplied to the microscope, (2) AsH_3 supply is increased/TMSb supply is stopped, (3) nanowire growth rate rapidly increases/lattice spacing decreases, (4) nanowire starts to grow in twinned ZB crystal structure (5) nanowire starts to form WZ segments. (b) HRTEM image of a Au-seeded GaAs nanowire during growth 347.0 s after commencing supply of AsH_3. (c) FFT of the crystal region marked by the blue box in (b) revealing a twinned ZB crystal phase. Select reflections for the two rotational twins are illustrated using white and orange circles in the FFT. (d) HRTEM image of a Au-seeded GaAs nanowire during growth 452.0 s after commencing supply of AsH_3. (e) FFT of the crystal region marked by the green box in (d) revealing a predominantly 4H crystal phase. Select reflections for WZ and 4H crystal phase are shown in white and orange, respectively, to show that 4H has double periodicity of WZ. Figure adapted from **Paper IV**.

In Figure 5.7 (a) the RGA data acquired during the axial GaSb/GaAs heterostructure formation process is shown. Similarly to Figure 5.5 (b), also in Figure 5.7 (a) the five key moments occurring during heterojunction formation are depicted with dashed lines (see the list at the beginning of Section 5.2 or caption of Figure 5.7). From the RGA data in Figure 5.7 (a), it is clear that the observed rapid increase in growth rate, and

decrease in lattice spacing (marked by the dashed line (3) in Figure 5.5 (b) and Figure 5.7 (a)) corresponds to the point where As pressure, measured by RGA, starts to rapidly increase. With As pressure continuing to increase at 270 s, we can first observe formation of ZB twins in the nanowire as indicated by dashed line (4) in Figure 5.7 (a). An image displaying the twinning in the nanowire at 347 s into the heterojunction formation process is depicted in Figure 5.7 (b). A complementary FFT pattern of the highlighted blue region is also shown in Figure 5.7 (c). Here the reflections of the two rotational ZB twins are highlighted with white and orange circles.

When the As pressure reaches its peak and the Sb pressure approaches a measured minimal value, we first observe formation of 4H-WZ segments in the nanowire, as indicated by dashed line (5) in Figure 5.7 (a). This can be seen in Figure 5.7 (d), where an image of a nanowire at 452 s into the heterojunction formation is shown, with a complementary FFT pattern of the highlighted green box shown in Figure 5.7 (e). Here the orange circles are used to mark 4H reflections seen in the FFT, with WZ reflections shown in white for reference to illustrate that 4H has double the periodicity of WZ. From Figure 5.7 it is evident that the change in crystal phase is strongly influenced by the partial pressures of As and Sb, and/or the As/Sb ratio in the vapour phase. These observations agree with previous reports in conventional growth systems involving the growth of III-As and III-Sb nanowires.[91,95,97] Here the Sb residues present in the growth reactor were theorized to affect the nanowire crystal phase due to its surfactant nature that can alter surface and interfacial energies, which determine the crystal phase selection of nanowires.[7]

The onset of the change from ZB to a mixed regime, and ultimately WZ crystal phase displays a good match with the RGA data of the vapour phase composition. However, trace amounts of Sb (in the range of 1-2 at.%) could still be present in the solid nanowire and/or the liquid nanoparticle during the heterojunction formation process. Such trace amounts could have a significant effect on the energy balance between the nanoparticle and nanowire, while having negligible impact on the lattice spacing and being below the detection limit of XEDS at the growth temperature.[60,95]

The observations of ZB being the preferred crystal phase until full compositional switch from GaSb to GaAs are in line with previous works involving III-Sb materials.[28,91,95–97] In general III-Sb nanowires favour growth in a ZB crystal phase.[91] Ternary segments of antimonides often exhibit a mixed structure (although this is highly dependent on the Sb concentration in the ternary $GaSb_xAs_{1-x}$ segment), whereas WZ crystal phase (of the GaAs) is attainable only at negligible or non-existent Sb background.[30,96,99] Therefore, the crystal phase in III-Sb/III-As heterostructures can be used as an extremely sensitive way to determine compositional purity.

The data presented in this chapter provided a detailed discussion on growth dynamics during the formation of axial GaSb/GaAs nanowire heterostructures. In the first part of this chapter we briefly discussed challenges and limitations of this heterostructure by finding an answer to the question: "*What does it take to form this heterostructure?*". Afterwards, we examined quantitative data, extracted from the *in situ* videos and RGA, to track nanowire and nanoparticle morphology, composition, and crystal phase purity. These observations allowed to infer information about kinetics of the heterostructure formation and determine the impact of vapour phase precursors on the growth process. In summary, the findings from this study provide knowledge of the requirements for successful formation of large lattice mismatched and/or antimonide containing axial heterostructures.

6 Concluding remarks and outlook

In this thesis I have described the results of *in situ* studies of III-V nanowire growth conducted in an ETEM. The main focus has been to investigate phenomena and address problems within nanowire growth that are impossible (or at least extremely challenging) to address by means of conventional growth studies and modelling. Before we discuss the potential future research directions that can originate from this thesis, let's briefly recap it.

- Chapter 1 was dedicated to establishing a theoretical basis of crystallization and nanowire growth.
- Chapter 2 focused on describing the main experimental system used in this work – The Lund Hitachi HF-3300S ETEM – as well as the most important TEM concepts.
- Chapter 3 showcased my work on investigating size effects in Au-seeded GaAs nanowires by studying the processes comprising layer-by-layer growth.
- Chapter 4 established a comprehensive understanding of the growth of Au-seeded GaSb nanowires. Here we closely examined the interplay between vapour phase precursors, liquid nanoparticle and solid nanowire from the aspects of composition, morphology and growth dynamics.
- Chapter 5 described the formation dynamics of axial GaSb/GaAs nanowire heterostructures. Here I discussed the formation of such heterojunctions as well as the observed morphological, compositional and crystal phase changes during growth.

Opening the black box of III-V nanowire growth is not a straightforward process and I would compare it to assembling a puzzle, where each new piece of knowledge we discover uncovers the black box only a little. Throughout the different chapters, we have acquired more and more of the puzzle pieces necessary to, so to speak, open the black box of the III-V nanowire growth and finally assemble the puzzle as shown in Figure 6.1. Within the context of III-V nanowire growth, this puzzle can be thought of as a small corner of a much larger puzzle consisting of thousands of pieces (and a

much bigger, darker box). Therefore, to uncover the larger picture we need to keep acquiring more puzzle pieces. So how do we do that?

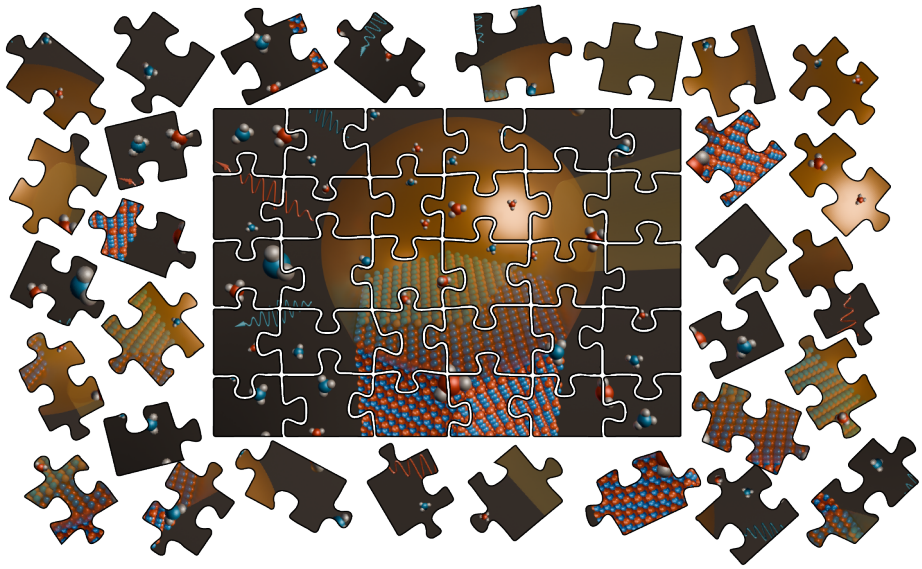

Figure 6.1 The assembled puzzle.

In my opinion, the most significant achievement of my work has been the successful development of GaSb nanowires as a viable materials system to study further *in situ*. Here the biggest unknown was always Sb and how it would behave in our ETEM. Through the studies in this thesis I have not only developed an understanding of GaSb as a materials system, but also elemental Sb. I hope that this will pave the way for continued studies involving Sb *in situ* with some potential ideas discussed below.

One of the more fascinating aspects of III-Sb nanowires is their crystal phase purity. These nanowires almost exclusively are found to be in ZB phase, with GaSb never demonstrated in WZ phase in axial nanowires. Although several different theories exist on why this is, to date we lack experimental information on the subject. To understand the crystal phase selection in III-Sb nanowires would undoubtedly aid in our goal to comprehend polytypism in general.

Furthermore, as we saw in Chapter 5 more exotic metastable crystal phases than WZ, such as 4H, are formed in heterostructures involving GaSb and GaAs. Here they are seen as a transient stage in the growth process when the nanowire and the vapour phase composition changed from GaSb to GaAs. If we can manage to capture and stabilize these fleeting conditions it could enable the controlled growth of 4H crystal segments. Similar to when pure WZ nanowires were first realized this would mark a significant

advancement in our control of the growth process. This is especially true since controlled growth of the higher metastable polytypes, such as 4H and 6H, has not yet been achieved for III-V nanowires.

Since our ETEM has been inaugurated my colleagues and I have managed to test a variety of III-V materials. However, if all possible combinations are considered we have barely scratched the surface. Among the more uncommon ones (and on top of my wishlist) are the AlSb nanowires. Little is known about these nanowires since no one can actually make them, with the only published works including AlSb as a part of core-shell structures.[100] The difficulty in growing these nanowires partly comes from Sb being a challenging material, but perhaps more so from Al due to its rapid oxidation. Because of the relatively low pressure and reducing environment, the ETEM could then present the perfect testing bed for developing procedures for the growth of AlSb nanowires. It is worth noting that my initial attempts to grow these nanowires in the ETEM failed precisely due to the rapid oxidation of deposited Al. This is something that could be potentially avoided if growth would occur in a more reducing environment or was conducted using an ultra-high vacuum ETEM.

The aforementioned project ideas all are based on III-V nanowire growth studies because it is something I know and love. However, the field of *in situ* crystal growth studies is expanding to new material combinations of different dimensionalities almost daily. This has led to *in situ* growth establishing itself more and more as a self-standing research field rather than just an extension of conventional CVD growth studies. This ability to see dynamic processes as they occur is incredibly important not only to improve our understanding of crystal growth, but also provide undeniable evidence of all the peculiar things that occur at the nanoscale. After all, it is not impossible that weird things happen, but it is much easier to believe when we can witness them first-hand. Therefore, it is not so much that I hope for my work to inspire future research into III-V nanowires (although I would love that too), but rather inspire growth and study of complex, challenging and exciting materials *in situ*.

References

(1) Moore, G. E. Cramming More Components onto Integrated Circuits. *Proc. IEEE* **1998**, *86* (1), 82–85.

(2) Barrigón, E.; Heurlin, M.; Bi, Z.; Monemar, B.; Samuelson, L. Synthesis and Applications of III-V Nanowires. *Chem. Rev.* **2019**, *119* (15), 9170–9220.

(3) Das, S.; Kim, M.; Lee, J. W.; Choi, W. Synthesis, Properties, and Applications of 2-D Materials: A Comprehensive Review. *Crit. Rev. Solid State Mater. Sci.* **2014**, *39* (4), 231–252.

(4) García de Arquer, F. P.; Talapin, D. V.; Klimov, V. I.; Arakawa, Y.; Bayer, M.; Sargent, E. H. Semiconductor Quantum Dots: Technological Progress and Future Challenges. *Science* **2021**, *373* (6555).

(5) McIntyre, P. C.; Fontcuberta i Morral, A. Semiconductor Nanowires: To Grow or Not to Grow? *Mater. Today Nano* **2020**, *9*, 100058.

(6) Dick, K. A. A Review of Nanowire Growth Promoted by Alloys and Non-Alloying Elements with Emphasis on Au-Assisted III-V Nanowires. *Prog. Cryst. Growth Charact. Mater.* **2008**, *54* (3–4), 138–173.

(7) Mattias Borg, B.; Wernersson, L.-E. E. Synthesis and Properties of Antimonide Nanowires. *Nanotechnology* **2013**, *24* (20), 202001.

(8) Yip, S.; Shen, L.; Ho, J. C. Recent Advances in III-Sb Nanowires: From Synthesis to Applications. *Nanotechnology* **2019**, *30* (20).

(9) Carter, B. C.; Williams, D. B. *Transmission Electron Microscopy*; Springer Science & Business Media, 2009.

(10) Persson, A. I.; Larsson, M. W.; Stenström, S.; Ohlsson, B. J.; Samuelson, L.; Wallenberg, L. R. Solid-Phase Diffusion Mechanism for GaAs Nanowire Growth. *Nat. Mater.* **2004**, *3* (10), 677–681.

(11) Dubrovskii, V. G. Mono- and Polynucleation, Atomistic Growth, and Crystal Phase of III-V Nanowires under Varying Group v Flow. *J. Chem. Phys.* **2015**, *142* (20).

(12) Johansson, J.; Svensson, C. P. T.; Mårtensson, T.; Samuelson, L.; Seifert, W. Mass Transport Model for Semiconductor Nanowire Growth. *J. Phys. Chem. B* **2005**, *109* (28), 13567–13571.

(13) Glas, F.; Harmand, J. C.; Patriarche, G. Nucleation Antibunching in Catalyst-Assisted Nanowire Growth. *Phys. Rev. Lett.* **2010**, *104* (13), 2–5.

(14) Lehmann, S.; Jacobsson, D.; Dick, K. A. Crystal Phase Control in GaAs Nanowires: Opposing Trends in the Ga- and As-Limited Growth Regimes. *Nanotechnology* **2015**, *26* (30).

(15) Jiang, N.; Wong-leung, J.; Joyce, H. J.; Gao, Q.; Tan, H. H.; Jagadish, C. Understanding the True Shape of Au-Catalyzed GaAs Nanowires. **2014**.

(16) Joyce, H. J.; Wong-Leung, J.; Gao, Q.; Hoe Tan, H.; Jagadish, C. Phase Perfection in Zinc Blende and Wurtzite III- V Nanowires Using Basic Growth Parameters. *Nano Lett.* **2010**, *10* (3), 908–915.

(17) Dick, K. A. Gas-Phase Materials Synthesis in Environmental Transmission Electron Microscopy. *MRS Bull.* **2023**, *48* (August), 1–9.

(18) Reidy, K.; Thomsen, J. D.; Ross, F. M. Perspectives on Ultra-High Vacuum Transmission Electron Microscopy of Dynamic Crystal Growth Phenomena. *Prog. Mater. Sci.* **2023**, 101163.

(19) Harmand, J.; Patriarche, G.; Glas, F.; Panciera, F.; Florea, I.; Maurice, J.; Travers, L.; Ollivier, Y. Atomic Step Flow on a Nanofacet. *Phys. Rev. Lett.* **2018**, *121* (16), 166101.

(20) Glas, F.; Harmand, J.; Patriarche, G. Why Does Wurtzite Form in Nanowires of III-V Zinc Blende Semiconductors ? *Phys. Rev. Lett.* **2007**, *146101* (October), 3–6.

(21) Maliakkal, C. B.; Mårtensson, E. K.; Tornberg, M. U.; Jacobsson, D.; Persson, A. R.; Johansson, J.; Wallenberg, L. R.; Dick, K. A. Independent Control of Nucleation and Layer Growth in Nanowires. *ACS Nano* **2020**, *14* (4), 3719–5150.

(22) Dubrovskii, V. G. *Nucleation Theory and Growth of Nanostructures*; 2014.

(23) Dick, K. A.; Caroff, P.; Bolinsson, J.; Messing, M. E.; Johansson, J.; Deppert, K.; Wallenberg, L. R.; Samuelson, L. Control of III-V Nanowire Crystal Structure by Growth Parameter Tuning. *Semicond. Sci. Technol.* **2010**, *25* (2).

(24) Heurlin, M.; Lindgren, D.; Deppert, K.; Samuelson, L.; Magnusson, M. H.; Ek, M. L.; Wallenberg, R. Continuous Gas-Phase Synthesis of Nanowires with

Tunable Properties. *Nature* **2012**, *492* (7427), 90–94.

(25) Lehmann, S.; Wallentin, J.; Mårtensson, E. K.; Ek, M.; Deppert, K.; Dick, K. A.; Borgström, M. T. Simultaneous Growth of Pure Wurtzite and Zinc Blende Nanowires. *Nano Lett.* **2019**, *19* (4), 2723–2730.

(26) Maliakkal, C. B.; Jacobsson, D.; Tornberg, M.; Dick, K. A. Post-Nucleation Evolution of the Liquid-Solid Interface in Nanowire Growth. *Nanotechnology* **2022**, *33* (10).

(27) Momma, Koichi and Izumi, F. VESTA 3 for Three-Dimensional Visualization of Crystal, Volumetric and Morphology Data. *J. Appl. Crystallogr.* **2011**, *44* (6), 1272–1276.

(28) Johansson, J.; Bolinsson, J.; Ek, M.; Caroff, P.; Dick, K. A. Combinatorial Approaches to Understanding Polytypism in III-V Nanowires. *ACS Nano* **2012**, *6* (7), 6142–6149.

(29) Jacobsson, D.; Yang, F.; Hillerich, K.; Lenrick, F.; Lehmann, S.; Kriegner, D.; Stangl, J.; Wallenberg, L. R.; Dick, K. A.; Johansson, J. Phase Transformation in Radially Merged Wurtzite GaAs Nanowires. *Cryst. Growth Des.* **2015**, *15* (10), 4795–4803.

(30) Dheeraj, D. L.; Patriarche, G.; Zhou, H.; Hoang, T. B.; Moses, A. F.; Grønsberg, S.; Van Helvoort, A. T. J.; Fimland, B. O.; Weman, H. Growth and Characterization of Wurtzite GaAs Nanowires with Defect-Free Zinc Blende GaAsSb Inserts. *Nano Lett.* **2008**, *8* (12), 4459–4463.

(31) De La Mata, M.; Magén, C.; Caroff, P.; Arbiol, J. Atomic Scale Strain Relaxation in Axial Semiconductor III-V Nanowire Heterostructures. *Nano Lett.* **2014**, *14* (11), 6614–6620.

(32) Dick, K. A.; Kodambaka, S.; Reuter, M. C.; Deppert, K.; Samuelson, L.; Seifert, W.; Wallenberg, L. R.; Ross, F. M. The Morphology of Axial and Branched Nanowire Heterostructures. *Nano Lett.* **2007**, *7* (6), 1817–1822.

(33) Wang, N.; Cai, Y.; Zhang, R. Q. Growth of Nanowires. *Mater. Sci. Eng. R Reports* **2008**, *60* (1–6), 1–51.

(34) Stringfellow, G. B. *Organometallic Vapor Phase Epitaxy*, 2nd ed.; Elsevier, 1999.

(35) Andre, C. L.; El-Zein, N.; Tran, N. Bubbler for Constant Vapor Delivery of a Solid Chemical. *J. Cryst. Growth* **2007**, *298* (SPEC. ISS), 168–171.

(36) Mountziaris, T. J.; Jensen, K. F. Gas-Phase and Surface Reaction Mechanisms in MOCVD of GaAs with Trimethyl-Gallium and Arsine. *J. Electrochem. Soc.*

1991, *138* (8), 2426–2439.

(37) Nishizawa, J. and Kurabayashi, T. Mechanism of Gallium Arsenide MOCVD. *Vacuum* **1990**, *41* (3), 958–962.

(38) Nishizawa, J. ichi; Kurabayashi, T. On the Reaction Mechanism of GaAs MOCVD. *J. Cryst. Growth* **1990**, *99* (1–4), 525–529.

(39) Pohl, U. W. *Epitaxy of Semiconductors Physics and Fabrication of Heterostructures*; 2020.

(40) Wagner, R. S.; Ellis, W. C. Vapor-Liquid-Solid Mechanism of Single Crystal Growth. *Appl. Phys. Lett.* **1964**, *4* (5), 89–90.

(41) Dick, K. A.; Caroff, P. Metal-Seeded Growth of III-V Semiconductor Nanowires: Towards Gold-Free Synthesis. *Nanoscale* **2014**, *6* (6), 3006–3021.

(42) Maliakkal, C. B.; Jacobsson, D.; Tornberg, M.; Persson, A. R.; Johansson, J.; Wallenberg, R.; Dick, K. A. In Situ Analysis of Catalyst Composition during Gold Catalyzed GaAs Nanowire Growth. *Nat. Commun.* **2019**, *10* (1).

(43) Mandl, B.; Stangl, J.; Hilner, E.; Zakharov, A. A.; Hillerich, K.; Dey, A. W.; Samuelson, L.; Bauer, G.; Deppert, K.; Mikkelsen, A. Growth Mechanism of Self-Catalyzed Group III-V Nanowires. *Nano Lett.* **2010**, *10* (11), 4443–4449.

(44) Güniat, L.; Caroff, P.; Fontcuberta I Morral, A. Vapor Phase Growth of Semiconductor Nanowires: Key Developments and Open Questions. *Chem. Rev.* **2019**, *119* (15), 8958–8971.

(45) Wacaser, B. A.; Dick, K. A.; Johansson, J.; Borgström, M. T.; Deppert, K.; Samuelson, L. Preferential Interface Nucleation: An Expansion of the VLS Growth Mechanism for Nanowires. *Adv. Mater.* **2009**, *21* (2), 153–165.

(46) Dubrovskii, V. G.; Sibirev, N. V.; Cirlin, G. E.; Harmand, J. C.; Ustinov, V. M. Theoretical Analysis of the Vapor-Liquid-Solid Mechanism of Nanowire Growth during Molecular Beam Epitaxy. *Phys. Rev. E - Stat. Nonlinear, Soft Matter Phys.* **2006**, *73* (2), 1–10.

(47) Dubrovskii, V. G.; Sibirev, N. V.; Harmand, J. C.; Glas, F. Growth Kinetics and Crystal Structure of Semiconductor Nanowires. *Phys. Rev. B - Condens. Matter Mater. Phys.* **2008**, *78* (23), 1–10.

(48) Krogstrup, P.; Jørgensen, H. I.; Johnson, E.; Madsen, M. H.; Sørensen, C. B.; Morral, A. F. I.; Aagesen, M.; Nygård, J.; Glas, F. Advances in the Theory of III-V Nanowire Growth Dynamics. *J. Phys. D. Appl. Phys.* **2013**, *46* (31).

(49) Dubrovskii, V. G. Influence of the Group v Element on the Chemical Potential and Crystal Structure of Au-Catalyzed III-V Nanowires. *Appl. Phys. Lett.* **2014**, *104* (5).

(50) Jacobsson, D.; Panciera, F.; Tersoff, J.; Reuter, M. C.; Lehmann, S.; Hofmann, S.; Dick, K. A.; Ross, F. M. Interface Dynamics and Crystal Phase Switching in GaAs Nanowires. *Nature* **2016**, *531* (7594), 317–322.

(51) Sjökvist, R.; Jacobsson, D.; Tornberg, M.; Wallenberg, R.; Leshchenko, E. D.; Johansson, J.; Dick, K. A. Compositional Correlation between the Nanoparticle and the Growing Au-Assisted InxGa1-XAs Nanowire. *J. Phys. Chem. Lett.* **2021**, *12* (31), 7590–7595.

(52) Glas, F.; Ramdani, M. R.; Patriarche, G.; Harmand, J. Predictive Modeling of Self-Catalyzed III-V Nanowire Growth. *Phys. Rev. B* **2013**, *195304* (May), 1–14.

(53) Gil, E.; Dubrovskii, V. G.; Avit, G.; André, Y.; Leroux, C.; Lekhal, K.; Grecenkov, J.; Trassoudaine, A.; Castelluci, D.; Monier, G.; Ramdani, R. M.; Robert-Goumet, C.; Bideux, L.; Harmand, J. C.; Glas, F. Record Pure Zincblende Phase in GaAs Nanowires down to 5 Nm in Radius. *Nano Lett.* **2014**, *14* (7), 3938–3944.

(54) Müller, H.; Maßmann, I.; Uhlemann, S.; Hartel, P.; Zach, J.; Haider, M. Aplanatic Imaging Systems for the Transmission Electron Microscope. *Nucl. Instruments Methods Phys. Res. Sect. A Accel. Spectrometers, Detect. Assoc. Equip.* **2011**, *645* (1), 20–27.

(55) Hetherington, C.; Jacobsson, D.; Dick, K. A.; Wallenberg, L. R. In Situ Metal-Organic Chemical Vapour Deposition Growth of III-V Semiconductor Nanowires in the Lund Environmental Transmission Electron Microscope. *Semicond. Sci. Technol.* **2020**, *35* (3).

(56) Goldstein, J. I.; Newbury, D. E.; Michael, J. R.; Ritchie, N. W. M.; Scott, J. H. J.; Joy, D. C. *Scanning Electron Microscopy and X-Ray Microanalysis*; 2018.

(57) Cliff, G.; Lorimer, G. W. The Quantitative Analysis of Thin Specimens. *J. Microsc.* **1975**, *103* (2), 203–207.

(58) Watanabe, M.; Williams, D. B. The Quantitative Analysis of Thin Specimens: A Review of Progress from the Cliff-Lorimer to the New ζ-Factor Methods. *J. Microsc.* **2006**, *221* (2), 89–109.

(59) Joy, David C., Alton D. Romig, and J. G. *Basic Principles of Analytical Electron Microscopy*; Springer Science & Business Media, 1986.

(60) Tornberg, M.; Maliakkal, C. B.; Jacobsson, D.; Wallenberg, R.; Dick, K. A. Enabling In Situ Studies of Metal-Organic Chemical Vapor Deposition in a Transmission Electron Microscope . *Microsc. Microanal.* **2022**, *28* (5), 1–9.

(61) Song, B.; Yang, Y.; Yang, T. T.; He, K.; Hu, X.; Yuan, Y.; Dravid, V. P.; Zachariah, M. R.; Saidi, W. A.; Liu, Y.; Shahbazian-Yassar, R. Revealing High-Temperature Reduction Dynamics of High-Entropy Alloy Nanoparticles via in Situ Transmission Electron Microscopy. *Nano Lett.* **2021**, *21* (4), 1742–1748.

(62) Yokosawa, T.; Alan, T.; Pandraud, G.; Dam, B.; Zandbergen, H. In-Situ TEM on (de)Hydrogenation of Pd at 0.5-4.5bar Hydrogen Pressure and 20-400°C. *Ultramicroscopy* **2012**, *112* (1), 47–52.

(63) Kim, J.; Kang, S.; Cheng, F.; Wang, Y.; Ye, X.; Park, J. Recent Advances in Liquid Phase Transmission Electron Microscopy of Nanoparticle Growth and Self-Assembly. *MRS Bull.* **2024**, *49* (4), 365–376.

(64) Krisper, R.; Lammer, J.; Pivak, Y.; Fisslthaler, E.; Grogger, W. The Performance of EDXS at Elevated Sample Temperatures Using a MEMS-Based In Situ TEM Heating System. *Ultramicroscopy* **2022**, *234* (August 2021), 113461.

(65) Mårtensson, E. K.; Lehmann, S.; Dick, K. A.; Johansson, J. Effect of Radius on Crystal Structure Selection in III–V Nanowire Growth. *Cryst. Growth Des.* **2020**, *20* (8), 5373–5379.

(66) Fröberg, L. E.; Seifert, W.; Johansson, J. Diameter-Dependent Growth Rate of InAs Nanowires. *Phys. Rev. B* **2007**, *76* (15), 1–4.

(67) Kashchiev, D. Dependence of the Growth Rate of Nanowires on the Nanowire Diameter. *Cryst. Growth Des.* **2006**, *6* (5), 1154–1156.

(68) Dubrovskii, V. G.; Sibirev, N. V.; Cirlin, G. E.; Soshnikov, I. P.; Chen, W. H.; Larde, R.; Cadel, E.; Pareige, P.; Xu, T.; Grandidier, B.; Nys, J. P.; Stievenard, D.; Moewe, M.; Chuang, L. C.; Chang-Hasnain, C. Gibbs-Thomson and Diffusion-Induced Contributions to the Growth Rate of Si, InP, and GaAs Nanowires. *Phys. Rev. B - Condens. Matter Mater. Phys.* **2009**, *79* (20), 1–7.

(69) Givargizov, E. I. Fundamental Aspects of VLS Growth. *J. Cryst. Growth* **1975**, *31* (C), 20–30.

(70) Nilsson, M.; Chen, I. J.; Lehmann, S.; Maulerova, V.; Dick, K. A.; Thelander, C. Parallel-Coupled Quantum Dots in InAs Nanowires. *Nano Lett.* **2017**, *17* (12), 7847–7852.

(71) Tedeschi, D.; De Luca, M.; Granados Del Águila, A.; Gao, Q.; Ambrosio, G.; Capizzi, M.; Tan, H. H.; Christianen, P. C. M.; Jagadish, C.; Polimeni, A. Value and Anisotropy of the Electron and Hole Mass in Pure Wurtzite InP Nanowires. *Nano Lett.* **2016**, *16* (10), 6213–6221.

(72) Beznasyuk, D. V.; Robin, E.; Hertog, M. Den; Claudon, J.; Hocevar, M. Dislocation-Free Axial InAs-on-GaAs Nanowires on Silicon. *Nanotechnology* **2017**, *28* (36).

(73) Glas, F. Critical Dimensions for the Plastic Relaxation of Strained Axial Heterostructures in Free-Standing Nanowires. *Phys. Rev. B - Condens. Matter Mater. Phys.* **2006**, *74* (12), 2–5.

(74) Magnusson, M. H.; Deppert, K.; Malm, J. O.; Bovin, J. O.; Samuelson, L. Size-Selected Gold Nanoparticles by Aerosol Technology. *Nanostructured Mater.* **1999**, *12* (1), 45–48.

(75) DeHoff, R. *Thermodynamics in Materials Science*; CRC Press, 2006.

(76) Buffat, P.; Borel, J. P. Size Effect on the Melting Temperature of Gold Particles. *Phys. Rev. A* **1976**, *13* (6), 2287–2298.

(77) Tornberg, M.; Jacobsson, D.; Persson, A. R.; Wallenberg, R.; Dick, K. A.; Kodambaka, S. Kinetics of Au – Ga Droplet Mediated Decomposition of GaAs Nanowires. *Nano Lett.* **2019**, *19* (6), 3498–3504.

(78) Givargizov, E. I. Perioidic Instability in Whisker Growth. *J. Cryst. Growth* **1973**, *20* (3), 217–226.

(79) Dubrovskii, V. G.; Sibirev, N. V. General Form of the Dependences of Nanowire Growth Rate on the Nanowire Radius. *J. Cryst. Growth* **2007**, *304* (2), 504–513.

(80) Seifert, W.; Borgström, M.; Deppert, K.; Dick, K. A.; Johansson, J.; Larsson, M. W.; Mårtensson, T.; Skold, N.; Svensson, C. P. T.; Wacaser, B. A.; Wallenberg, L. R.; Samuelson, L. Growth of One-Dimensional Nanostructures in MOVPE. *J. Cryst. Growth* **2004**, *272* (1-4 SPEC. ISS.), 211–220.

(81) Soci, C.; Bao, X.; Aplin, D. P. R.; Wang, D. A Systematic Study on the Growth of GaAs Nanowires by Metal - Organic Chemical Vapor Deposition. *Nano Lett.* **2008**, *8* (12), 4275–4282.

(82) Dubrovskii, V. G.; Sibirev, N. V. Growth Rate of a Crystal Facet of Arbitrary Size and Growth Kinetics of Vertical Nanowires. *Phys. Rev. E - Stat. Physics, Plasmas, Fluids, Relat. Interdiscip. Top.* **2004**, *70* (3), 7.

(83) Tornberg, M.; Maliakkal, C. B.; Jacobsson, D.; Dick, K. A.; Johansson, J. Limits of III – V Nanowire Growth Based on Droplet Dynamics. *J. Phys. Chem. Lett.* **2020**, *11* (8), 2949–2954.

(84) Lisak, A.; Fitzner, K. Vapor Pressure Measurements of Arsenic and Arsenic Trioxide over Condensed Phases. *J. Phase Equilibria* **1994**, *15* (2), 151–154.

(85) Geiger, F.; Busse, C. A.; Loehrke, R. I. The Vapor Pressure of Indium, Silver, Gallium, Copper, Tin, and Gold between 0.1 and 3.0 Bar. *Int. J. Thermophys.* **1987**, *8* (4), 425–436.

(86) Dubrovskii, V. G. Refinement of Nucleation Theory for Vapor-Liquid-Solid Nanowires. *Cryst. Growth Des.* **2017**, *17* (5), 2589–2593.

(87) Glas, F. Chemical Potentials for Au-Assisted Vapor-Liquid-Solid Growth of III-V Nanowires. *J. Appl. Phys.* **2010**, *108* (7).

(88) Oliveira, D. S. Role of Group V Atoms during GaAs Nanowire Growth Revealed by Molecular Dynamics Simulations: Implications in the Formation of Sharp Interfaces. *ACS Appl. Nano Mater.* **2021**.

(89) Guo, Y. N.; Zou, J.; Paladugu, M.; Wang, H.; Gao, Q.; Tan, H. H.; Jagadish, C. Structural Characteristics of GaSb/GaAs Nanowire Heterostructures Grown by Metal-Organic Chemical Vapor Deposition. *Appl. Phys. Lett.* **2006**, *89* (23), 6–9.

(90) Jeppsson, M.; Dick, K. A.; Wagner, J. B.; Caroff, P.; Deppert, K.; Samuelson, L.; Wernersson, L. E. GaAs/GaSb Nanowire Heterostructures Grown by MOVPE. *J. Cryst. Growth* **2008**, *310* (18), 4115–4121.

(91) Ghalamestani, S. G.; Lehmann, S.; Dick, K. A. Can Antimonide-Based Nanowires Form Wurtzite Crystal Structure? *Nanoscale* **2016**, 2778–2786.

(92) Ghalamestani, S. G.; Ek, M.; Dick, K. A. Realization of Single and Double Axial InSb – GaSb Heterostructure Nanowires. *Phys. Status Solidi RRL* **2014**, *273* (3), 269–273.

(93) Straumanis, M. E.; Kim, C. D. Lattice Parameters, Thermal Expansion Coefficients, Phase Width, and Perfection of the Structure of GaSb and InSb. *J. Appl. Phys.* **1965**, *36* (12), 3822–3825.

(94) Verheijen, M. A.; Immink, G.; De Smet, T.; Borgström, M. T.; Bakkers, E. P. A. M. Growth Kinetics of Heterostructured GaP-GaAs Nanowires. *J. Am. Chem. Soc.* **2006**, *128* (4), 1353–1359.

(95) Ek, M.; Borg, B. M.; Dey, A. W.; Ganjipour, B.; Thelander, C.; Wernersson,

L. E.; Dick, K. A. Formation of the Axial Heterojunction in GaSb/InAs(Sb) Nanowires with High Crystal Quality. *Cryst. Growth Des.* **2011**, *11* (10), 4588–4593.

(96) Dheeraj, D. L.; Patriarche, G.; Zhou, H.; Harmand, J. C.; Weman, H.; Fimland, B. O. Growth and Structural Characterization of GaAs/GaAsSb Axial Heterostructured Nanowires. *J. Cryst. Growth* **2009**, *311* (7), 1847–1850.

(97) Lugani, L.; Ercolani, D.; Beltram, F.; Sorba, L. Growth Mechanism of InAsInSb Heterostructured Nanowires Grown by Chemical Beam Epitaxy. *J. Cryst. Growth* **2011**, *323* (1), 304–306.

(98) Sjökvist, R.; Tornberg, M.; Marnauza, M.; Jacobsson, D.; Dick, K. A. Observation of the Multilayer Growth Mode in Ternary InGaAs Nanowires. *ACS Nanosci. Au* **2022**, *2* (6), 539–548.

(99) Plissard, S.; Dick, K. A.; Wallart, X.; Caroff, P. Gold-Free GaAs/GaAsSb Heterostructure Nanowires Grown on Silicon. *Appl. Phys. Lett.* **2010**, *96* (12), 2008–2011.

(100) Kindlund, H.; Zamani, R. R.; Persson, A. R.; Lehmann, S.; Wallenberg, L. R.; Dick, K. A. Kinetic Engineering of Wurtzite and Zinc-Blende AlSb Shells on InAs Nanowires. *Nano Lett.* **2018**.

Printed by Media-Tryck, Lund 2025 NORDIC SWAN ECOLABEL 3041 0903

ISBN 978-91-8096-086-1

Centre for Analysis and Synthesis
Department of Chemistry
Faculty of Engineering
Lund University

9 789180 960861